On modelling and physics of ice-age ice sheet-sea level-solid Earth interactions

Kyeore Holly Han
Department of Earth and Planetary Sciences
McGill University, Montreal

Supervisor
Natalya Gomez

A thesis submitted to McGill University in partial fulfillment of
the requirements of the degree of

Doctor of Philosophy in Earth and Planetary Sciences

April, 2021

Abstract

The retreat and advance of ice sheets perturb the Earth's solid surface, gravitational field and rotation, leading to spatially and temporally varying changes in the elevation of the ocean surface and solid Earth and hence sea level (glacial isostatic adjustment; GIA). Modelling studies have shown that sea-level changes associated with GIA in turn feed back onto ice sheets, confirming the coupled nature of ice sheets, the solid Earth and sea level. These interactions occur over a range of timescales (from decadal to multi-millennial and longer) and have important implications for ice sheet stability and sensitivity to climate changes in marine and terrestrial settings. Understanding the physics of these interactions through the Earth's glacial history is pertinent to interpreting ice-sheet and sea-level records from the past, understanding ongoing changes and projecting future climate changes.

This thesis expands 1) the understanding of the history and physics of coupled ice-sheet and sea-level changes in the Northern Hemisphere over the last glacial cycle and 2) the computational capability of coupled ice-sheet – sea-level modelling. In the first study, I apply a sea-level model to simulate gravitationally consistent sea-level changes in North America associated with ice melting through the last deglaciation (21-6 thousand years ago). I separate the ice and water loading signals from periods during active deglaciation and post-deglaciation phases and show how these signals lead to a possible bias in interpreting geophysical records used to constrain the viscosity underlying mantle in the Hudson Bay region. I also identify sites where the bias is minimized in the region.

In the second study, I explore how deformation of the solid Earth and perturbations of the gravitational field impacted the evolution of ice sheets in the Northern Hemisphere during the last glacial cycle using a coupled ice-sheet – sea-level model. I demonstrate that solid Earth deformation enhances the dynamics of the Northern Hemispheric ice sheets, causing greater fluctuations of ice sheets in North America and Eurasia throughout the glacial cycle and that gravitational perturbations influence the stability of marine-based sectors of ice on decadal to centennial timescales.

Finally, I develop a novel “time window” algorithm in a sea-level model to replace the classic algorithm of temporal discretization of the ice history in the model. This algorithm improves the computational efficiency of the model and thus allows for capturing the short-term scale interactions between ice sheets, solid Earth and sea level within glacial-cycle scale simulations with a coupled ice sheet – sea level model. I apply the new algorithm to simulate ice-sheet and sea-level variations globally over the past two glacial cycles and the future retreat of the Antarctic Ice Sheet due to anthropogenic climate warming between 1950-2500 AD. I show that using the time window algorithm reduces the total CPU calculation times by at least by 50% in both cases.

Overall, I contribute to expanding the understanding of the interactions between GIA and ice sheets over broader spatiotemporal scales.

Résumé

Le recul et l'avance des calottes glaciaires perturbent la surface solide de la Terre, son champ gravitationnel et sa rotation, entraînant des changements spatiaux et temporels à l'élévation de la surface de l'océan et de la Terre solide et donc au niveau de la mer (ajustement isostatique glacier; GIA). Des études de modélisation ont démontré que les changements du niveau de la mer associés au GIA se répercutent à leur tour sur les calottes glaciaires, confirmant la nature couplée des calottes glaciaires, de la Terre solide et du niveau de la mer. Ces interactions se produisent sur une gamme d'échelles de temps (de la décennie à plusieurs millénaires et plus) et ont des implications importantes pour la stabilité des calottes glaciaires et leur sensibilité aux changements climatiques dans les milieux marins et terrestres. La compréhension du charactère et de la physique de ces interactions à travers l'histoire glaciaire de la Terre est pertinente pour interpréter les enregistrements passées des calottes glaciaires et du niveau de la mer, comprendre les changements en cours (actuels) et projeter les changements climatiques futurs.

Cette thèse élargit 1) la compréhension de l'histoire et de la physique des changements couplés de la calotte glaciaire et du niveau de la mer dans l'hémisphère nord au cours du dernier cycle glacier et 2) la capacité informatique de la modélisation couplée de la calotte glaciaire et du niveau de la mer. Dans la première étude, j'applique un modèle du niveau de la mer pour simuler les changements gravitationnels du niveau de la mer en Amérique du Nord associés à la fonte des glaces lors de la dernière déglaciation (il y a 21000 à 6000 avant le présent). Je sépare les signaux de charge de glace et d'eau des périodes pendant les phases de déglaciation active et de post-déglaciation et je démontre comment ces signaux mènent à un biais possible dans l'interprétation des enregistrements géophysiques utilisés pour contraindre la viscosité du manteau sous-jacent la région de la baie d'Hudson. J'identifie également les sites où le biais est minimisé dans la région.

Dans la deuxième étude, j'explore comment la déformation de la Terre solide et les perturbations du champ gravitationnel ont eu un impact sur l'évolution des calottes glaciaires dans l'hémisphère nord au cours du dernier cycle glaciaire en utilisant un modèle couplé calotte glaciaire-niveau de la mer. Je démontre que la déformation de la Terre solide améliore la dynamique des calottes glaciaires de l'hémisphère Nord, provoquant de plus grandes fluctuations des calottes glaciaires en Amérique du Nord et en Eurasie tout au long du cycle glacier et que les perturbations gravitationnelles influencent la stabilité des secteurs de glace marins sur des échelles de temps décennales à centenaires.

Enfin, je développe un nouvel algorithme de «fenêtre temporelle» dans un modèle de niveau de la mer pour remplacer l'algorithme classique de discrétisation temporelle de l'histoire des glaces dans le modèle. Cet algorithme améliore l'efficacité informatique du modèle et permet ainsi de capturer les interactions à court terme entre les calottes glaciaires, la Terre solide et le niveau de la mer dans des simulations à l'échelle du cycle glaciaire avec un modèle couplé calotte glaciaire - niveau de la mer. Je applique le nouvel algorithme pour simuler les variations des calottes glaciaires et du niveau de la mer à l'échelle mondiale au cours des deux derniers cycles glaciers et pour simuler le futur retrait de la calotte glaciaire antarctique en raison du réchauffement climatique anthropique entre 1950 et 2500 AD. Je démontre que l'utilisation de l'algorithme de fenêtre temporelle réduit le temps total de calcul du processeur d'au moins 50% dans les deux cas.

Dans l'ensemble, à travers cette thèse, je contribue à élargir la compréhension des interactions entre le GIA et les calottes glaciaires à des échelles spatiales et temporelles plus larges qu'auparavant.

List of Figures

List of Tables

Acknowledgements

First, I would like to thank my advisor, Dr. Natalya Gomez, for her supervision that made completing this thesis possible. I could not have become a scientist and the person I am today without Natalya's dedicated mentorship throughout the past six years of my Ph.D. journey. I feel challenged to express my gratitude in words because the extent and depth of it are boundless, but here is my trial: Thank you, Natalya, for giving me a chance to work with you, for seeing potential in me as a scientist and for helping me through thick and thin. Your commitment, persistence, perseverance and solicitous support in working with your students while continually excelling in your own scientific career has always inspired me to strive to become a better scientist, a mentor and a colleague. I am aware that I still have a long way to go, and you will continue to motivate me throughout my career.

I also thank my Ph.D. committee members Dr. Alfonso Mucci, Dr. Fiona Darbyshire, Dr. Yajing Liu and Dr. William Minarik for advice before, during and after my Ph.D. qualification exam.

I want to express deep gratitude to Dr. David Pollard and Dr. Rob deConto, who have provided support and motivation during our collaboration. Working with Dave and Rob was a privileging experience through which I have learnt not only in the means of science but also the joy of collaboration.

Since I started as the first and only member of Gomez Geodynamics Group

(GGG) in 2015, many more have come through and arrived to create a fantastic group. I thank Anna Hayden, David Purnell, Erik Chan, Gabriel Tseng, Jeannette Wan, Julia Morales-Aguirre, Katarina Kuhnert, Linda Pan, Maryam Yousefi, Morgan Flament, Tomas Milla-Knoch, Thomas Navarro. They all have directly and indirectly influenced me to grow during my time at McGill. I also thank many friends and peers at the Department of the Earth and Planetary Sciences. I want to name Andres Peña-Castro, Ashley Dinaur and Joel Schwartz particularly. Too many thanks go to Angela Di Ninno (I hope you are resting in peace, Angela), Anne Kosowski and Kristy Thornton at the EPS Department, who have helped me immensely in essential matters throughout my degree.

I cannot miss mentioning Dr. Sabine Stanley and Dr. Paul Kushner, who mentored me during my undergraduate program at the Department of Physics at the University of Toronto. I will be grateful forever to Sabine and Paul for helping me knock on the door of graduate study, the door to an opportunity to be a scholar.

Athletic activities have been an essential part of my life at McGill, which I embraced with all my heart and conferred nearly equal value as my degree. I thank my friends, teammates and coaches from McGill Martlet Soccer Team and McGill Track and Field Team, particularly Cheryl Leung, Jose Valdes, Justine Enns, Laura Strenger, Lisa Perrett, Mimi Simmons, Ollie Lusterio-Adler, Olivia Trotter, Sarah Dubois, Selwynne Hawkins, Sophie Barlos and Yue Jiao. The time, sweat, tears and friendship we shared on the pitch, inside the locker room, fieldhouse, the weight room and outside the campus made my times at McGill beautiful. I also thank McGill Athletics and Recreation for providing such great programs and intramural leagues that I have fully enjoyed participating in as a player, a referee and a supervisor. To all my teammates and colleagues I played and worked with, thank you.

I would not be exaggerating to say that I have finished close to half the work in my thesis from café Genki crépe. Lin, thank you for the great coffee, friendship and support throughout my time at McGill.

Finally, I thank my family – my mom and dad, who have given me genuine love, trust and freedom that allowed me to be brave and explore anything and everything in the world that I was curious about. I also thank them for demonstrating the continuous growth of an individual throughout a lifetime with positivity and passion. My little sister, Minjoo - whom I love dearly and could do anything for – has always provided love and support during my journey. Thank you, and I love you, everyone.

Contribution to original knowledge

I confirm that this thesis presents original research and the results of my own work, unless otherwise referenced and acknowledged in this thesis.

This thesis contributes to the original knowledge of the feedback between ice sheets and glacial isostatic adjustment over a range of spatiotemporal scales during the last ice age. It shows how different feedback mechanisms act over different timescales on the evolution of ice sheets. It also contributes to extending the current state-of-art in coupled ice sheet – sea level modelling by developing a new sea-level model algorithm that allows coupled models to capture the annual to decadal ice-sheet – sea-level - solid Earth interactions while running over 100,000 years glacial-cycle timescales.

Contribution of authors

This thesis is composed of three manuscripts that I have written as the first author and developed through collaboration with my advisor Natalya Gomez (NG) and colleagues David Pollard (DP), Robert DeConto (RD) and Jeannette Xiuwen Wan (JXW).

The first manuscript (Chapter 2) has been published as follows: Han, H. K. and Gomez, N. "The impact of water loading on postglacial decay times in Hudson Bay", Earth Planet. Sci. Lett. (2018), 489, 1-10. doi.org/10.1016/j.epsl.2018.02.043. In the work, I performed numerical simulations and analysis, with contribution from NG to designing the project, modifying the GIA/sea-level model for the numerical experiments as well as writing and editing the manuscript.

The second manuscript (Chapter 3) is currently in press and can be cited as Han, H. K., Gomez, N., Pollard, D. and DeConto, R. Modeling Northern Hemispheric ice sheet dynamics, sea level change and solid Earth deformation through the last glacial cycle (2021), Journal of Geophysical Research. doi: 10.1029/2020JF006040. NG and I have designed the study, I have modified an ice-age GIA/sea-level model in Fortran 90 version (provided by Jerry Mitrovica's group at Harvard University) to a forward GIA/sea-level model, coupled the forward GIA/sea-level model to the PSU ice-sheet model based on a published algorithm (Gomez et al., 2013), modified the GIA/sea-level modelling for the numerical experiments, performed numerical simulations and analysis and wrote the manuscript. DP and RD provided the PSU dynamic ice-sheet model, DP contributed to adapting the ice-sheet model for the application, choosing the ice sheet model parameters in the analysis. DP and RD also provided general guidance on ice-sheet and climate modeling components throughout the preparation of the manuscript. All co-authors contributed to discussions of the results, editing and reviewing the manuscript.

The third manuscript (Chapter 4) is in preparation for a submission to a peer-reviewed journal Geoscientific Model Development (GMD) under the manuscript type "Development and technical papers". The work is co-authored with NG and JXW. I have developed and implemented a novel sea-level model time window algorithm, performed numerical simulations and analysis and I wrote the manuscript. NG provided motivation and vision for the work and contributed to manuscript revisions, JXW contributed to discussions of results and all authors contributed to designing the numerical experiments.

Contents

Chapter 1

Introduction

1.1 Context and motivation

Changing sea level and related risks of extreme climate events in our warming world are a rising concern to humanity. Global and local sea levels change due to various effects over a range of timescales from diurnal to multi-millennial. For example, the effects include variations in ocean density and salinity, ocean tides, sea surface waves, atmospheric pressure and ocean circulation, mass exchanges between the cryosphere and hydrosphere, adjustment of the gravitational field, rotation and viscoelastic solid Earth associated with the mass exchanges (glacial isostatic adjustment, GIA) and the flow of the Earth's mantle (dynamic topography) (Gregory et al., 2019).

Among the various contributions to sea-level change, the contribution of the polar ice sheets are projected to dominate future sea-level rise on multi-century timescales (IPCC SROCC). However, our incomplete knowledge of ice-sheet responses to different greenhouse gases emission pathways causes deep uncertainties in future sea-level projections (Kopp et al., 2019). An ice sheet evolves by deforming internally under its own weight and interacts with the surrounding atmosphere, underlying bedrock and ocean water. These interactions occur over a range of timescales in a nonlinear fashion, posing challenges in determining a complete diagnosis of ice-sheet sensitivity to climate change. We have not yet witnessed the ice sheets responding to the level of warming expected in future with modern satellite and in-situ observations. In this regard, modelling the Earth's past ice sheets with physics-based models constrained by paleoenvironmental records can inform our understanding of ice-sheet physics and improve future sea-level projections (DeConto and Pollard., 2016; Gilford et al., 2020; Gomez et al., 2020).

The Earth's climate has been naturally driven by the orbital configuration of the planet (i.e., eccentricity, precession and obliquity, so-called Milankovitch cycles) that controls the amount of incoming solar radiation on the Earth surface and atmospheric greenhouse gases that control the absorption of the outgoing radiation emitted back from the Earth's surface. During the Pleistocene epoch (the last 1 Million years) in the Quaternary Period (the last 2.58 Million years), surface temperature and atmospheric CO_2 fluctuated, and continental ice sheets varied accordingly with a periodicity of ∼100 thousand years (ky) (Shackleton, 1967). The most recent glacial cycle (i.e., the last glacial cycle) started following the last interglacial (∼129-116 ka) during which global temperature was ∼1 degree Celsius higher and sea level was ∼6-9 meters higher than the present day (Kopp et al., 2009; Dutton et al, 2015; DeConto et al., 2021). The global ice extent reached a maximum at ∼26-21 ka (Last Glacial Maximum, LGM; Clark et al., 2009; Yokoyama et al., 2018) when global mean sea level was ∼130 m lower than present (Austermann et al., 2013). The LGM was then followed by the Last deglaciation into the current interglacial (i.e., the Holocene, starting at ∼11.6 ka) with ice sheets remaining only in Greenland and Antarctica, which currently hold sea-level equivalent ice volumes of around 57.9 m and 7.4 m, respectively

(Morlighem et al., 2017; 2020).

Retreat or advance of an ice sheet has both direct and indirect effects on sea level (here we define sea level as the height difference between the sea surface and solid surface): In addition to contributing meltwater to the oceans, it perturbs Earth's gravitational field and rotation (centrifugal acceleration) and deforms the solid Earth (glacial isostatic adjustment, GIA; Woodward, 1888; Peltier, 1974; Farrell and Clark, Milne and Mitrovica, 1996; 1976; Milne, 1998a, b; Mitrovica and Milne, 2003), which in turn give rise to spatially variable sea-level changes. Moreover, the ocean water redistribution due to GIA in turn further perturbs Earth's gravitational field, rotation and solid surface. GIA occurs over a range of timescales, with an immediate, elastic response of the Earth to changes in surface (ice and ocean) loading and rotational changes followed by a slower response associated with the viscous flow of the mantle that typically takes places on multi-millennial timescales depending on the viscosity structure of the Earth's interior. Sea-level changes associated with GIA in response to surface loading changes are numerically modelled by a sea-level model (described in more detail in section 1.3). (Note that a sea-level model is also interchangeably called a "GIA model" or an "Earth/sea-level model" in different sub-fields and contexts. This thesis uses the term "sea-level model" except for Chapter 3 that uses the term "GIA model").

Spatially and temporally varying sea-level changes depend on the history of ice cover changes and the Earth's rheological structure. Reconstruction of paleo ice sheets has been mainly based on either geological and geophysical observations and sea-level modelling or dynamic ice-sheet modelling. The former utilizes a sea-level model and iteratively refines the input ice histories and the Earth model such that the model results match with observational sea-level records (e.g., ICE-5G, Peltier 2004; ANU model, Lambeck et al., 2014). The latter utilizes dynamic ice-sheet modelling to numerically solve the ice-sheet processes under an applied climate forcing with prescribed model parameters and boundary conditions (e.g., Pollard and DeConto, 2012; Albrecht et al., 2020). Each of these approaches has strengths and limitations: The reconstructed ice history based on sea-level modelling has its configurations and spatially varying sea-level predictions matching with observational sea-level data but lacks ice sheet physics (i.e., ice cover changes are prescribed and so can be glaciologically inconsistent), whereas the reconstructed ice history based on ice-sheet modelling is glaciologically consistent, but does not include predictions of spatially varying sea-level changes and the resulting predictions of sea-level contribution do not always match with sea-level data.

In the last decade, coupled dynamic ice-sheet - sea-level models have been developed to self-consistently compute spatially varying sea-level and dynamic ice-sheet response to climate changes. Gomez et al. (2010, 2012) identified a new feedback mechanism between ice sheets and GIA and later studies confirmed that the feedback has a significant effect on the paleo and future evolution of marine-based sectors of the Antarctic Ice Sheet (e.g., Gomez et al., 2013; de Boer et al., 2014; Konrad et al., 2015; Larour et al., 2019). The evolution of a marine-based ice sheet is strongly dependent on the ocean depth at a grounding line (boundary where the grounded portion of the ice sheet extends into ocean and forms an ice shelf) and the slope of bedrock underneath the ice sheet (e.g., Weertman, 1974; Thomas and Bentley, 1978; Schoof, 2007) such that the ice flux across the grounding line increases with ocean depth there. In the absence of GIA feedback, the ocean depth at the grounding line increases as the grounding line retreats over a reverse-sloped bed that deepens towards the interior, leading to a runaway retreat (so called "Marine Ice Sheet Instability", MISI; Weertman, 1974). However, the ocean depth at the grounding line decreases when the GIA feedback is included, mainly because of rebounding of the solid Earth and drawing down of sea surface associated with weakened gravitational attraction between water and ice, stabilizing the ice sheet from a runaway retreat (Gomez et al., 2010; 2012).

In confirming the feedback mechanism between ice sheets and GIA, Gomez et al. (2013) first developed a coupled ice-sheet – sea-level model that incorporates GIA feedback with radially varying (1-D) Earth structure (Mitrovica and Milne, 2003; Kendall et al., 2005). They applied the coupled model to the Antarctic Ice sheet (AIS) through the last 40 ky and demonstrated the stabilizing effects of this "sea-level feedback" (see Fig. 1.1) on the advance and retreat of the marine-based West Antarctic Ice Sheet (WAIS). Gomez et al. (2015) and Konrad et al. (2015) then applied their model to project the future evolution of the AIS under a range of climate forcing incorporating a suite of viscoelastic Earth structure. de Boer et al. (2014) also developed a 3-D coupled ice sheet-sea level model to simulate the evolution of ice sheets on a global scale over four glacial cycles (410 ky). The majority of the above studies focused on modelling AIS evolution in the Southern Hemisphere, presumably because the stability of the marine-based portion of the AIS (i.e., WAIS) is imperilled by global warming.

The Northern Hemisphere during the last glacial cycle is also an exciting place and period to study the feedbacks between ice sheets and GIA. Large continental ice sheets evolved over North America, Eurasia and Greenland (e.g., Dyke, 2004; Kleman et al., 2010; Hughes et al., 2016). Viscoelastic deformation of the solid Earth would have impacted positively or negatively on the dynamics and surface mass balance of the ice sheet through changes in ice surface slope and elevation (i.e., "ice-elevation feedback", see Fig. 1.1; Levermann and Winkelmann, 2016). Two studies have explored the impact of the solid Earth feedback on the Eurasian Ice Sheet (van den Berg et al., 2008) and Northern Hemispheric Ice Sheet (Crucifix

(a) Ice sheets - GIA feedback mechanism

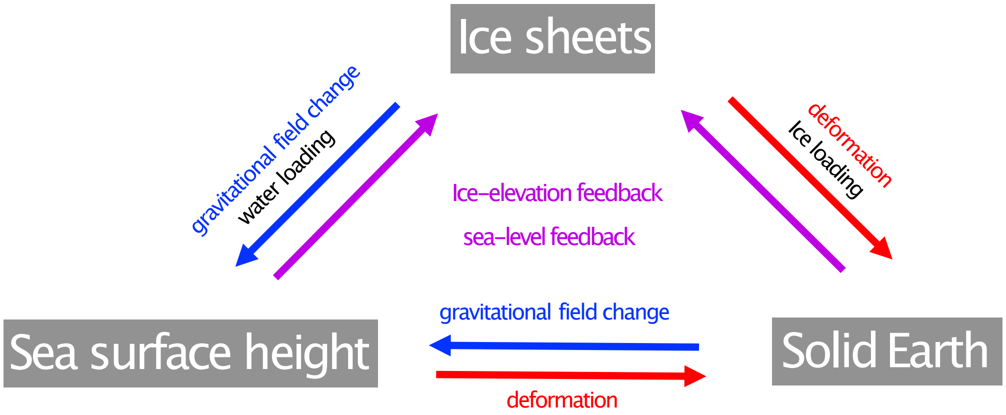

(b) Sea-level feedback

(c) Ice-elevation feedback

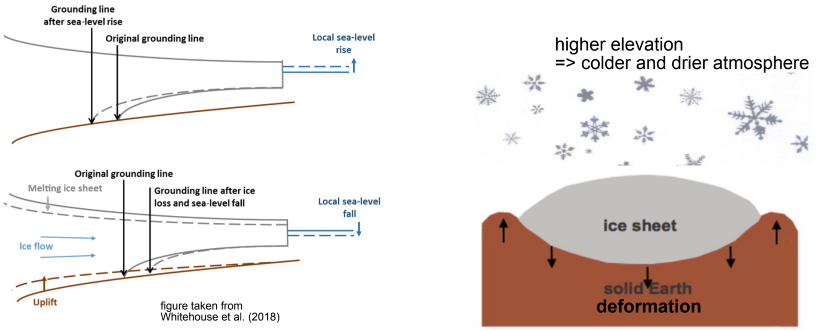

figure taken from
Whitehouse et al. (2018)

Marine-based ice sheet

Land-based ice sheet

Figure 1.1: Interactions between ice sheets, sea level and the solid Earth. Schematic diagram of the (a) ice sheets - GIA feedback, (b) sea-level feedback and (c) ice-elevation feedback.

et al., 2001) during the last glacial cycle. However, their results differed, and the role of solid Earth deformation on these ice-sheet evolutions remains to be investigated further. Moreover, the sea-level feedback could have influenced the extensive marine-based ice sheets over Hudson Bay in North America and the Barents and Kara Seas in the Eurasian region. These marine-based ice sheets could have contributed a measurable amount to episodic sea-level rise events during the last deglaciation phase (Melt Water Pulse events; Fairbanks, 1989; Deschamps et al., 2012).

1.2 Thesis Overview

In this thesis, I study the ice sheet-GIA feedback in the Northern Hemisphere through the last glacial cycle and advance our understanding and modelling of the interactions between ice, sea level and the solid Earth to span over longer timescales and greater spatial scales. I start by investigating the unidirectional influence of surface (ice and water) loading changes on sea-level changes and the interpretation of geological sea-level records from the Hudson Bay region using a standalone sea-level model (Ch. 2). I move on to study the two-way influence between ice sheets and GIA using a coupled ice-sheet – sea-level model in Northern Hemisphere through the last glacial cycle (Ch. 3). Finally, I further extend the coupled modelling by developing an algorithm in the sea-level model that allows the coupled model to capture short-term (annual to decadal) feedbacks between ice sheets and GIA within much longer simulations, which was previously infeasible (Ch. 4).

More specifically, in Chapter 2, I explore the subtleties of postglacial sea-level processes during and after the last deglaciation in Hudson Bay. I re-examines the geological observables called “postglacial decay times” that are estimated from paleo-sea level records and have been used to infer mantle viscosity under previously glaciated regions in Hudson Bay in North America (Mitrovica and Peltier, 1995; Mitrovica and Forte; 2004; Lau et al, 2016). I quantify potential bias in postglacial decay-time estimates due to recent and ongoing ice and water loading changes. Results show that ice unloading and Holocene water loading changes in the bay can impart a significant geographic trend on the decay time estimates if the time window used to compute decay times includes periods that are temporally close to (i.e., contemporaneous with, or soon after) periods of active loading.

Chapter 3 explores the interactions between ice sheets, solid Earth and sea level over the last glacial cycle in the Northern Hemisphere and investigates the roles of solid Earth deformation and gravitational perturbations on the evolution of the Northern Hemispheric Ice Sheets. I show that the impacts of these effects on ice sheet evolution depend on an ice sheet's size and location: The larger North American Ice Sheet Complex is more sensitive to GIA effects than the smaller Eurasian Ice Sheet Complex. Moreover, in a terrestrial setting, solid Earth deformation acts upon the continental ice sheet dominantly through ice surface mass balance feedback over the span of thousands of years. In marine-terminating areas, gravitational field perturbations and solid Earth deformation together dominantly influence ice sheet changes through sea-level forcing over a shorter, centennial timescale.

Finally, in Chapter 4, I tackle computational challenges posed in coupled ice-sheet - sea-level modelling by addressing the need to capture short-term $O(\leq 10^2$ yr) interactions within long-term $O(> 10^2$ yr) simulations. I develop a new "travelling time window" algorithm within the sea-level model that improves computational efficiency while maintaining model precision. The algorithm will allow future studies to examine the interactions between ice sheets, sea level and the solid Earth over much longer timescales and at higher temporal resolution.

The remaining sections expand on the sea-level theory and modelling, ice-sheet modelling and coupled ice-sheet – sea-level modelling as background information for the rest of this thesis.

1.3 The generalized sea-level equation

This section derives the generalized sea-level equation (Mitrovica and Milne, 2003), which is a fundamental pillar of this thesis. In the static sea-level theory, the sea surface is defined to remain on a gravitational equipotential surface. Sea level (SL) is globally defined as the radial height difference between the sea surface G and the solid surface R, where topography T (excluding ice height) is defined as the negative of sea level. That is,

$$SL(\theta, \psi, t_j) = G(\theta, \psi, t_j) - R(\theta, \psi, t_j), \tag{1.1}$$

$$T(\theta, \psi, t_j) = -SL(\theta, \psi, t_j) = R(\theta, \psi, t_j) - G(\theta, \psi, t_j), \tag{1.2}$$

where θ is the colatitude, ψ is the east-longitude, and t_j is the time. Note that a shoreline is defined as $SL(\theta, \psi, t_j) = T(\theta, \psi, t_j) = 0$ in an ice-free region.

Ocean depth is expressed as a projection of the globally defined sea level onto the surface areas covered by ocean,

$$S(\theta, \psi, t_j) = SL(\theta, \psi, t_j)\, C^*(\theta, \psi, t_j) \tag{1.3}$$

where C^* is the ocean function defined as follows:

$$C^*(\theta,\psi,t_j) = \begin{cases} 1 & \text{if } SL(\theta,\psi,t_j) > 0 \text{ and there is no grounded ice} \\ 0 & \text{elsewhere.} \end{cases} \tag{1.4}$$

Change in the globally defined sea level arises from perturbations in the sea surface and solid surface after a surface load mass exchange between ice sheets and ocean, expressed as follows:

$$\Delta SL(\theta,\psi,t_j) = \Delta G(\theta,\psi,t_j) - \Delta R(\theta,\psi,t_j), \tag{1.5}$$

where the symbol Δ indicates a change in the given field from time t_0 to t_j. The term indicating perturbation in the sea surface, $\Delta G(\theta,\psi,t_j)$, on the right-hand side of Eqn. 1.5, can be decomposed into two terms,

$$\Delta G(\theta,\psi,t_j) = \mathcal{G}(\theta,\psi,t_j) + \frac{\Delta\Phi(t_j)}{g}. \tag{1.6}$$

The first term represents a geographically variable change in the height of gravitational (sea-surface) equipotential surface due to perturbations in the original gravitational equipotential and the second term represents a geographically uniform shift in gravitational equipotential surface, invoked to satisfy the mass conservation of surface (ice and water) load. Thus, change in globally defined sea level can then be separated into geographically variable and uniform components expressed as follows:

$$\Delta SL(\theta,\psi,t_j) = \Delta\mathcal{SL}(\theta,\psi,t_j) + \frac{\Delta\Phi(t_j)}{g}, \tag{1.7}$$

where the first and the second terms of Eqn. 1.7 are defined as follow:

$$\Delta\mathcal{SL}(\theta,\psi,t_j) = \Delta\mathcal{G}(\theta,\psi,t_j) - \Delta R(\theta,\psi,t_j) \tag{1.8}$$

and

$$\begin{aligned}\frac{\Delta\Phi(t_j)}{g} = &-\frac{1}{A(t_j)}\frac{\rho_i}{\rho_w}\iint_\Omega \Delta I(\theta,\psi,t_j)\,d\Omega \\ &-\frac{1}{A(t_j)}\iint_\Omega \Delta\mathcal{SL}(\theta,\psi,t_j)\,C^*(\theta,\psi,t_j)\,d\Omega \\ &+\frac{1}{A(t_j)}\iint_\Omega T(\theta,\psi,t_0)\,[\,C^*(\theta,\psi,t_j) - C^*(\theta,\psi,t_0)\,]d\Omega,\end{aligned} \tag{1.9}$$

where ρ_i and ρ_w are the density of ice and water, respectively, A is the ice-free ocean area at time t_j given by integrating the ocean function over the Earth's surface Ω,

$$A = \iint_\Omega C^*(\theta,\psi,t_j)\,d\Omega. \tag{1.10}$$

After some algebra based on the equations above, change in ocean depth relative to the initial $t = t_0$ depth in response to redistribution of ice and water loading is expressed in the generalized sea-level equation derived by Mitrovica and Milne (2003),

$$\begin{aligned}\Delta S(\theta,\psi,t_j) = &\left[\Delta\mathcal{SL}(\theta,\psi,t_j) + \frac{\Delta\Phi(t_j)}{g}\right] C^*(\theta,\psi,t_j) \\ &- T(\theta,\psi,t_0)\,[\,C^*(\theta,\psi,t_j) - C^*(\theta,\psi,t_0)\,].\end{aligned} \tag{1.11}$$

The first expression on the right-hand side of Eqn. 1.11 indicates projection of sea-level change at t_j onto the ocean function at t_j. This expression incorporates solid Earth deformation and perturbations in the gravitational field associated with surface mass loading and changes in Earth rotation. The second expression indicates a topographic correction applied to the initial topography accounting for shoreline migration due to changes in local sea-level and marine-based ice-sheet extent.

The formalism of the equation is valid for any arbitrary Earth model (that is, either radially and/or laterally varying structure of the solid Earth). Throughout this thesis, the geographically variable sea-level change term ($\Delta\mathcal{SL}$) is solved by incorporating a spherically symmetric (1D radially varying), linear Maxwell viscoelastic Earth rheology model that describes linear creep under constant stress. Adopting this linear Maxwell rheology allows for a transformation between the time domain and the Laplace domain and thus analytical convolution of surface (ice and ocean) loading changes and Green Functions (i.e., response function) over space and time. That is, the expression is written out as follows:

$$\Delta\mathcal{SL}(\theta,\psi,t_j) = \int_{-\infty}^{t_j} \iint_{\Omega} \Delta L(\theta^{'},\psi^{'},t_j^{'}) \left[\frac{\Phi(\gamma,t_j-t^{'})}{g} - \Gamma(\gamma,t_j-t^{'}) \right] d\Omega' dt', \quad (1.12)$$

the first term ΔL represents total surface loading changes:

$$\Delta L(\theta,\psi,t_j) = \rho_i \Delta I(\theta,\psi,t_j) + \rho_w \Delta S(\theta,\psi,t_j), \quad (1.13)$$

Φ and Γ in Eqn. 1.12 represent Greens Functions for gravitational potential perturbation and solid Earth deformation, respectively. On a sphere, these Greens Functions are expressed in terms of Legendre polynomial as follow:

$$\Phi(\gamma, t_j) = \frac{ag}{M_e} \sum_{l=0}^{\infty} \left[\delta(t) + k_l^E \delta(t) + \sum_{k=1}^{K} r_k^{\prime l} e^{-s_k^l t} \right] P_l(cos\gamma) \tag{1.14}$$

$$\Gamma(\gamma, t_j) = \frac{a}{M_e} \sum_{l=0}^{\infty} \left[h_l^E \delta(t) + \sum_{k=1}^{K} r_k^l e^{-s_k^l t} \right] P_l(cos\gamma), \tag{1.15}$$

where a is the radius of the Earth, g is the gravitational acceleration constant, M_e is the mass of the Earth, $P_l(cos\gamma)$ is the Legendre polynomial at l, the term $\delta(t)$ represents the direct effect of the surface loading on the gravitational field. The rest of the terms are the coefficients of the Legendre Polynomials called the surface loading "Love numbers" (Peltier, 1974), which describe the viscoelastic response of the solid Earth associated with the surface loading changes.

Substituting Eqns. 1.13-1.15 into Eqn. 1.12, and expressing Eqn. 1.12 as a Spherical Harmonic expansion yields,

$$\begin{aligned} \Delta\mathcal{SL}(\theta, \psi, t_j) = & \sum_{l,m} T_l E_l \left[\rho_i \Delta I_{lm}(t_j) + \rho_w \Delta S_{lm}(t_j) \right] Y_{lm}(\theta, \psi) \\ & + \sum_{l,m} T_l \sum_{n=0}^{j-1} \beta(l, t_n, t_j) \left[\rho_i \delta I_{lm}(t_n) + \rho_w \delta S_{lm}(t_n) \right] Y_{lm}(\theta, \psi), \end{aligned} \tag{1.16}$$

where l and m are Spherical Harmonics degree and order, respectively, and

$$T_l \equiv \frac{4\pi a^3}{M_e(2l+1)} \tag{1.17}$$

$$E_l = 1 + k_l^E - h_l^E \tag{1.18}$$

$$\beta(l, t_n, t_j) = \sum_{k=1}^{K} \frac{r_k'^l - r_k^l}{s_k^l}[1 - e^{-s_k^l(t_j - t_n)}]. \tag{1.19}$$

Thus, Eqns. 1.16-1.19 represent geographically variable sea-level changes due to solid Earth deformation and gravitational perturbation associated with the surface loading redistribution on a non-rotating Earth. Since surface loading redistribution itself and the associated sea-level changes in turn perturb the Earth's rotational vector, a number of studies (Milne and Mitrovica, 1996, 1998; Mitrovica et al., 2005) advanced the theory by implementing rotational effects in the generalized sea-level equation as follows:

$$\begin{aligned}\Delta\mathcal{SL}(\theta,\psi,t_j) = &\sum_{l,m} T_l E_l \,[\, \rho_i \Delta I_{lm}(t_j) + \rho_w \Delta S_{lm}(t_j) \,]\, Y_{lm}(\theta,\psi) \\ &+ \sum_{l,m} T_l \sum_{n=0}^{j-1} \beta(l,t_n,t_j) \,[\, \rho_i \delta I_{lm}(t_n) + \rho_w \delta S_{lm}(t_n) \,]\, Y_{lm}(\theta,\psi) \\ &+ \sum_{l,m} \frac{1}{g} E_l^T \,[\, \Delta\Lambda_{lm}(t_j) \,]\, Y_{lm}(\theta,\psi) \\ &+ \sum_{l,m} \frac{1}{g} \sum_{n=0}^{j-1} \beta^T(l,t_n,t_j) \,[\, \delta\Lambda_{lm}(t_n) \,]\, Y_{lm}(\theta,\psi).\end{aligned} \tag{1.20}$$

,

$$E_l^T = 1 + k_l^{T,E} - h_l^{T,E} \tag{1.21}$$

$$\beta^T(l, t_n, t_j) = \sum_{k=1}^{K} \frac{r_k^{\prime l,T} - r_k^{l,T}}{s_k^l}[1 - e^{-s_k^l(t_j - t_n)}]. \tag{1.22}$$

,

where Λ and g represent rotational (centrifugal) potential and gravitational acceleration, respectively. Overall, Eqn. 1.20 describes sea-level changes due to gravitational, deformational and rotational effects associated with the surface loading changes (the numerical form of this equation is shown in Supporting Information of Ch. 3) . Chapters 2 and 3 modify this sea-level equation to separate the contributions to sea-level change from ice loading and water loading (Ch. 2) and deformational effects and gravitational effects (Ch. 3). I also note here that some of the math is repeated in those chapters. The numerical formulation of this expression and description of the physical representation of Love numbers are also included in Supplementary Information for Ch. 3 of this thesis.

1.4 Sea-level modelling

A sea-level model takes an Earth structure model and ice history as inputs and numerically solves the generalized sea-level equation derived in the previous section. Outputs of a sea-level model are gravitationally consistent changes in the heights of the sea surface and solid surface (i.e., sea-level changes when combined) associated with surface (ice and water) loading redistribution (Fig. 1.2).

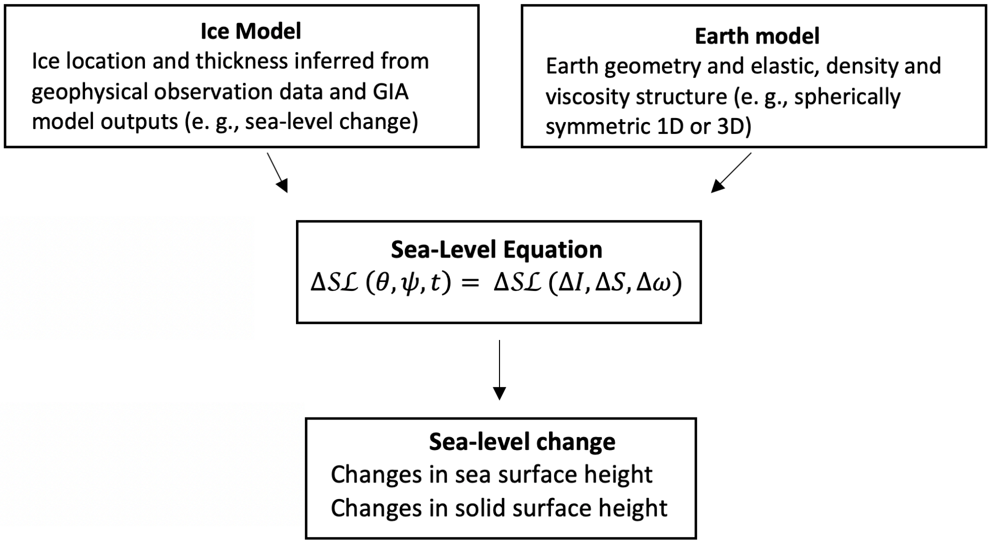

Figure 1.2: Principal components of a sea-level model

A sea-level model requires two inputs: an Earth model that describes the viscoelastic structure of the Earth (e.g., Fig. 1.3) and an ice history model that describes the thickness and extent of grounded ice through time (e.g., Lambeck et al. 2014; Peltier, 2004; Tarasov et al. 2012). For the Earth Structure (Fig. 1.3), the elastic and density structure of the Earth is typically provided by a seismic model such as Preliminary Reference Earth Model (PREM, Dziewonski and Anderson, 1981) and mantle viscosity can be inferred based on seismic tomography, geodetic and geologic constraints and lab experiments (e.g., Ishii and Tromp, 2001; Ritsema et al., 2011; Lloyd et al., 2020) or paleo sea-level data (e.g., Mitrovica and Forte, 2004; Lau et al., 2016;). Some applications adopt a 1-D depth varying Earth structure model that allows for fast sea-level computations with a pseudo-spectral approach to solving the sea-level equation (e.g., Mitrovica et al., 2001; Pico et al., 2017; Coulson et al., 2019), while some applications account for lateral variability in Earth structure (e.g., van der Wal et al., 2015; Hay et al., 2017; Nield et al., 2018). The latter are much more computationally expensive, but necessary to accurately capture deformation in structurally complex regions such as Antarctica (Gomez et al., 2018) or along tectonically active regions such as the North American West Coast (Yousefi et al., 2021). In this thesis, I incorporate a 1D Earth model as it allows for performing simulations in broader spatiotemporal scales.

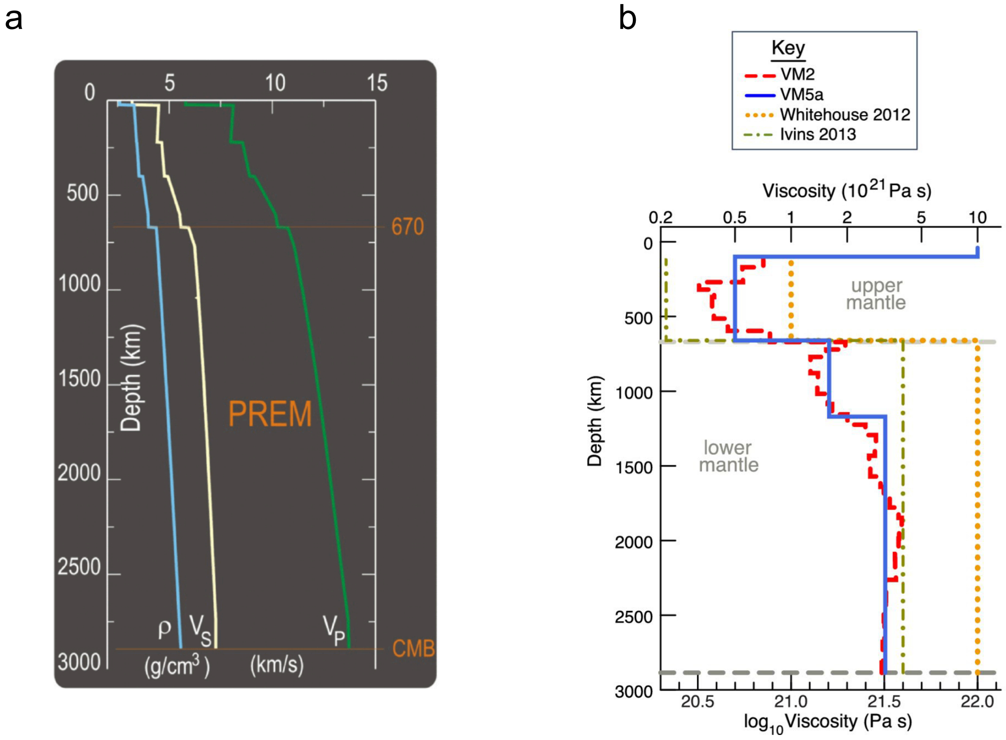

Figure 1.3: (a) Velocity and density structure of the Earth (Dziewonski and Anderson, 1981) and (b) mantle viscosity (taken from Argus et al., 2014)

Ice history (extent, thickness and chronology) inputs to sea-level models are typically reconstructed based on methods such as radiocarbon dating on glacial geomorphology observation data (e.g., terminal moraines, proglacial deposits, and ice and meltwater flow features; Dyke et al., 2002, 2003; Dyke, 2004), surface exposure dating (e.g., Carlson et al., 2007; Ullman et al., 2016) and tuning sea-level model outputs (i.e., predictions of postglacial sea-level history) to match observed relative sea-level records (e.g., Pendea et al., 2010; Lambeck et al., 2017; Simon et al., 2014) and space geodetic observations (e.g., GPS and GRACE; Argus et al., 2014; Peltier et al., 2015). The caveat of such reconstructed ice histories is that they lack ice-sheet physics. That is, the snapshots of ice sheet configurations through time are not glaciologically consistent. In this regard, coupling a dynamic ice-sheet model to a sea-level model fills in the missing gap by including ice-sheet physics in sea-level modelling.

1.5 Ice-sheet modelling

Ice sheets are modelled as very slowly moving (non-accelerating), incompressible, non-Newtonian viscous fluids (i.e., viscosity varies nonlinearly with ice velocity and temperature). Given a climate forcing that provides surface air and ocean temperature, and precipitation to compute surface mass balance and sub-ice-shelf melt rates along with other external conditions such as basal friction, geothermal heat flux, sea level and equilibrium bedrock topography, a dynamic ice-sheet model solves three main equations for the internal ice dynamics: 1) the momentum equation (i.e., Navier-Stokes equation; conservation of momentum) for ice velocity and pressure, 2) the energy equation (conservation of energy) for ice temperature and 3) the thickness equation (conservation of mass). In addition to these three equations, for multi-century simulations and longer, ice-sheet models also typically solve a simple equation for bedrock deformation under the ice.

In this thesis, I work with the PSU (PennState) 3D dynamic ice-sheet model developed by Pollard and DeConto (2012), which is a hybrid ice sheet-shelf model that combines the scaled Shallow Ice Approximation (SIA) and Shallow Shelf Approximation (SSA) equations to capture different modes of the flow of grounded ice sheets and floating ice shelves, respectively. Ice flux across the grounding zone is parameterized by ice thickness (and thus ocean depth) at the grounding zone following Schoof (2007). These two characteristics (flow approximations and grounding zone parametrization) together enable the PSU model to be feasible for continental-scale ice-sheet simulations over $O(10^7$ yr) timescales.

Sea-level changes are typically incorporated into the PSU ice-sheet model in stand-alone simulations by imposing a single value of global mean sea level derived from reconstructed ice history models (e.g., ICE5G; Peltier, 2004) or δ^{18}O (Lisieki and Raymo, 2005) to update the height of the sea surface in the model and solving a simple equation for bedrock deformation represented by the Elastic Lithosphere and Relaxed Asthenosphere model (ELRA; Le Meur and Huybrechts, 1996):

$$\frac{dh}{dt} = \frac{-1}{\tau}(w - h), \tag{1.23}$$

where h is bedrock elevation (positive downwards), w is the deflection of an elastic lithosphere, and τ is a relaxation time at which the rate of bedrock deformation decays (it is generally taken to be 3 ky). The ELRA bedrock model incorporates elastic flexure of the lithosphere as well as isostatic relaxation of the asthenosphere, but it does not capture a complex bedrock deformation characterized by multiple normal modes with distinct relaxation times (Peltier, 1974; Tromp and Mitrovica, 2000) and performs poorly particularly at edges (peripheral regions) of an ice sheet compared to the self-gravitating viscoelastic Earth model, which is incorporated in 1D sea-level models (e.g., Le Meur and Huybrecht, 1996; van den Berg et al., 2008; Konrad et al., 2014). Ice-sheet models disregarding geographically variable sea-level changes and complex bedrock deformation will therefore include some degree of error in the predicted ice flow and grounding line migration (Gomez et al., 2013), which will, in turn, affect the interpretation of paleo sea-level records and modern satellite-gravity and geodetic observations of ice-sheet changes.

1.6 Coupled ice-sheet - sea-level modelling

When an ice-sheet model and a sea-level model are coupled to each other, the coupled model can capture the interactions between ice sheets, sea level and the solid Earth (Fig. 1.1). The outputs of the coupled model capture both the physics of ice sheets and sea level and can be directly compared to ice sheet and sea level observations, making the coupled model potentially a powerful research tool.

In a coupled simulation, the ice-sheet and sea-level models exchange their outputs at every coupling time interval dt. The ice-sheet model provides the sea-level model with snapshots of ice thickness at a current model time step t_j. The sea-level model computes gravitationally consistent sea-level changes across the interval $dt = t_j – t_{j-1}$ in response to the past and ongoing ice loading changes. The sea-level model then passes its outputs to the ice-sheet model, and the ice-sheet model updates the elevations of the bedrock and sea surface and then proceeds to predict the ice sheet at the following time step (note that sea level is defined to be the negative of topography in the sea-level theory, Eqn. 1.5). This process continues throughout the simulation (Fig. 1.4).

In coupled modelling, at every current time step t_j when a new snapshot of ice thickness is provided, the sea-level model needs to read in the ice thickness changes that precede the current time step to compute viscoelastic signals associated with past loading changes. The number of the past loading files that the sea-level model needs to read in (the blue bars in 1.4), and along with it the compute time of each step, therefore increase as the simulation progresses. This issue becomes a computational challenge to overcome for simulations that

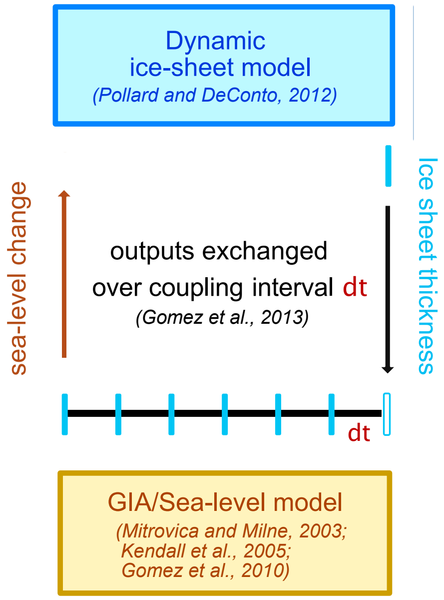

Figure 1.4: A schematic depiction of the general process of coupled ice-sheet - sea-level model coupling

run over longer timescales (e.g., over multiple glacial cycles) or need a higher temporal resolution to capture the short-term (annual to decadal) feedbacks between ice sheets and GIA (particularly for low viscosity regions of WAIS where the solid Earth responds quickly to surface loading). This challenge motivates the development of a time window algorithm in Ch. 4 of this thesis.

Chapter 2

The impact of water loading on postglacial decay times in Hudson Bay

The first study in this thesis starts by investigating how sea level has changed in North America in response to surface ice and water loading changes during the last deglaciation between 21-6 ka, and how the separate effects of ice and water loading changes on sea level influence the interpretation of “postglacial decay times” derived from geological sea level records that have been used to infer mantle viscosity in the Hudson Bay region.

2.1 Abstract

Ongoing glacial isostatic adjustment (GIA) due to surface loading (ice and water) variations during the last glacial cycle has been contributing to sea-level changes globally throughout the Holocene, especially in regions like Canada that were heavily glaciated during the Last Glacial Maximum (LGM). The spatial and temporal distribution of GIA, as manifested in relative sea-level (RSL) change, are sensitive to the ice history and the rheological structure of the solid Earth, both of which are uncertain. It has been shown that RSL curves near the center of previously glaciated regions with no ongoing surface loading follow an exponential-like form, with the postglacial decay times associated with that form having a weak sensitivity to the details of the ice loading history. Postglacial decay time estimates thus provide a powerful datum for constraining the Earth's viscous structure and improving GIA predictions. We explore spatial patterns of postglacial decay time predictions in Hudson Bay by decomposing numerically modeled RSL changes into contributions from water and ice loading effects, and computing their relative impact on the decay times. We demonstrate that ice loading can contribute a strong geographic trend on the decay time estimates if the time window used to compute decay times includes periods that are temporally close to (i.e. contemporaneous with, or soon after) periods of active loading. This variability can be avoided by choosing a suitable starting point for the decay time window. However, more surprisingly, we show that across any adopted time window, water loading effects associated with inundation into, and postglacial flux out of, Hudson Bay and James Bay will impart significant geographic variability onto decay time estimates. We emphasize this issue by considering both maps of predicted decay times across the region and site-specific estimates, and we conclude that variability in observed decay times (whether based on existing or future data sets) may reflect this water loading signal.

2.2 Introduction

Glacial isostatic adjustment (GIA) is defined as the response of the solid Earth surface and gravitational field to ice age surface mass (ice and water) loading. Ongoing GIA associated with the last deglaciation, extending from the Last Glacial Maximum (LGM, ∼21 ka) when ice sheets were at their maximum extent (Clark et al., 2009), to ∼6 ka when major deglaciation ended globally (Denton et al., 2010), has been contributing to sea-level changes throughout the Holocene (i.e. the current interglacial). In regions like North America and Fennoscandia that were heavily glaciated during the LGM, GIA effects make a significant contribution to local sea-level change through solid Earth deformation, but the impact of GIA on sea level is global in extent (Mitrovica and Peltier, 1991).

Constraining the sea-level changes associated with GIA is challenging because the spatial and temporal distributions of these changes are sensitive to the ice history and the rheological structure of the solid Earth, both of which are poorly constrained. One approach to overcoming this challenge is to develop a parameterization of relative sea level i.e., sea level at a time in the past relative to the present (henceforth "RSL"), that are relatively insensitive to the ice history (Andrews, 1970; Cathles, 1975; Forte and Mitrovica, 1996; McConnell, 1968; Mitrovica and Forte, 2004; Mitrovica and Peltier, 1995; Nordman et al., 2015; Walcott, 1972, 1980; Wieczerkowski et al., 1999). (Note that the term RSL is also used in other literature to define the height of sea surface relative to the solid surface, which is what we define here as simply "sea level"). A widely-used example of such a parameterization is the postglacial decay time inferred from RSL curves in previously ice-covered regions.

Postglacial decay times represent, at least in principle, the intrinsic timescale associated with the relaxation of the solid Earth toward isostatic equilibrium after deglaciation (Andrews, 1970; Walcott, 1972, 1980). Pioneering studies (Andrews, 1970; Cathles, 1975; Walcott, 1980) demonstrated that sea-level change after termination of the deglaciation phase in locations near the center of previously ice-covered regions is in free decay (i.e. RSL curves follow an exponential form, see Methods). Subsequent numerical studies have shown that the decay time (or e-folding time) associated with this form is relatively insensitive to ice loading history, and therefore predominantly dependent on mantle viscosity (Lau et al., 2016; Forte and Mitrovica, 1996; Mitrovica et al., 2000; Mitrovica and Peltier, 1993; Nordman et al., 2015). Hence, decay times estimated from RSL histories have been used to constrain mantle viscosity under previously glaciated regions such as Hudson Bay and Fennoscandia, and differences in decay time estimates between sites have been considered potentially indicative of lateral variations in mantle viscosity (e.g. Mitrovica 1996; Mitrovica and Forte, 1997, 2004; Mitrovica and Peltier, 1993, 1995). It is important to note that while decay times are insensitive to the details of the ice history, the maximum depth of mantle at which viscosity profile can be inferred depends on the broad spatial scale of the ice cover at LGM (Mitrovica, 1996).

Decay times have been extensively studied in the Hudson Bay region of North America because the region was straddled by two major domes of the Laurentide Ice Sheet, which covered much of the continent at the LGM. Estimates of decay times at sites in the Hudson Bay region vary widely. For example, Andrews (1970) estimated a decay time of 2 ky for the whole North American region. Walcott (1980) then introduced a modified version of the original methodology developed by Andrews (1970) to take into account uncertainties in absolute age and height of a given geological sea-level record and emphasized the importance of using consistent sea-level markers (e.g., mytilus edilus shells) in determining decay times. He estimated a lower bound on the decay time in southeastern Hudson Bay (i.e. Richmond Gulf and Castle Island) of 5 ky. Peltier (1998) suggested a decay time of 3.4 ky for a region that includes both Richmond Gulf (henceforth RG) and James Bay (henceforth JB). Mitrovica et al. (2000) emphasized the importance of site-specific decay time analysis, showing that a regional decay time estimated by combining RSL data at multiple sites (i.e. calculating a single decay time for a region that includes RG and JB) may be inconsistent with decay times estimated at individual sites. Mitrovica et al. (2000) reappraised decay times at RG and JB with an updated compilation of RSL data, and estimated decay times of between 4-6.6 ky for RG and 2-2.8 ky for JB. Most recently, Lau et al. (2016) computed postglacial decay times of 2.7-4.7 ky for James Bay based on a new RSL curve reconstructed for the last 7 ky by Pendea et al. (2010), who utilized sediments from wetlands in the region.

In addition to the ice loading changes in Hudson Bay, regional RSL has been influenced by a history of surface water loading changes. Hudson Bay became mostly ice-free and inundated with a mix of meltwater and water from the open ocean during the early Holocene (∼9-6 ka) (Dyke 2004). Subsequently, sea level continued to fall in Hudson Bay due to viscous rebound of the solid Earth in response to the collapse of the Laurentide Ice Sheet over the region and viscoelastic deformation in response to ongoing changes in the water loading (Kendall et al., 2005). This water loading perturbs estimates of the decay time associated with the ice collapse in at least two ways. First, it introduces a potentially significant elastic component into the postglacial rebound. Second, it has a spatial scale significantly smaller than the scale of the Laurentide Ice Sheet (i.e. the aerial extent of Hudson Bay is smaller than that of the Laurentide Ice Sheet at the LGM). Both of these effects introduce significant geographic variability in decay times estimated from field data away from an assumption of free decay in response to Laurentide-scale ice unloading.

While many studies have investigated site-specific postglacial decay times in the Hudson Bay region, there has been no analysis of the regional spatial variability of postglacial decay times and how this variability is affected by ongoing water loading in the bay. In this study, we model postglacial sea-level changes over the last 21 ky and compute associated postglacial decay times throughout Hudson Bay. We investigate the spatial pattern of decay times in the region and assess the impact on decay time patterns of both ice and water loading changes during the Holocene (i.e. 8-0 ka). We also consider decay time estimates at a number of individual sites in the region (i.e. Richmond Gulf, James Bay, Churchill, Ottawa Island and Ungava Peninsula), for which there are extensive RSL records (Hardy 1976; Hillaire-Marcel and Fairbridge, 1976) and corresponding decay times analyses in the literature (e.g. Mitrovica et al. 2000; Mitrovica and Forte, 1997; Mitrovica and Peltier, 1995; Peltier, 1994, 1998; Walcott, 1980). Finally, we highlight sites where the impacts of Holocene water and ice loading changes on decay times are minimized that may be ideal for collecting future RSL observations in the bay.

2.3 Methods

Andrews (1970) first approximated the postglacial sea-level change at locations near the center of previously glaciated regions with the following exponential form:

$$SL(t) = Aexp(-\frac{t}{\tau}) \tag{2.1}$$

where τ is the postglacial decay time, $t = 0$ at the present-day, $t < 0$ at a time in the past, and A is the sea-level change remaining at present-day for the system to reach isostatic equilibrium.

Using Equation 2.1, postglacial RSL changes can be approximated by the following expression:

$$RSL(t) = SL(t) - SL(0) = A[exp(-\frac{t}{\tau}) - 1] + c \tag{2.2}$$

where the constant c is an offset that accounts for the uncertainty in present-day absolute age and height of a geological sea-level record (Walcott, 1980). Note that model-generated, synthetic RSL curves are always defined to be zero at present ($t = 0$), which in this case sets the constant c to be zero. One can estimate the postglacial decay time, τ, and remaining sea-level change to reach isostatic equilibrium, A, at a given site by fitting Eqn. 2.2 to the local (modeled or observed) RSL curve.

In order to estimate decay times in Hudson Bay, we generate RSL predictions globally using the postglacial sea-level theory and pseudo-spectral algorithm described in Kendall et al. (2005). Kendall et al. (2005) and Mitrovica and Milne (2003) outline the sea-level theory in detail, and we include the components here that are essential to understanding our methodology. The sea-level theory we implement is gravitationally self-consistent, and it includes migrating shorelines, Earth rotation, and deformation of a Maxwell viscoelastic Earth model with radially varying Earth structure. That is, we solve the generalized sea-level equation (Mitrovica and Milne, 2003; Eqn. 39):

$$\begin{aligned} \Delta S(\theta, \psi, t_j) = {} & \Delta SL(\theta, \psi, t_j)\, C^*(\theta, \psi, t_j) \\ & - T(\theta, \psi, t_0)\,[\,C^*(\theta, \psi, t_j) - C^*(\theta, \psi, t_0)\,], \end{aligned} \tag{2.3}$$

where θ is the colatitude, ψ is the east-longitude, and t_j is the time. The symbol S is the ocean depth, Δ indicates a change in the given field from an initial time t_0 to t_j, SL is globally-defined sea level, T is topography, and C^* is the ocean function defined by the following,

$$C^*(\theta,\psi,t_j) = \begin{cases} 1 & \text{if } SL(\theta,\psi,t_j) > 0 \text{ and there is no grounded ice} \\ 0 & \text{elsewhere.} \end{cases} \tag{2.4}$$

The first term on the right-hand side of Eqn. 2.3, $\Delta SL(\theta,\psi,t_j)$, can be separated into two terms,

$$\Delta SL(\theta,\psi,t_j) = \Delta\mathcal{SL}(\theta,\psi,t_j) + \frac{\Delta\Phi(t_j)}{g}, \tag{2.5}$$

where the first term indicates geographically variable sea-level change due to perturbations in shape of the original gravitational equipotential and solid surfaces defining sea level, and the second term represents a geographically uniform height change of the gravitational equipotential surface constrained by invoking conservation of mass. One can derive the expression for the geographically variable sea-level change, $\Delta\mathcal{SL}(\theta,\psi,t_j)$, using a space-time convolution of the total surface mass (ice and water) loading with the Green's function for sea level (Farrell and Clark, 1976). $\Delta\mathcal{SL}(\theta,\psi,t_j)$ can be represented using viscoelastic Love number theory (Peltier, 1974), and the convolution can be performed analytically to yield (Kendall et al., 2005):

$$\begin{aligned} \Delta\mathcal{SL}(\theta,\psi,t_j) =& \sum_{l,m} T_l E_l \left[\rho_i \Delta I_{lm}(t_j) \;+\; \rho_w \Delta S_{lm}(t_j)\right] Y_{lm}(\theta,\psi) \\ &+ \sum_{l,m} T_l \sum_{n=0}^{j-1} \beta(l,t_n,t_j) \left[\rho_i \delta I_{lm}(t_n) \;+\; \rho_w \delta S_{lm}(t_n)\right] Y_{lm}(\theta,\psi), \end{aligned} \tag{2.6}$$

where l and m are the spherical harmonic degree and order, respectively, Y_{lm}

are spherical harmonic basis functions normalized as discussed in Kendall et al. (2005), $T_l \equiv \frac{4\pi a^3}{M_e(2l+1)}$, M_e and a are the mass and radius of the Earth, and ρ_i and ρ_w are the density of ice and water, respectively. The parameters E_l and β are determined by combining elastic and viscous (or more accurately, non-elastic) components of surface load Love numbers that describe the impulse response of a viscoelastic Earth to loading as a function of harmonic degree l. ΔI and ΔS represent the total change in grounded ice thickness and water depth from t_0 to t_j, whereas the symbol δ represents any change over the time interval from t_{j-1} to t_j. Note that Eqn. 2.3 and 2.6 are integral equations; that is, solving for $\Delta S(\theta, \psi, t_j)$ on the left-hand side of Eqn. 2.3 requires knowledge of $\Delta S_{lm}(t_j)$ on the right-hand side (as in the expression for $\Delta SL(\theta, \psi, t_j)$ in Eqn. 2.6).

Finally, the second, geographically uniform term in Eqn. 2.5 is defined as follows:

$$\begin{aligned}\frac{\Delta\Phi(t_j)}{g} = &-\frac{1}{A(t_j)}\frac{\rho_i}{\rho_w}\iint_\Omega \Delta I(\theta,\psi,t_j)\,d\Omega \\ &-\frac{1}{A(t_j)}\iint_\Omega \Delta\mathcal{SL}(\theta,\psi,t_j)\,C^*(\theta,\psi,t_j)\,d\Omega \\ &+\frac{1}{A(t_j)}\iint_\Omega T(\theta,\psi,t_0)\,[\,C^*(\theta,\psi,t_j)-C^*(\theta,\psi,t_0)\,]d\Omega,\end{aligned} \tag{2.7}$$

where $A(t_j)$ is the ocean area at time t_j, and Ω is the surface of the Earth.

For all calculations in the main text, we adopt the ICE-5G reconstruction of global ice cover changes from 21 ka to the modern (i.e. 0 ka) and the associated VM2 model of 1-D Earth structure (Peltier, 2004). The multi-layer VM2 model has an elastic lithospheric thickness of 90 km, and average upper and lower mantle viscosities of $\sim 5 \times 10^{20}$ and $\sim 2 \times 10^{21}$ Pa S, respectively (Peltier, 2004). The density and elastic structure of the Earth model are given by the seismic model PREM (Dizewonski and Anderson, 1981). We perform calculations up to spherical harmonic degree and order 512, and adopt the etopo2 modern global topography dataset (National Geophysical Data Center, 2006) in our calculations. In the Supplementary material (Figs. S1 2.5 and S22.6) we explore the sensitivity of our results to the adopted ice history by considering an additional simulation with the ICE-6G global ice reconstruction model (Argus et al. 2014; Peltier et al. 2015).

We first perform the sea-level simulation solving the system of equations described above (Eqns. 2.3-2.7) to predict RSL changes associated with the total surface loading changes (both ΔI and ΔS) from 21 ka to the modern. Then, we fit the exponential form of Eqn. 2.2 (with $c = 0$) to a predicted RSL curve at every grid point in the Hudson Bay region to produce maps of decay time estimates. Note that while our results focus on the Hudson Bay region, our sea-level calculations are performed globally. Unless otherwise specified, the RSL curves adopted in the decay time calculations extend back from the modern to 6 ka, encompassing a period in which the deglaciation in North America in the ICE-5G model has ended. We also consider the impact on the decay time estimates of using longer time windows of 7 ky and 8 ky.

In addition to the "full" sea-level simulation described above, we perform another simulation in which we calculate the sea-level variations associated only with ice loading changes over the same time period (i.e. from 21-0 ka) in order to isolate the impact of water loading changes on the decay time estimations. The calculation adopts the following modified expression of Eqn. 2.6:

$$\begin{aligned}\Delta \mathcal{SL}(\theta,\psi,t_j)_{ice} = &\sum_{l,m} T_l E_l \left[\rho_i \Delta I_{lm}(t_j)\right] Y_{lm}(\theta,\psi) \\ &+ \sum_{l,m} T_l \sum_{n=0}^{j-1} \beta(l,t_n,t_j)\left[\rho_i \delta I_{lm}(t_n)\right] Y_{lm}(\theta,\psi),\end{aligned} \tag{2.8}$$

where terms associated with ocean loading changes (ΔS) have been dropped. Additionally, in order to account for meltwater entering the oceans during the time window over which the decay time estimates are made, we approximate the geographically uniform term in the sea-level equation, $\frac{\Delta\phi(t_j)}{g}$, to be the global mean sea-level change (i.e. eustatic change) associated with the change in ocean volume due to loss of grounded ice cover:

$$\frac{\Delta\Phi(t_j)}{g} = \frac{\Delta\Phi_{eus}(t_j)}{g} = -\frac{1}{A(t_j)}\frac{\rho_i}{\rho_w}\iint_{\Omega}\Delta I(\theta,\psi,t_j)\,d\Omega. \tag{2.9}$$

This is a valid approximation because the ice loss over the last 8 ky is relatively far from the Hudson Bay (some ice loss occurs in regions northwest and east of Hudson Bay, and Baffin Island, but most of the ice loss happens in Antarctica and Greenland during this period in the ICE-5G model), and hence the RSL change in Hudson Bay associated with that ice loss is close to the global mean (Mitrovica et al., 2000; Mitrovica Forte, 1997). In solving Eqn. 2.9, we use the present-day area of the ocean for the term A, as we verified that the ocean area does not change significantly over the last 8 ky.

Combining Eqns. 2.8 and 2.9, we predict the total global sea-level change associated with ice loading only using the following equation:

$$\Delta SL(\theta,\psi,t_j)_{ice} = \Delta\mathcal{SL}(\theta,\psi,t_j)_{ice} + \frac{\Delta\Phi_{eus}(t_j)}{g}. \tag{2.10}$$

We then fit Eqn. 2.2 to the predicted RSL curves produced using Eqn. 2.10 to estimate decay times associated with ice loading changes during the last deglaciation, over time windows of the last 6 ky, 7 ky and 8 ky. Finally, we subtract decay times estimated on the basis of Eqn. 2.10 from those associated with the full (ice plus water) loading effects to estimate the contribution to decay times from water loading changes in Hudson Bay.

2.4 Results

2.4.1 Ice cover and RSL since the Last Glacial Maximum in North America

Fig. 2.1 shows ice cover changes (Figs. 2.1a-c) and predictions of RSL in North America (Figs. 2.1d-f) and Hudson Bay (Figs. 2.1g-i) over the last deglaciation associated with the ICE-5G model and the radially varying Earth model VM2 (Peltier, 2004). Ice cover was at its maximum extent globally at the LGM (i.e. 21 ka), and the Laurentide and Cordilleran ice sheets covered much of North America (e.g. Clark et al., 2009; Dyke, 2004). At the LGM in the ICE-5G model (Peltier, 2004), global average sea level is ∼120 m lower than the modern, North American Ice Sheets are up to ∼5200 m thick (Fig. 2.1a), and predicted RSL in ice-covered regions in North America peaks at ∼1200 m (or, equivalently, modeled sea level falls by up to ∼1200 m in the ice-age simulation; Fig. 2.1d). RSL in Hudson Bay at LGM peaks at ∼1000 m on the southwest side of the bay (site Churchill, CH in Fig. 2.1g) and this amplitude falls toward the northeast, reaching ∼500 m at Ottawa Island (site OI in Fig. 2.1g). The James Bay region located southeast of Hudson Bay (site JB in Fig. 2.1g) shows more pronounced RSL change compared with surrounding region. A secondary peak in RSL of 800 m at the LGM occurs near James Bay.

Significant ice-sheet retreat occurs globally from 21-9 ka in the ICE-5G model, and by 9 ka, ice has retreated from most of North America except in the vicinity of Hudson Bay (Fig. 2.1b). At 9 ka, predicted RSL in North America reaches a peak of 570 m to the West of Hudson Bay, and a smaller peak of 360 m is predicted over James Bay (see blue regions in Fig. 2.1e, h). By 6 ka, deglaciation in North America is complete, and the continent is ice-free with the exception of glaciers in Baffin Island that remain to the present day (Fig. 2.1c). RSL in Hudson Bay at 6 ka peaks at 200 m both in James Bay and on the western shore of Hudson Bay (yellow regions in Fig. 2.5i). Comparing Figs. 2.1a and 2.1d-f, note that the pattern of RSL in North America (Fig. 2.1d-f) resembles the pattern of ice cover at the LGM (Fig. 2.1a).

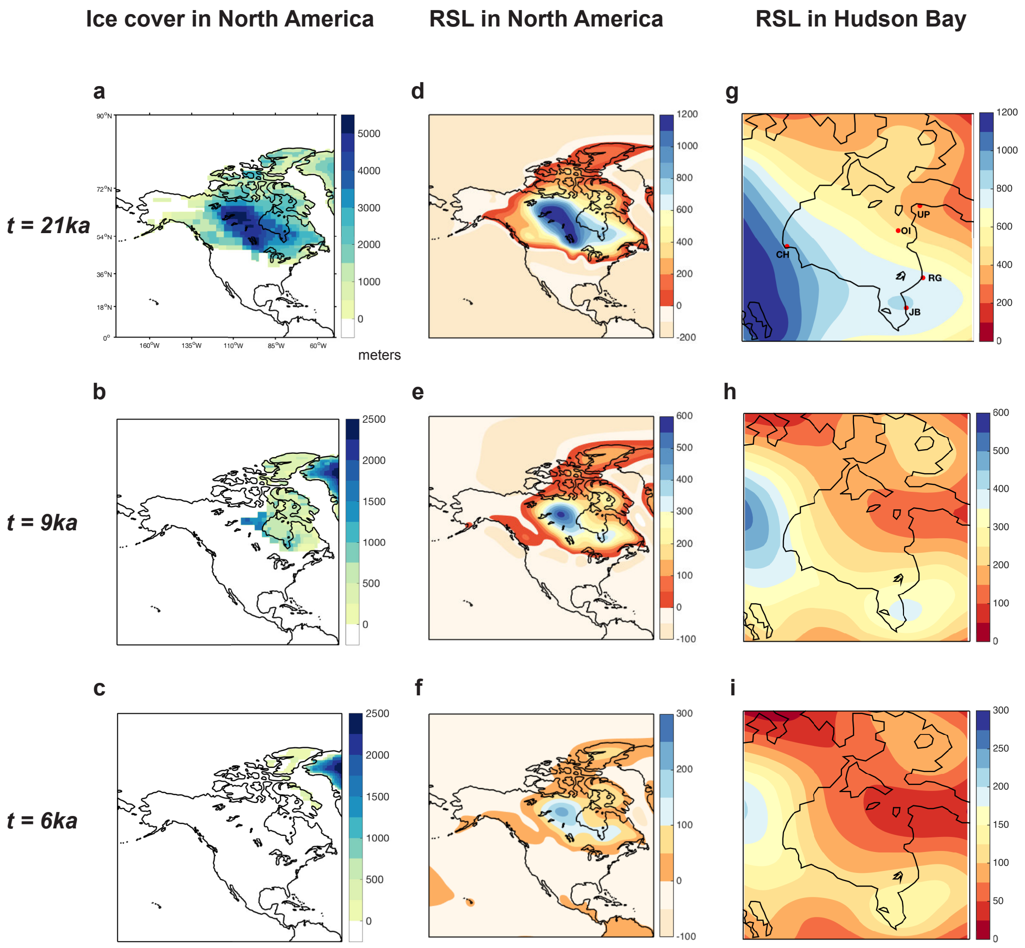

Figure 2.1: Snapshots of ice cover and RSL during the last deglaciation (from 21 ka to 0 ka) in North America and Hudson Bay. (a–c) Ice thickness, in meters, at the indicated times from the ICE-5G (Peltier, 2004) in North America. (d–i) Predicted RSL, in meters, associated with the ICE-5G in (a–c) over North America (d–f) and in Hudson Bay (g–i). Note the changes in color bar limits between rows. Specific sites discussed in the text are marked by labeled red dots (JB = James Bay; RG = Richmond Gulf; CH = Churchill; UP = Ungava Peninsula; and OI = Ottawa Island).

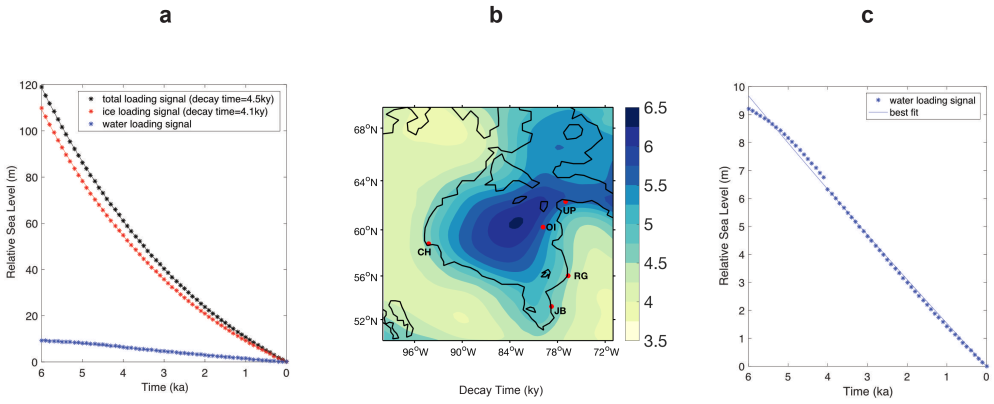

Figure 2.2: Predicted postglacial decay times at Richmond Gulf and in Hudson Bay. (a) Black stars: Predicted RSL curves from 6 ka to the modern at Richmond Gulf (RG) in Hudson Bay, generated from a model simulation of postglacial sea-level changes over the last 21 ky associated with the ICE-5G (Peltier, 2004) that takes the full (ice and water) loading history into account (Eqns. 2.5-2.7). Black lines: Best fitting curve of Eqn. 2.2 to the RSL predictions shown by the black stars. Red lines and stars are equivalent to the black lines and stars, but for a predicted RSL curve associated only with ice loading (see Methods and Eqns. 2.8-2.10). Decay times associated with each fit are indicated in the legend. Blue stars: contribution of water loading to RSL changes, calculated by taking the difference between the black and red stars. Blue lines: Best fitting curve of Eqn. 2.2 to the RSL predictions shown by the blue stars. (b) Map of predicted decay times across the entire Hudson Bay region using a time window over the last 6 ky, produced by applying the method of decay time estimation shown by the black lines and stars of frame (a) at each grid point in the region. Specific sites discussed in the text are marked by labeled red dots. (c) Contribution of water loading changes (blue stars) and the best fitting curve of Eqn. 2.2 to the RSL predictions (blue line).

2.4.2 Estimates of decay times in Hudson Bay

We calculate decay times in Hudson Bay by fitting an exponential form (Eqn. 2.2) to RSL curves predicted from the simulation described in Section 3.1 (Fig. 2.1). Fig. 2.2a shows the RSL curve predicted at the Richmond Gulf (site RG in

Fig. 2.2b) over the last 6 ky. The black stars in Fig. 2.2a represent the predicted RSL from the full (ice and water) loading simulation at RG, and the red stars represent the predicted RSL from the ice loading-only simulation at RG. The solid lines through the stars represent least-squares fits of Eqn. 2.2 to the predicted RSL curves. The best fit to the predicted RSL curve for the full loading (black lines) and ice load (red lines) simulations yield decay times, , of 4.5 ky and 4.1 ky for RG, respectively. In Fig. 2.2b, we extend the decay time calculation shown in Fig. 2.2a to the entire Hudson Bay region. The map shows calculated decay times due to total loading effects (i.e. calculation based on the black curve shown in Fig. 2.2a). A clear spatial pattern emerges in the decay time map in Fig. 2.2b. Predicted decay times in the region are the longest at the center of Hudson Bay, peaking at 6.3 ky, and they shorten moving outwards towards the present-day shoreline. Rather than resembling the ice cover at the LGM, or the pattern of ice loss through deglaciation, the spatial pattern evident in Fig. 2.2b appears to be associated with the geometry of water loading in the region. In the following section, we explore the connection between the ongoing water loading changes in Hudson Bay and predicted decay times, by taking into account the contribution of water loading to predicted RSL curves (e.g. blue stars in Fig. 2.2a and c; note that these curves are identical to each other).

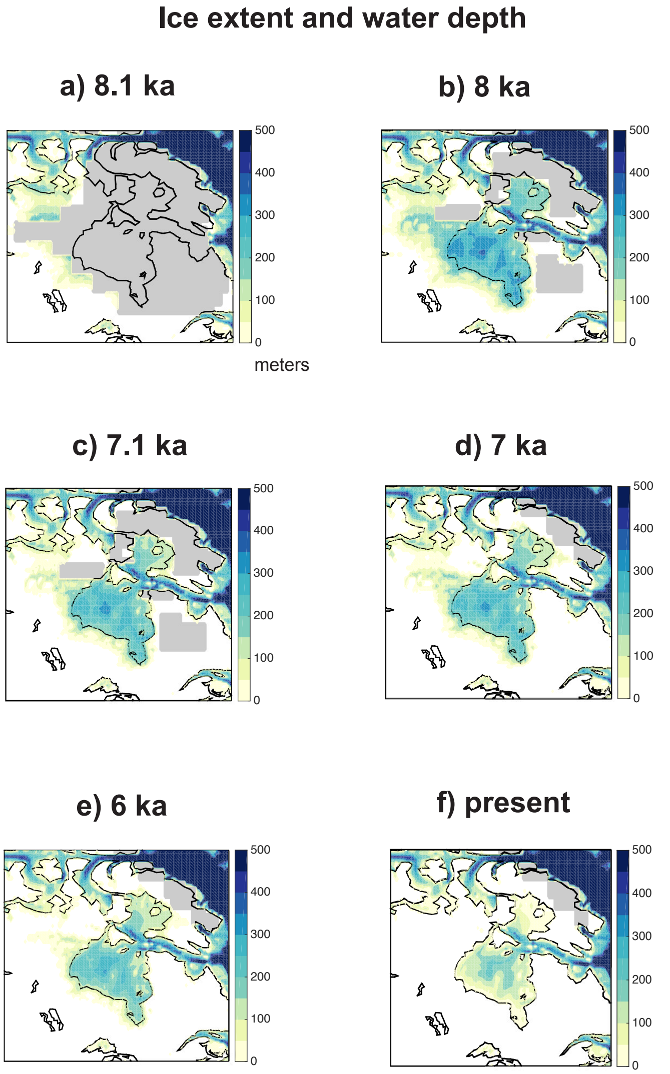

Figure 2.3: Ice extent and absolute water depth in Hudson Bay during and after the end of the deglaciation. Colored contours show water depth, in meters, predicted from the full sea-level simulation (i.e., S on the left-hand side of Eqn. 2.3). Ice covered regions in the ICE-5G are plotted in grey, and the modern shoreline is drawn in black line. Maps are plotted at times indicated above each plot (a) before, (b-d) during and (e-f) after the collapse of the ice cover over Hudson Bay.

2.4.3 Impact of water loading changes on decay time estimations

Fig. 2.3 shows absolute water depth in Hudson Bay at times before (Fig. 2.3a), during (Figs. 2.3b-c) and after (Figs. 2.3d-f) the collapse of ice cover over the bay. Until 8.1 ka in the ICE-5G model, grounded ice is still covering Hudson Bay (grey regions in Fig. 2.3a) and the bay is water-free. As ice cover retreats from Hudson Bay from 8.1 ka to 8 ka, regions freed of marine-based ice are inundated with water at a maximum depth of 390 m. From this time on, uplift of the solid Earth pushes water out of the bay (sea level falls) and the water load monotonically decreases as the shoreline retreats inward.

To examine the impact of the water loading on the decay time predictions, in Fig. 2.4, we decompose the signal shown in Fig. 2.2b, into contributions from ice and water loading. Figs. 2.4a-c show predicted decay times in Hudson Bay for the full sea-level calculation (Eqns. 2.5-2.7; Fig. 2.1 and the black line in Fig. 2.2a), where decay times are computed over time windows extending over the past 6 ky, 7 ky and 8 ky. Note that Fig. 2.4a is identical to Fig. 2b, but with a different color scale. Figs. 2.4d-f show predicted decay times in Hudson Bay attributed to ice loading effects only (e.g. the red line in Fig. 2.2a, see Eqns. 2.8-2.10). Finally, we subtract the decay times associated with ice loading (Figs. 2.4d-f) from those associated with total loading (Figs. 2.4a-c) to assess the impact of water loading changes to the predicted decay times (Figs. 2.4g-i). Note that we cannot calculate this influence by directly fitting the RSL curve associated with the water loading changes to Eqn. 2.2, because water loading is active throughout the time window after deglaciation has terminated and thus the system is not in free decay. This is demonstrated by comparing the blue stars and blue line in Fig. 2.2c, showing the contribution of water loading to RSL changes and the least squares best fit of Eqn. 2.2 to this RSL signal, respectively; the

RSL signal associated with water loading clearly does not follow an exponential decay. In the case of the 6 ky time window (Figs. 2.4a, d, g), the estimated decay times associated with ice unloading (Fig. 2.4d) show little geographic variability, and range from values of ∼3.9 ky along parts of the shoreline of Hudson Bay to 4.3 ky in the center of the bay. This muted variability reflects the fact that the system is in free decay (i.e., all ice unloading in the region is complete) and that the rebound is strongly dominated by the broad spatial scale of the ancient ice cover; the variability that does exist is focused mainly toward the northern sector of the bay, where one moves from Laurentide to Arctic ice cover (see Figs. 2.1a-b). In contrast to the ice loading contribution, water loading effects imprint a more spatially variable signal on the decay time predictions (Figs. 2.4a, g). This signal peaks at ∼1.5 ky along the shoreline of Hudson Bay and up to 2 ky in the center of the bay. We conclude that decay times estimated at sites in the region over a 6 ky time window should show significant geographic variability and that this variability is associated with the impact of water loading on the postglacial rebound of the region.

The remaining rows of Fig. 2.4 explore the impact of increasing the time window on the computed decay times. The estimated decay times in Hudson Bay generally decrease as the time window increases, reflecting a more rapid relaxation toward equilibrium, and the geographic variation in decay times is more strongly affected by variability in the ice loading component. There are two reasons for this increased variability. First, ice is actively retreating from 8-7 ka in the vicinity of Hudson Bay to the northwest and to the east of the bay (see Figs. 2.3c, d), and the elastic response of the solid Earth to this ice unloading will shorten the predicted decay times (compare these regions in Fig. 2.4d to Figs. 42.4e, f). In particular, the areas of active ice unloading from 8-7 ka, are characterized by zones of significantly shorter decay time estimates. In the case of the 8 ky (7 ky) time window, predicted decay times are up to 2.2 ky (1.1 ky) shorter than those predicted using a 6 ky time window (see Supplementary Fig. 2.7). A second reason for the greater geographic variability in the decay times associated with deglaciation is that the Earth's response to load changes is characterized by multiple normal modes with distinct relaxation times (Peltier, 1974; Tromp and Mitrovica, 2000). As one moves away from a period of active ice unloading, the shortest of these decay times will have relaxed out of the system. Conversely, as the time window is increased, decay time estimates in regions close to the most recent ice load changes will be impacted more significantly by such modes. Hence some of the difference between Figs. 2.4d and 2.4f is attributed to natural lengthening of the decay time of the Earth deformation with time after unloading (Mitrovica et al. 2000).

We conclude from the above, that the geographic variability in the decay times estimated using a time window of 8 ky will have a significant signal associated with the response of the solid Earth to ice unloading in the earliest portions of the time window. To avoid this variability, one would have to reduce the time window to less than 7 ky, although this would of course reduce the number of RSL observation data points that can be included to estimate decay times (Mitrovica et al., 2000). However, even in this case, the decay times estimated from observation data across Hudson Bay (or model-predictions of these decay times) will have a significant geographic variability arising from water loading effects that cannot be avoided. It is interesting to note that the geometry of this impact follows the details of the shorelines of Hudson Bay and James Bay as one shortens the time window (compare Fig. 2.4g to Fig. 2.8, which shows the same field as Fig. 2.4i with a finer color scale). This is due to the increased importance of viscous effects relative to elastic effects as one moves further in time from the original inundation of these areas when they become ice free at

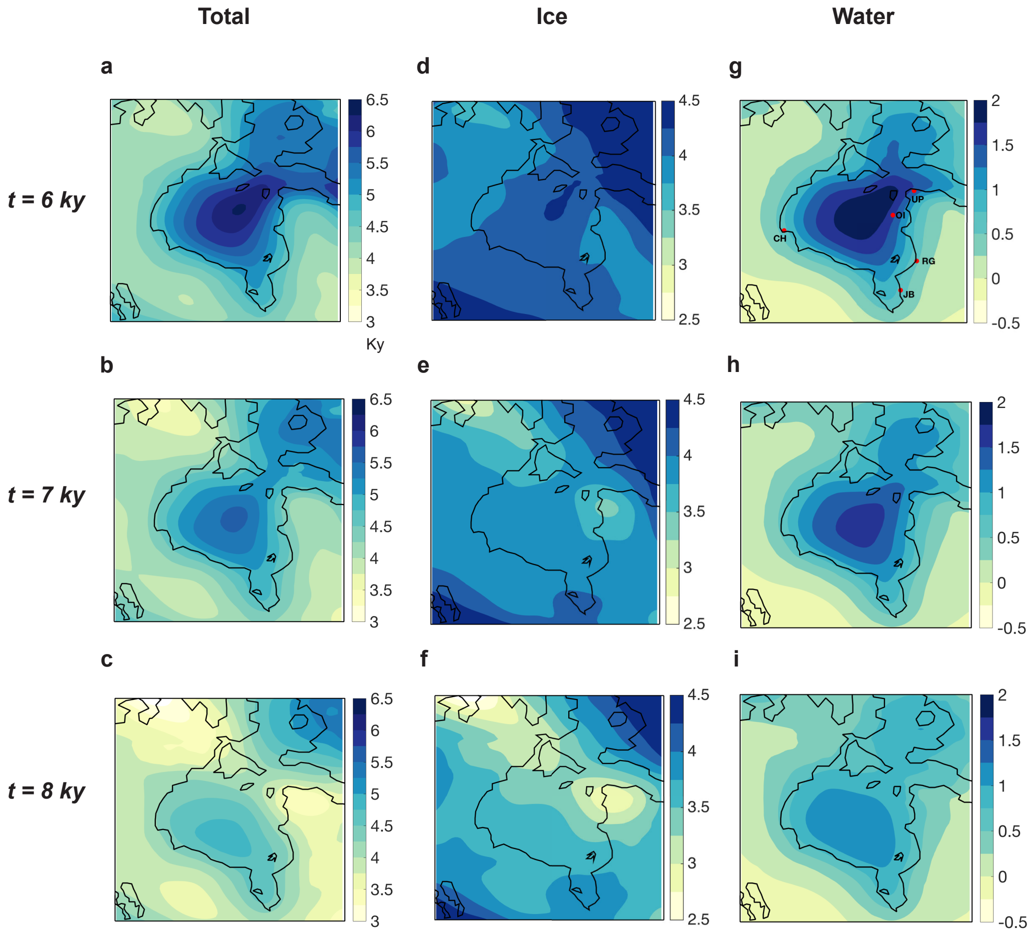

Figure 2.4: Maps of postglacial decay times in Hudson Bay, decomposed into the contribution from ice and water loading effects. Decay times are calculated by fitting Eqn. 2.2 to RSL predictions over time windows ranging from the last 8 ky to 6 ky as labeled. (a-c) represent decay times, in ky, calculated from RSL curves predicted from the full sea-level simulation (Eqns. 2.5-2.7) that accounts for both ice and water loading effects over the last 21 ky. Note that frame (a) is identical to Fig. 2.2b. (d-f) represent decay times calculated from predicted RSL curves associated with ice loading changes only (i.e. calculated using Eqns. 2.8-2.10). (g-i) show the difference between frames (a-c) and frames (g-f), representing the perturbation in the free decay estimates due to water loading changes.

∼8 ka. We note that Mitrovica and Forte (1997) emphasize the need to consider possible contamination of RSL curves associated with ongoing melting of ice sheets outside of the Hudson Bay region (e.g. Greenland and Antarctica), adding meltwater to the oceans during the time window of the decay time calculation. In Supplementary Fig. 2.9, we explore the spatial pattern of the impact of meltwater entering the ocean on decay time estimates. We demonstrate, as suggested by Mitrovica and Forte (1997) and Mitrovica et al. (2000), that this effect can significantly bias decay time estimates based on the assumption of free decay, particularly in regions with smaller magnitude RSL changes (Fig. 2.1h-i).

2.4.4 Site-Specific Decay Time Analysis

Table 2.1 explores the size of decomposed surface loading effects on decay times arising at specific sites in Hudson Bay. We choose five sites where there are available RSL records and decay time analyses based on the sites in previous literature (e.g. Mitrovica et al., 2000; Richmond Gulf (RG), Churchill (CH), James Bay (JB), Ungava Peninsula (UP), and Ottawa Island (OI): marked as dots in Fig. 2.2b). The first column of Table 2.1 (τ_t) shows the estimated site-specific decay times associated with the full deglacial ice and water loading history using a 6 ky time window, while the second and third columns show contribution to the total from ice (τ_i) and water (τ_w) loading effects, respectively.

Site specific decay times t vary by 1.2 ky, between 4.5 and 5.7 ky across the sites, while decay times associated with ice loading τ_i vary by only 300 years from 4.0 to 4.3 ky. This suggests that the Earth system underneath Hudson Bay is in free decay at a relatively geographically uniform rate in the absence of water loading. This is due to the much broader spatial scale of the deglacial ice loading changes relative to the water loading signal. The contamination of the free decay time estimates due to the water loading effects peaks in the center of the

Table 2.1: Site specific estimates of decay times and the contributions of water and ice loading effects at individual sites in Hudson Bay. Columns labeled τ_t, τ_i, and τ_w represent decay times, in ky, attributed to total surface (ice plus water) loading effects, ice loading effects only, and water loading effects only (see Methods). Columns labeled "$\frac{\tau_w}{\tau_t}$" represent the percent bias in the total decay τ_t (calculated based on the assumption of free decay), from water loading effects (i.e. $\frac{\tau_w}{\tau_t} * 100\%$). The site names are as follows: RG=Richmond Gulf; CH=Churchill; JB=James Bay; OI=Ottawa Island; UP=Ungava Peninsula.

t and τ	$t = 6$ ky				$t = 7$ ky				$t = 8$ ky			
Sites	τ_t	τ_i	τ_w	$\frac{\tau_w}{\tau_t}$ (%)	τ_t	τ_i	τ_w	$\frac{\tau_w}{\tau_t}$ (%)	τ_t	τ_i	τ_w	$\frac{\tau_w}{\tau_t}$ (%)
RG	4.5	4.1	0.4	9	4.4	3.9	0.5	11	4.1	3.7	0.4	10
CH	4.6	4.0	0.6	13	4.5	3.9	0.6	13	4.3	3.7	0.6	19
JB	4.7	4.1	0.6	13	4.6	4.0	0.6	13	4.4	3.8	0.6	14
OI	5.7	4.1	1.6	28	4.9	3.7	1.3	27	4.1	3.2	0.9	22
UP	5.7	4.3	1.4	25	4.7	3.7	1.0	21	3.6	3.0	0.6	16

bay at ~30% and decreases smoothly moving towards the present-day shoreline. However, the position of the shoreline of Hudson Bay varies unevenly at a much smaller spatial scale, crossing the contours of the decay time pattern (See Fig. 2.4g). The decay time of sites along the shoreline will be perturbed upwards by 400-1600 years due to the impact of water loading on the sea-level prediction. The estimated total decay times in sites like OI and UP are biased upwards by the water loading effects by more than 1 ky, or ~27% of the total, while the estimates in RG, CH and JB are relatively weakly biased by ~500 years, or ~12% of the total. The water loading effects are the lowest along the eastern and southern shoreline of Hudson Bay and James Bay, respectively. Previous studies have estimated different decay times at different sites in the bay. Mitrovica et al. (2000) hypothesize that these differences may reflect errors in observational RSL records or lateral variations in Earth structure in Hudson Bay. Our results indicate that the difference in predicted decay times between sites in the bay may have a contribution from water loading effects.

At all five sites, predicted decay times attributed to total loading effects (τ_t in Table 2.1) and those attributed to ice loading effects (τ_i in Table 2.1) decrease as the time window extends further into the past. However, the perturbation in the decay time estimates due to water loading effects (τ_w in Table 2.1) remains relatively constant at sites near the edge of the bay as the time window is extended, even though the maximum bias in the center of the bay decreases (see Figs. 2.4g-i). OI and UP are the exceptions, with the perturbation to free decay time estimates attributed to water loading effects dropping significantly from 1.6 ky to 1.3 ky and from 1.4 ky to 1 ky, respectively, as the time window is extended from 6 ky to 7 ky. This is because these sites are covered by or near ice until 7.1 ka. Ice near RG, CH and JB disappears between 8.1-8 ka, and estimated decay times with an 8 ky time window at these sites are impacted by an instantaneous elastic response of the solid Earth immediately following the deglaciation. These results suggest that the optimal time window to adopt in the decay time calculation will vary among sites.

2.5 Discussion and Conclusions

Holocene RSL changes in Hudson Bay are the result of a combination of ongoing adjustment of the solid Earth and gravitational field in response to i) past ice unloading during the deglaciation (∼21-7 ka in the ICE-5G), ii) influx of water as Hudson Bay becomes ice-free (around 8 ka in the ICE-5G), and iii) water redistribution throughout the Holocene (i.e. after deglaciation in the region finishes, ∼7 ka-modern in the ICE-5G). Previous analyses (e.g. Andrews, 1970; Lau et al., 2016; Mitrovica et al., 2000; Mitrovica and Forte, 1997; Mitrovica and Peltier, 1993, 1995; Peltier, 1998; Walcott, 1980) have considered site-specific postglacial decay time estimates associated with Holocene RSL changes. We produce maps, for the first time, that show the spatial patterns of decay time predictions across the entire Hudson Bay region. We also estimate the contributions of ice and water loading to sea-level predictions since the Last Glacial Maximum (21 ka), and in turn consider their impacts on decay time predictions in Hudson Bay. Our results indicate that water loading changes over the last deglaciation can contaminate the free decay time estimates by up to 1.6 ky, when the decay times are computed over the last 6 ky along the shoreline of Hudson Bay (i.e. 5.7 ky at site OI, see Fig. 2.4a, g and Table 2.1). Furthermore, Fig. 2.4 and Table 2.1 indicate that water loading effects in our simulations vary along the shoreline of the bay by up to 1.1 ky, and that without the signal associated with water loading, predicted decay times are relatively geographically uniform along the shoreline of Hudson Bay (see τ_i in Table. 2.1).

We also show that decay time estimates are dependent on the choice of time window over which the calculations are made. We find that decay time estimates using a time window that spans the last 8 ky or 7 ky are lower than those adopting a 6 ky time window by up to 2.2 ky and 1.1 ky, respectively (see Figs. 2.4a-c and Supplementary Fig. 2.7). These differences are associated with the solid Earth deforming elastically in response to recent or ongoing surface loading changes in the calculations adopting a longer time window, as well as the natural tendency for decay times to lengthen with time after loading. Previous studies have adopted time windows over the last 6-10 ky, depending on the availability of RSL data at the sites being investigated (Lau et al., 2016; Mitrovica and Forte, 1997; Mitovica and Peltier, 1993, 1995; Mitrovica et al., 2000; Peltier, 1998). We emphasize that these observation-based decay-time estimates will be associated with the time span of the data, and not necessarily represent the decay time at the modern. Expanding on the work of Mitrovica et al. (2000), the decay time maps in Fig. 2.4 highlight that there will be significant geographic variability in decay time estimates calculated over time windows during which deglaciation in the region is ongoing, particularly in locations close to active or recent ice loss.

While the decay time parameter is considered relatively independent of ice history (Forte and Mitrovica 1996; Mitrovica et al., 2000; Mitrovica and Peltier, 1993; Nordman et al., 2015), it is important to note that this is only true when the parameters are calculated over a time window that truly excludes the elastic deformation associated with ice loading. Recent studies suggest that the Laurentide ice history is particularly ill-constrained during the end of the last deglaciation as the ice makes its final retreat over Hudson Bay through Hudson Strait (Carlson et al., 2007; Dyke, 2004; Simon et al., 2014, 2016; Ullman et al., 2016; Wickert et al., 2013; Wickert, 2016). More observational constraints on the ice and sea-level evolution (e.g. Engelhart et al., 2012, 2015; Hawkes et al., 2016; Khan et al., 2015), and ice-sheet modeling studies (e.g. Gregoire et al., 2012; Matero et al., 2017; Roy and Peltier, 2017; Stokes and Tarasov, 2012; Tarasov et al., 2012) focused on Hudson Bay during and after the end of North American deglaciation would aid in accounting for the effects of recent loading on decay time estimates.

More generally, this study highlights that the effects of recent (i.e. last 8 ky) ice and water loading changes should be taken into account in future studies and in the interpretation of decay time estimates in the literature. Note that previous analyses comparing observed decay times to decay times predicted on the basis of a full sea-level theory (i.e. Eqns. 2.5-2.7) account for the effects of ocean loading implicitly. Fig. 2.4 and Table 2.1 may be used to assess the degree to which water loading and recent ice loading perturb solid Earth uplift away from free decay at sites throughout the Hudson Bay region. We note that both effects are minimized along the southern shore of the bay (e.g. at RG, JB and CH), making this an ideal region for future decay time analyses.

2.6 Supplementary material

In order to explore the sensitivity of results presented in the main text to the adopted ice history, we perform additional simulations with the newer ICE-6G ice history model (Argus et al. 2014; Peltier et al. 2015), but keeping the adopted Earth model the same (i.e. using Earth model VM2, associated with ICE-5G, rather than VM5a, associated with ICE-6G). Supplementary Figures 2.5 and 2.6 show the results of these additional simulations, and are equivalent to Figures 2.3 and 2.4 of the main text.

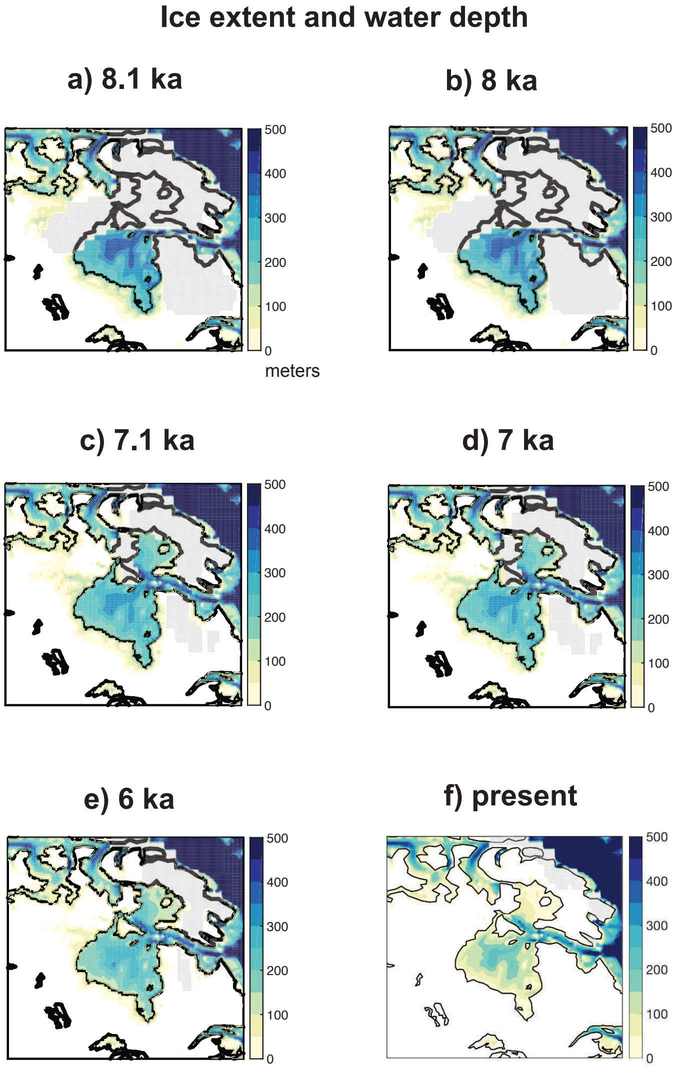

Figure 2.5: Ice extent and absolute water depth in Hudson Bay during and after the end of the deglaciation from the modified simulation based on the ICE-6G and VM2. Colored contours show water depth, in meters, predicted from the full sea-level simulation (i.e., S on the LHS of Eqn. 2.3). Ice-covered regions in the ICE-6G are plotted in grey, and the modern shoreline is drawn in black line. Maps are plotted at times indicated above each plot (a) before, (b-d) during and (e-f) after the collapse of the ice cover over Hudson Bay

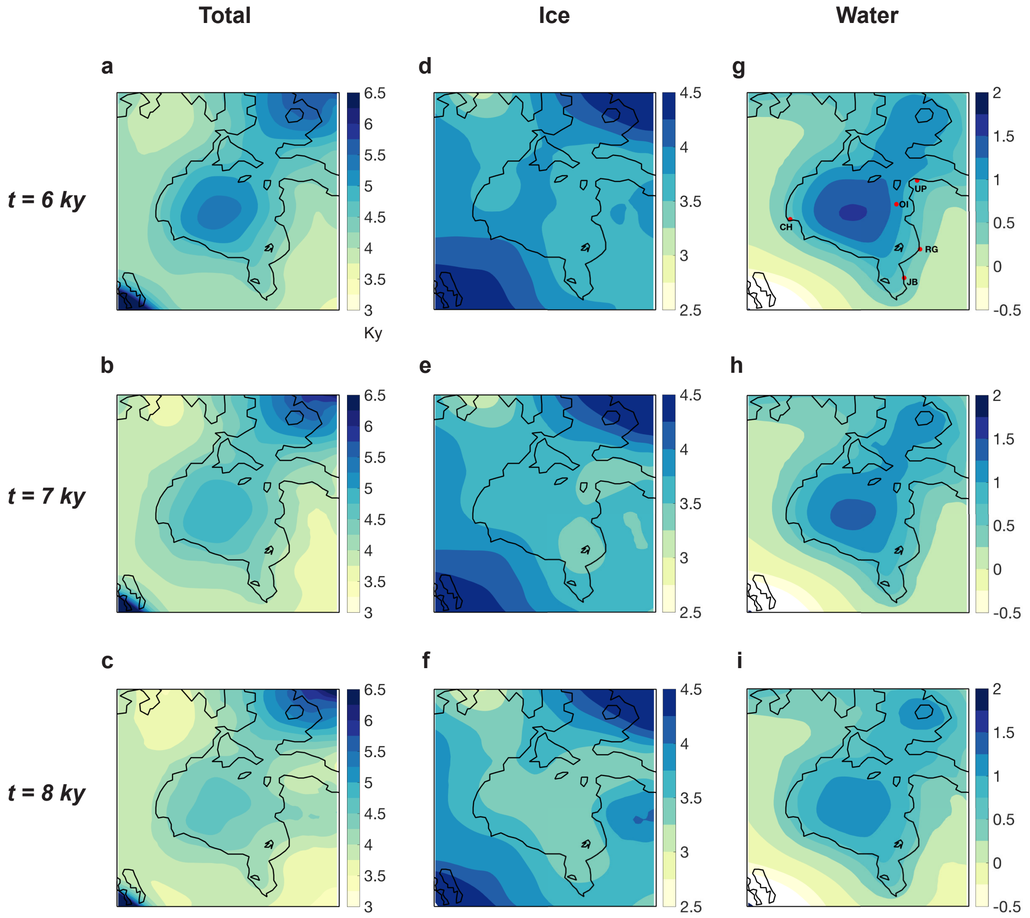

Figure 2.6: Maps of postglacial decay times in Hudson Bay associated with the modified simulation based on the ICE-6G model with Earth model VM2, decomposed into the contributions from ice and water loading effects. Decay times are calculated by fitting Eqn. 2.2 to RSL predictions over time windows ranging from the last 8 ky to 6 ky as labeled. (a-c) represent decay times, in ky, calculated from RSL curves predicted from the full sea-level simulation (Eqns. 2.5-2.7) that accounts for both ice and water loading effects over the last 21 ky. (d-f) represent decay times calculated from predicted RSL curves associated with ice loading changes only (i.e. calculated using Eqns. 2.8-2.10). (g-i) show the difference between frames (a-c) and frames (g-f), representing the contribution of water loading effects to the decay times.

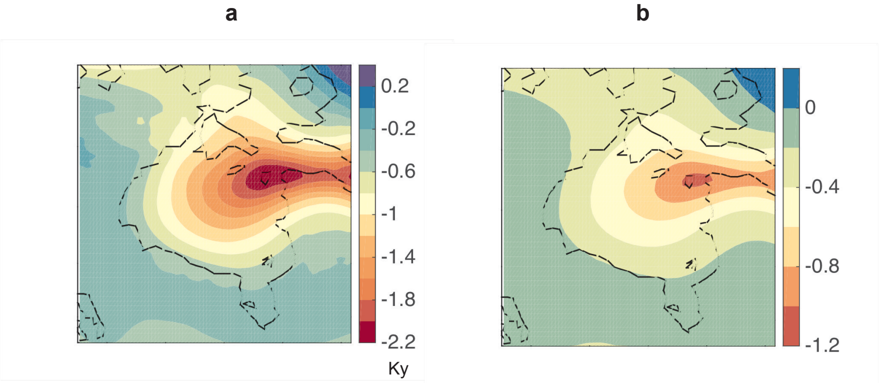

Figure 2.7: Maps of the difference between decay times estimated using RSL predictions over time windows of the last (a) 8 ky and 6 ky, (b) 7 ky and 6 ky, in ky. Black lines indicate the present-day shoreline.

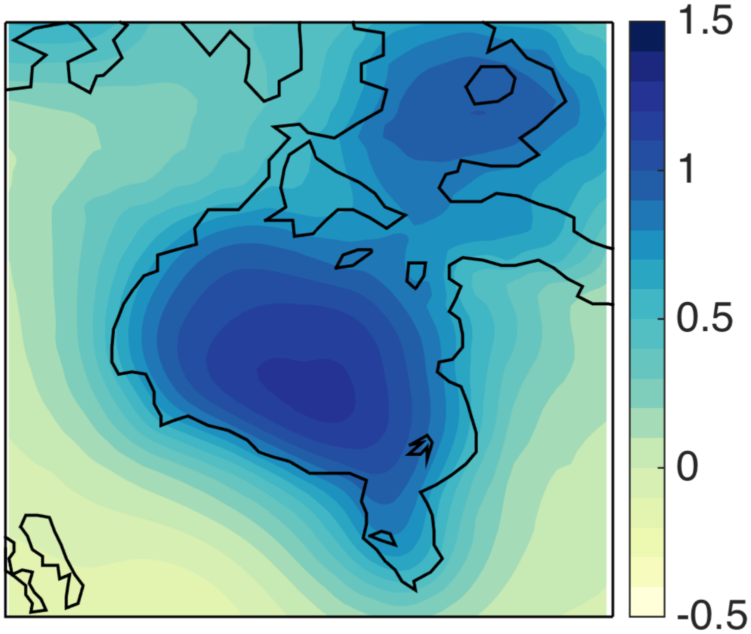

Figure 2.8: This supplementary figure is identical to Fig. 2.4i, but with a finer color scale that highlights the geometry of the signal relative to the geometry of the bay.

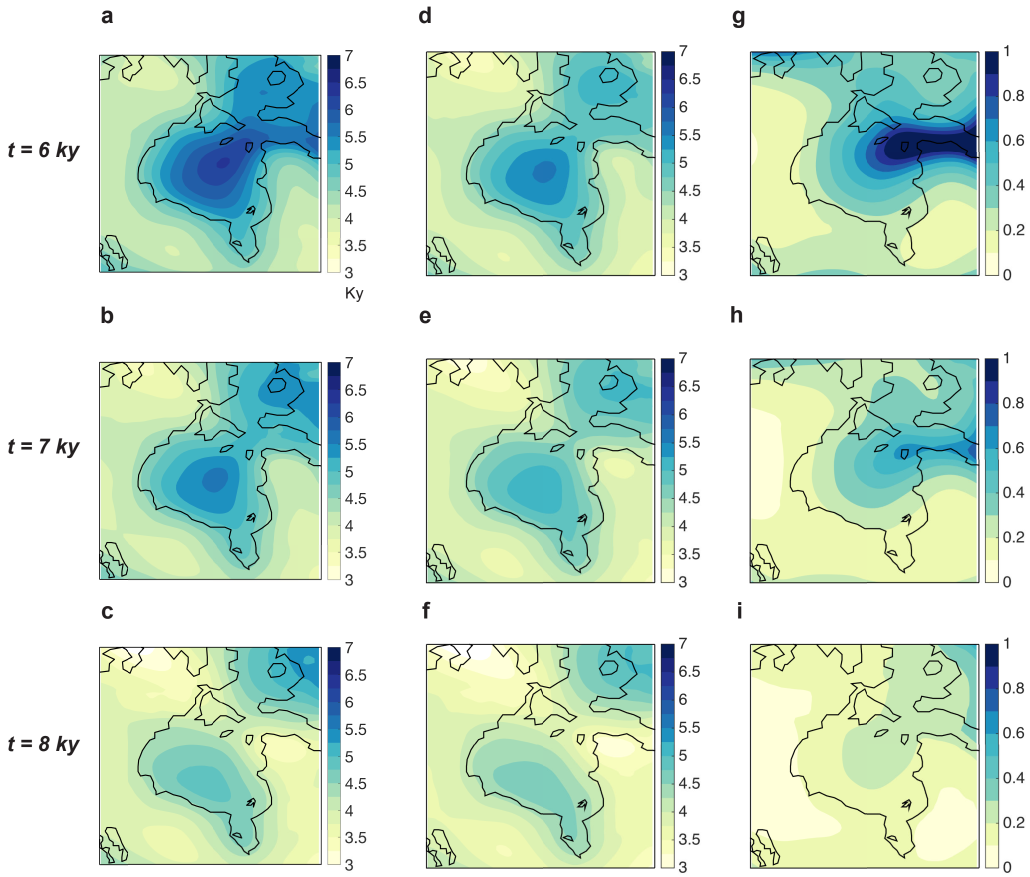

Figure 2.9: The contribution of meltwater associated with ongoing melting of Late Pleistocene ice sheets entering the ocean (henceforth the "eustatic contribution") to postglacial decay times in Hudson Bay. (a-c) represent decay times, in ky, calculated from RSL curves predicted from the full sea-level simulation that accounts for both ice and water loading effects over the last 21 ky, and are identical to frames (a-c) of Fig. 2.4 in the main text. (d-f) represent decay times attributed to total (ice and water) loading changes corrected for the eustatic contribution (Mitrovica et al., 2000), calculated by subtracting the contribution from eustatic sea-level change (Eqn. 2.9) to RSL from the full (Eqns. 2.5-2.7) RSL calculation. (g-i) show the difference between frames (a-c) and frames (d-f), approximating the contribution of eustatic effects to the decay times. Note that the eustatic contribution is particularly large in regions where RSL changes are small (i.e. compare dark blue regions in frame (g) to red and orange regions in Fig. 2.1i of the main text).

References

[1] Andrews, J. T., A Geomorphological Study of Post-Glacial Uplift with Particular Reference to Arctic Canada, *Oxford University Press, New York*, doi:10.2307/1796773, 1970.

[2] Argus, D. F., W. R. Peltier, R. Drummond, and A. W. Moore, The Antarctica component of postglacial rebound model ICE-6G_C (VM5a) based on GPS positioning, exposure age dating of ice thicknesses, and relative sea level histories, *Geophysical Journal International*, *198*(1), 537–563, doi: 10.1093/gji/ggu140, 2014.

[3] Carlson, A. E., P. U. Clark, G. M. Raisbeck, and E. J. Brook, Rapid holocene deglaciation of the labrador sector of the Laurentide Ice Sheet, *Journal of Climate*, *20*, 5126–5133, doi:10.1175/JCLI4273.1, 2007.

[4] Cathles, L., The Viscosity of the Earth's Mantle. Princeton Univ. Press, N.J., *Princton Univ. Press. N.J.*, 1975.

[5] Clark, P. U., A. S. Dyke, J. D. Shakun, A. E. Carlson, J. Clark, B. Wohlfarth, J. X. Mitrovica, S. W. Hostetler, and A. M. McCabe, The Last Glacial Maximum, *Science*, *32*, 710–714, doi:10.1126/science.1172873, 2009.

[6] Denton, G. H., R. F. Anderson, J. R. Toggweiler, R. L. Edwards, J. M.

Schaefer, and A. E. Putnam, The last glacial termination, *Science*, *328*, 1652–1656, doi:10.1126/science.1184119, 2010.

[7] Dyke, A. S., An outline of North American deglaciation with emphasis on central and northern Canada, *Developments in Quaternary Sciences*, *2*, 373–424, doi:10.1016/S1571-0866(04)80209-4, 2004.

[8] Dziewonski, A. M., and D. L. Anderson, Preliminary reference Earth model, *Phys. Earth Planet. Inter*, *25*(4), 297–356, 1981.

[9] Engelhart, S. E., and B. P. Horton, Holocene sea level database for the Atlantic coast of the United States, *Quaternary Science Reviews*, *54*, 12–25, doi:10.1016/j.quascirev.2011.09.013, 2012.

[10] Engelhart, S. E., M. Vacchi, B. P. Horton, A. R. Nelson, and R. E. Kopp, A sea-level database for the Pacific coast of central North America, *Quaternary Science Reviews*, *113*, 78–92, doi:10.1016/j.quascirev.2014.12.001, 2015.

[11] Farrell, W. E., and J. A. Clark, On Postglacial Sea Level, *Geophysical Journal of the Royal Astronomical Society*, *46*, 64–667, doi:10.1111/j.1365-246X.1976.tb01252.x, 1976.

[12] Forte, A. M., and J. X. Mitrovica, New inferences of mantle viscosity from joint inversion of long-wavelength mantle convection and post-glacial rebound data, *Geophysical Research Letters*, *23*, 1147–1150, doi:10.1029/96GL00964, 1996.

[13] Gregoire, L. J., A. J. Payne, and P. J. Valdes, Deglacial rapid sea level rises caused by ice-sheet saddle collapses, *Nature*, *487*, 219–222, doi:10.1038/nature11257, 2012.

[14] Hardy, L., Contribution a l'étude geomorphologique de la portion Quebecoise de la Baie de James, *PhD thesis. McGill University, Montreal*, 1976.

[15] Hawkes, A. D., A. C. Kemp, J. P. Donnelly, B. P. Horton, W. R. Peltier, N. Cahill, D. F. Hill, E. Ashe, and C. R. Alexander, Relative sea-level change in northeastern Florida (USA) during the last ˜8.0 ka, *Quaternary Science Reviews*, *142*, 90–101, doi:10.1016/j.quascirev.2016.04.016, 2016.

[16] Hillaire-Marcel, C., and R. W. Fairbridge, Isostasy and eustasy of Hudson Bay, *Geology*, *6*(2), 117–122, doi:10.1130/0091-7613(1978)6⟨117:IAEOHB⟩2.0.CO;2, 1978.

[17] Kendall, R. A., J. X. Mitrovica, and G. A. Milne, On post-glacial sea level - II. Numerical formulation and comparative results on spherically symmetric models, *Geophysical Journal International*, *161*(3), 679–706, doi:10.1111/j.1365-246X.2005.02553.x, 2005.

[18] Khan, N. S., E. Ashe, T. A. Shaw, M. Vacchi, J. Walker, W. R. Peltier, R. E. Kopp, and B. P. Horton, Holocene Relative Sea-Level Changes from Near-, Intermediate-, and Far-Field Locations, *Current Climate Change Reports*, *1*, 247–262, doi:10.1007/s40641-015-0029-z, 2015.

[19] Lau, H. C., J. X. Mitrovica, J. Austermann, O. Crawford, D. Al-Attar, and K. Latychev, Inferences of mantle viscosity based on ice age data sets: Radial structure, *Journal of Geophysical Research: Solid Earth*, *121*, 6991–7012, doi:10.1002/2016JB013043, 2016.

[20] Matero, I. S., L. J. Gregoire, R. F. Ivanovic, J. C. Tindall, and A. M. Haywood, The 8.2 ka cooling event caused by Laurentide ice saddle collapse, *Earth and Planetary Science Letters*, *273*, 205–214, doi:10.1016/j.epsl.2017.06.011, 2017.

[21] McConnell R. K., Viscosity of the mantle from relaxation time spectra of isostatic adjustment, *J Geophysical Research*, *73*, 7089–7105, doi:10.1029/jb073i022p07089, 1968.

[22] Mitrovica, J. X., Haskell [1935] revisited, *Journal of Geophysical Research B: Solid Earth*, *101*, 555–569, doi:10.1029/95jb03208, 1996.

[23] Mitrovica, J. X., and A. M. Forte, Radial profile of mantle viscosity: Results from the joint inversion of convection and postglacial rebound observables, *Journal of Geophysical Research: Solid Earth*, *102*, 2751–2769, doi:10.1029/96jb03175, 1997.

[24] Mitrovica, J. X., and A. M. Forte, A new inference of mantle viscosity based upon joint inversion of convection and glacial isostatic adjustment data, *Earth and Planetary Science Letters*, *225*(1), 177–189, doi:10.1016/j.epsl.2004.06.005, 2004.

[25] Mitrovica, J. X., and G. A. Milne, On post-glacial sea level: I. General theory, *Geophysical Journal International*, *154*(2), 253–267, doi:10.1046/j.1365-246X.2003.01942.x, 2003.

[26] Mitrovica, J. X., and W. R. Peltier, On postglacial geoid subsidence over the equatorial oceans, *Journal of Geophysical Research*, *96*(B12), 20,053–20,071, doi:10.1029/91jb01284, 1991.

[27] Mitrovica, J. X., and W. R. Peltier, A new formalism for inferring mantle viscosity based on estimates of post glacial decay Times: Application to RSL variations in N.E. Hudson Bay, *Geophysical Research Letters*, *20*, 2183–2186, doi:10.1029/93GL02136, 1993.

[28] Mitrovica, J. X., and W. R. Peltier, Constraints on mantle viscosity based upon the inversion of post-glacial uplift data from the Hudson Bay region,

Geophysical Journal International, *122*, 353–377, doi:10.1111/j.1365-246X.1995.tb07002.x, 1995.

[29] Mitrovica, J. X., A. M. Forte, and M. Simons, A reappraisal of postglacial decay times from Richmond Gulf and James Bay, Canada, *Geophysical Journal International*, *142*, 783–800, doi:10.1046/j.1365-246X.2000.00199.x, 2000.

[30] National Geophysical Data Center, 2-minute Gridded Global Relief Data (ETOPO2) v2, 2006.

[31] Nordman, M., G. Milne, and L. Tarasov, Reappraisal of the Ångerman River decay time estimate and its application to determine uncertainty in Earth viscosity structure, *Geophysical Journal International*, *201*, 811–822, doi:10.1093/gji/ggv051, 2015.

[32] Peltier, W. R., The impulse response of a Maxwell Earth, *Reviews of Geophysics*, *12*, 649–669, doi:10.1029/RG012i004p00649, 1974.

[33] Peltier, W. R., Ice age paleotopography, *Science*, *265*, 195–201, doi:10.1126/science.265.5169.195, 1994.

[34] Peltier, W. R., Postglacial variations in the level of the sea: Implications for climate dynamics and solid-earth geophysics, *Reviews of Geophysics*, *36*, 603–689, doi:10.1029/98RG02638, 1998.

[35] Peltier, W. R., Global glacial isostasy and the surface of the ice-age earth: The ICE-5G (VM2) model and GRACE, *Annual Review of Earth and Planetary Sciences*, *32*, 111–149, doi:10.1146/annurev.earth.32.082503.144359, 2004.

[36] Peltier, W. R., D. F. Argus, and R. Drummond, Space geodesy constrains ice age terminal deglaciation: The global ICE-6G_C (VM5a) model,

Journal of Geophysical Research: Solid Earth, *120*, 450–487, doi:10.1002/2014JB011176, 2015.

[37] Pendea, I. F., A. Costopoulos, C. Nielsen, and G. L. Chmura, A new shoreline displacement model for the last 7 ka from eastern James Bay, Canada, *Quaternary Research*, *73*(3), 474–484, doi:10.1016/j.yqres.2010.02.001, 2010.

[38] Roy, K., and W. R. Peltier, Space-geodetic and water level gauge constraints on continental uplift and tilting over North America: Regional convergence of the ICE-6G C (VM5a/VM6) models, *Geophysical Journal International*, *210*(1115-1142), doi:10.1093/gji/ggx156, 2017.

[39] Simon, K. M., T. S. James, D. L. Forbes, A. M. Telka, A. S. Dyke, and J. A. Henton, A relative sea-level history for Arviat, Nunavut, and implications for Laurentide Ice Sheet thickness west of Hudson Bay, *Quaternary Research (United States)*, *82*(185-197), doi:10.1016/j.yqres.2014.04.002, 2014.

[40] Simon, K. M., T. S. James, J. A. Henton, and A. S. Dyke, A glacial isostatic adjustment model for the central and northern Laurentide ice sheet based on relative sea level and GPS measurements, *Geophysical Journal International*, *205*, 1818–1636, doi:10.1093/gji/ggw103, 2016.

[41] Stokes, C. R., L. Tarasov, and A. S. Dyke, Dynamics of the North American Ice Sheet Complex during its inception and build-up to the Last Glacial Maximum, *Quaternary Science Reviews*, *50*, 86–104, doi:10.1016/j.quascirev.2012.07.009, 2012.

[42] Tarasov, L., A. S. Dyke, R. M. Neal, and W. R. Peltier, A data-calibrated distribution of deglacial chronologies for the North American ice complex from glaciological modeling, *Earth and Planetary Science Letters*, *140*, 425–441, doi:10.1016/j.epsl.2011.09.010, 2012.

[43] Tromp, J., and J. X. Mitrovica, Surface loading of a viscoelastic planet-III. Aspherical models, *Geophysical Journal International*, *140*, 425–441, doi: 10.1046/j.1365-246x.2000.00027.x, 2000.

[44] Ullman, D. J., A. E. Carlson, S. W. Hostetler, P. U. Clark, J. Cuzzone, G. A. Milne, K. Winsor, and M. Caffee, Final Laurentide ice-sheet deglaciation and Holocene climate-sea level change, *Quaternary Science Reviews*, *152*, 49–59, doi:10.1016/j.quascirev.2016.09.014, 2016.

[45] Walcott, R. I., Late Quaternary vertical movements in eastern North America: Quantitative evidence of glacio-isostatic rebound, *Reviews of Geophysics*, *10*, 849–884, doi:10.1029/RG010i004p00849, 1972.

[46] Walcott, R. I., Rheological models and observational data of glacio-isostatic rebound., *Earth rheology, isostasy and eustasy, proc. symp., Stockholm. 1977*, pp. 3–10, 1980.

[47] Wickert, A. D., Reconstruction of North American drainage basins and river discharge since the Last Glacial Maximum, *Earth Surface Dynamics*, *4*, 831–869, doi:10.5194/esurf-4-831-2016, 2016.

[48] Wickert, A. D., J. X. Mitrovica, C. Williams, and R. S. Anderson, Gradual demise of a thin southern Laurentide ice sheet recorded by Mississippi drainage, *Nature*, *502*, 668–672, doi:10.1038/nature12609, 2013.

[49] Wieczerkowski, K., J. X. Mitrovica, and D. Wolf, A revised relaxation-time spectrum for Fennoscandia, *Geophysical Journal International*, *139*, 69–86, doi:10.1046/j.1365-246X.1999.00924.x, 1999.

Chapter 3

Modeling Northern Hemispheric ice sheet dynamics, sea level change and solid Earth deformation through the last glacial cycle

The previous chapter explored how ice cover changes influenced sea-level changes during the last deglaciation in North America. This chapter focusses in turn on how ice sheets have been influenced by sea-level changes in the past. I also consider a greater spatial and temporal scale than in the previous chapter - over the whole Northern Hemisphere through the last glacial cycle. In particular, I couple a sea level model to a dynamic ice sheet model to investigate the separate roles of solid Earth deformation and gravitational perturbation associated with ice sheet changes on the evolution of ice sheets and their sensitivity to climate. In the main text, I highlight the physics and implications of the feedbacks that arise between solid Earth, sea level and ice systems, and in the supplementary information I show that our conclusions in the main text hold for a wide range of Earth and ice model parameter settings.

3.1 Abstract

Retreat or advance of an ice sheet perturbs the Earth's solid surface, rotational vector and the gravitational field, which in turn feeds back onto the evolution of the ice sheet over a range of timescales. Throughout the last glacial cycle, ice sheets over the Northern Hemisphere have gone through multiple growth and retreat phases, but the dynamics during these phases are not well understood. In this study, we apply a coupled ice sheet-glacial isostatic adjustment model to simulate the Northern Hemisphere Ice Sheets over the last glacial cycle. We focus on understanding the influence of solid Earth deformation and gravitational field perturbations associated with surface (ice and water) loading changes on the dynamics of terrestrial and marine-based ice sheets during different phases of the glacial cycle. Our results show that solid Earth deformation enhances glaciation during growth phases and melting during retreat phases in terrestrial regions through ice-elevation feedback, and gravitational field perturbations have a stabilizing influence on marine-based ice sheets in regions such as Hudson Bay in North America and the Barents and Kara Seas in Eurasia during retreat phases through sea-level feedback. Our results also indicate that solid Earth deformation influences the relative sensitivity of the North American and Eurasian Ice Sheets to climate and thus the timing and magnitude of their fluctuations throughout the last glacial cycle.

3.2 Introduction

During the last glacial cycle, ice sheets in the Northern Hemisphere (Northern Hemispheric Ice Sheets, henceforth NHIS) went through multiple phases of growth and retreat during the buildup phase (∼120-21 ka; e.g., Dyke, 2004; Hughes et al., 2016; Kleman et al., 2010; Svendsen et al., 2004) until global ice volume and extent reached a maximum and global mean sea level was ∼130 m lower than at present day at the Last Glacial Maximum (∼26.5-21 ka; LGM; Austermann et al., 2013; Clark et al., 2009; Denton and Hughes, 1981). At the LGM, the British-Irish, Fennoscandian and Barents-Kara Ice Sheets covered Eurasia (Eurasian Ice Sheet Complex, henceforth EISC; Hughes et al., 2016), the Laurentide, Cordilleran and Innuitian Ice Sheets covered North America (North American Ice Sheet Complex, henceforth NAISC; Dyke, 2004), and the Greenland Ice Sheet (GIS) grew beyond its modern extent (Fleming and Lambeck, 2004). After the LGM, the EISC and NAISC retreated throughout the last deglaciation, ending in the final retreat of the Fennoscandian Ice Sheet by ∼9 ka (e.g., Cuzzone et al., 2016; Hughes et al., 2016) and the Laurentide Ice Sheet by ∼7 ka (Ullman et al., 2016). The last deglaciation phase ended with subsequent slowing of melting from the Antarctic and Greenland Ice Sheets by ∼4 ka (Yokoyama et al., 2019).

Understanding glacial-cycle dynamics of the NHIS is challenging since the ice sheet evolution is coupled to other components of the Earth system, and direct records of the long-term ice sheet evolution are limited because they are eroded away over multiple growth and retreat phases (Dyke et al., 2002; Kleman et al., 2010). A broad spectrum of modeling work has been done to explore the dynamics of the NHIS throughout the last glacial cycle, even when focusing only on the literature that studies the Northern Hemisphere as a whole (e.g., Abe-Ouchi et al., 2013; Banderas et al., 2018; Berends et al., 2018; Bonelli et al., 2009; Charbit et al., 2007; Ganopolski et al., 2010; Tarasov and Peltier 1997; Liakka et al., 2016;

Niu et al., 2019; Zweck and Huybrechts, 2005), during the pre-LGM buildup phase (Beghin et al., 2014; Charbit et al., 2013; Kleman et al., 2013; Stokes et al., 2012; Timmermann et al., 2010) and during the last deglaciation phase (Gregoire et al., 2015; Tarasov et al., 2012; Ullman et al., 2015). These studies have focused on different physical processes such as ice-atmosphere interactions (Beghin et al., 2014; Liakka et al., 2016), ice-ocean interactions (Timmermann et al., 2010), the role of orbital and greenhouse gas forcing on the evolution of the NHIS (Abe-Ouchi et al., 2013; Bonelli et al., 2009; Ganopolski et al., 2010; Gregoire et al., 2015), ice-sheet sensitivity to climate forcing (Banderas et al., 2018; Berends et al., 2018; Charbit et al., 2007; Tarasov and Peltier, 1997), ice-sheet sensitivity to climatological or glaciological model parameters (Charbit et al., 2013; Zweck and Huybrechts, 2005), and ice-sheet sensitivity to isostatic solid Earth deformation (Crucifix et al., 2001; van den Berg et al., 2008).

It has long been recognized that mass exchange between ice and water on the solid surface perturbs the gravitational field and rotation vectors and deforms the solid Earth. These responses together - termed “Glacial Isostatic Adjustment” (GIA) - lead to spatially and temporally variable changes in the elevations of the solid surface and the sea surface (e.g., Farrell and Clark, 1976; Mitrovica and Milne, 2002). The effects of GIA in turn feed back onto the dynamics and mass balance of ice sheets. In the interior of an ice sheet, viscoelastic deformation of the solid Earth underneath the ice alters the ice-surface elevation, changing atmospheric conditions (i.e., temperature and precipitation) and feeding back onto the surface mass balance of the ice sheet (termed the “ice-elevation feedback”; e.g., Levermann and Winkelmann, 2016). For example, when an ice sheet melts and the ice surface-elevation is lowered, increases in air temperature (lapse rate-induced) and precipitation (due to warmer air) lead to increased surface melting and accumulation, feeding back either negatively or positively onto the ice sheet’s surface mass balance. On the edge of an ice sheet, solid Earth depression and associated changes in ice surface slopes enhance ice flux into the ablation zone (Schoof, 2007; Weertman, 1974). If an ice sheet is marine-based and terminates in water, changes in local water depth due to changes in the solid Earth surface and gravitational equipotential surface feed back onto ice mass flux across the grounding line (the so-called "sea-level feedback"; e.g., Gomez et al., 2010). When a marine-based ice sheet loses mass, the solid Earth uplifts and the sea surface height drops near the retreating ice sheet because of the weakened gravitational attraction between ice and ocean (henceforth "ice-ocean gravity"), leading to a local sea level fall that acts to stabilize the ice sheet (Gomez et al., 2010).

Despite this existing knowledge of feedbacks between ice sheet dynamics, sea level change and solid Earth deformation, it is only recently that modeling studies have developed fully coupled, dynamic ice sheet-GIA models. Coupled models have been applied to simulate the evolution of the past and future Antarctic Ice Sheet (Gomez et al., 2013; 2015; 2018; Konrad et al., 2015) and past global ice sheets (de Boer et al., 2014), but are not yet applied extensively to the Northern Hemisphere. Unlike the Antarctic Ice Sheet where temperatures are colder, surface melting is minimal and ice mass loss happens dominantly through dynamic flow of ice across the grounding line (e.g., Shepherd et al., 2018), the dynamics of the NHIS are strongly sensitive to atmospheric forcing (e.g., Bonelli et al., 2009; Charbit et al., 2007; Niu et al., 2019) and hence the ice-elevation feedback would have played a significant role in NHIS evolution during the last glacial cycle. At the same time, the sea-level feedback would have influenced the dynamics of marine-based sectors of ice sheets in regions such as the Barents and Kara Seas in Europe and over Hudson Bay in North America.

While paleo ice sheet and sea level observations are extensive in the Northern Hemisphere, the processes driving observed changes remain often poorly understood. For example, the ice sheet mechanisms associated with meltwater pulse events (observed in relative sea level records; Fairbanks, 1989; Harrison et al., 2019) and Heinrich events (observed in ice-rafted debris records; Heinrich, 1988) are still debated. Furthermore, uncertainty remains in the individual contributions from the NAISC, EISC, and GIS to observed sea level changes (e.g., Bassis et al., 2017; MacAyeal, 1993). In addition, a number of recent studies (Batchelor et al., 2019; Carlson et al., 2018; Dalton et al., 2019; Pico et al., 2017) have proposed that the Laurentide Ice Sheet (LIS) was smaller than previously thought during the Marine Isotope Stage 3 (Lisiecki and Raymo, 2005) and rapidly grew to its LGM extent, but the processes driving this potential change remain relatively unexplored. In this regard, applying a coupled ice sheet-GIA model to the NHIS can both provide insight into the driving mechanisms of ice sheet change, and facilitate modeling glaciologically-consistent paleo-ice sheet evolution synchronously with associated gravitationally-consistent, spatially-variable sea level change, which can be directly compared to geomorphological data of ice-sheet change (e.g., terminal moraines, proglacial deposits or esker) and geophysical data of sea-level change (e.g., local relative sea-level records, GRACE data or present day GPS uplift rates).

In this study, we couple a dynamic ice sheet model to a global GIA model and apply the coupled model to simulate the NHIS over the last glacial cycle. Our central goal is to understand the influence of solid Earth deformation and spatially-variable gravitational field (and thus sea surface height) changes associated with surface (ice and ocean) loading redistribution on the evolution of the NHIS during growth and retreat phases throughout the last glacial cycle, which we term "deformational effects" and "gravitational effects", respectively. In the following sections, we introduce the ice sheet and GIA models and the coupling procedure (Section 2), show the results of NHIS ice volume changes over the last glacial cycle from simulations that include deformational and gravitational effects both separately and together, and explore how each effect plays a role in the distribution and timing of ice cover changes in North America and Eurasia during growth and retreat phases (Section 3). We finish with a discussion of our results in the context of existing literature (Section 4) followed by conclusions (Section 5).

3.3 Methods: Coupled ice sheet – glacial isostatic adjustment modeling

We couple a dynamic ice sheet model to a GIA model using the coupling algorithm described in Gomez et al. (2013) that has been previously applied to the past and future evolution of the Antarctic Ice Sheet. We review the key aspects of the modeling here, and more detailed descriptions of each model and the coupling procedure can be found in the following studies: Pollard and DeConto (2009; 2012) - ice sheet model, Gomez et al., (2013; 2015) - GIA model and coupling methods. The ice sheet model (Pollard and DeConto, 2012) combines Shallow Ice Approximation (SIA) and Shallow Shelf Approximation (SSA) dynamics. The ice flux across the grounding line is parameterized following Schoof (2007), which avoids the need for high resolution around the grounding zone and allows long-term and large-scale simulations to be feasible. The simplified dynamics capture grounding-line migration reasonably well in idealized intercomparisons (Pattyn et al., 2012, 2013), although with somewhat larger differences on smaller space and timescales (Drouet et al.,2013; Pattyn and Durand, 2013). The spatial resolution of the ice sheet model is 0.5-degree latitude and 1-degree longitude on a regular lat-lon grid, on which the domain of the model spans 35 N-90 N degrees in latitude and 0-360 degrees in longitude. The time resolution for the ice model is 0.5 year.

Climate forcing is obtained from a matrix of general circulation model (GCM) solutions for prescribed orbital configurations, atmospheric CO2 levels and ice-sheet sizes (DeConto and Pollard, 2003; Pollard, 2010; Pollard and DeConto, 2005). The GCM is the Global Environmental and Ecological Simulation of Interactive Systems (GENESIS) version 3 (Thompson and Pollard, 1997) and is run in spectral resolution of T31 (i.e., 48 latitude by 96 longitude cells). Each GCM solution contains an equilibrated climate condition for given prescriptions of the aforementioned variables. At any point during an ice sheet model simulation, monthly air temperature and precipitation are obtained by interpolating the values between the GCM-solution matrix. Monthly air temperature and precipitation are then interpolated in time to 5-day-time-step (which is the time-stepping of our surface mass balance model) annual cycle, after which the annual climate is bilinearly interpolated from the GCM grid to the ice model grid. In this procedure, a lapse rate correction from the topography assumed in the GCM matrix solutions to the modeled ice surface elevation is applied for both temperature and precipitation. While the appropriate lapse-rate value is uncertain, we use an atmospheric lapse rate of 8 C/km, which is larger than suggested in some studies (e.g., Abe-Ouchi et al., 2007) but within the range used in other previous studies (e.g., Marshall et al., 2002; Erokhina et al., 2017). In Supporting Information, we show equations for the lapse rate correction and the sensitivity of the NHIS volume to different parameter values used in the correction (Fig. 3.12). In calculating surface mass balance, we consider explicit snow and embedded liquid amount in pore space and allow refreezing and runoff of meltwater, where runoff only happens when snowpack is saturated with embedded liquid. Surface melt is computed by solving a linearized surface energy flux equation instead of using the Positive-Degree-Day scheme. We use a sub-grid scheme that straightforwardly interpolates the sloping ice surfaces within each cell and performs separate surface mass balance calculations for sub-grid portions of the cell before averaging them together, which reduces the dependency of the calculations to the model resolution. In the matrix climate forcing, GCM sensitivities are adjusted by multiplying the climate differences (temperature and precipitation) between pairs of matrix solutions by 2.5 due to orbital changes (the orbital forcing is shown in Fig. 3.7), and by 1.05 due to ice-sheet-extent changes. These ad-hoc adjustments represent uncertainty in the GCM climate sensitivities and are needed to achieve reasonably realistic orbital scale and 100-ky ice-sheet cycles in our current ice sheet model. We note that the focus of this study is on the sensitivity of ice sheet variations to ice-Earth-sea level feedbacks (rather than comparing our model results to data-based ice-sheet reconstructions), and the climate is adjusted simply to yield overall realistic cycles, i.e., with repeated growth and retreat phases on orbital time scales expanding towards a maximum similar to the Last Glacial Maximum, followed by a relatively rapid and complete or near-complete deglaciation similar to that since the LGM. In future work, we plan to improve the climate modeling.

For basal sliding, we use the Weertman sliding law with an exponent m=2 (Weertman, 1957). The basal sliding coefficient is set to be high (i.e., deformable sediment and faster ice flow) 10^{-6} m a^{-1} Pa^{-2} in regions in which the present-day topography is ocean-covered, and low (i.e., hard rock and slower ice flow) at 10^{-7} m a^{-1} Pa^{-2} in regions in which the present-day topography is above sea level. In Supporting Information, we perform additional simulations with more complex basal sliding coefficients based on the sediment distribution suggested by Gowan et al. (2019) and show that our conclusions remain the same.

The GIA model solves the general sea level theory described in Mitrovica and Milne (2003), Kendall et al. (2005), and Gomez et al. (2010). The model considers ice cover changes and a radially varying viscoelastic Earth structure as inputs and computes the responses of the solid Earth and gravitational field associated with changes in surface (ice and ocean) loading. We assume a spherically symmetric, self-gravitating viscoelastic Earth model (so-called "SGVE"; Peltier, 1974) that is rotating (Mitrovica et al., 2001), and adopt the elastic and density profile of the Earth structure from the seismic model PREM (Dziewonski and Anderson, 1981). Unless otherwise indicated, we adopt a lithospheric thickness of 120 km and upper and lower mantle viscosity of 5×10^{20} PaS and 5×10^{21} PaS, respectively. The GIA model performs simulations with a resolution of spherical harmonic degree and order 512, and the solutions account for the multi-normal response of the viscoelastic Earth to surface loading (Peltier, 1974). Since the dynamic ice sheet model simulates ice cover changes only over the Northern Hemisphere, we adopt the Antarctic Ice Sheet history from the ICE-6G_C model (Argus et al., 2014; Peltier et al., 2015) to produce global ice coverage as an input to the GIA model.

The coupling procedure is as described in Gomez et al. (2013). Initial conditions for coupled ice sheet-GIA model simulations are taken from a previous ice sheet model simulation that is spun up to reach an equilibrium initial state at the last interglacial (125 ka) where only the Greenland Ice Sheet exists in the Northern Hemisphere. Initial topography in the ice sheet model domain (35 N to 90 N latitude) is given by the ETOPO2 modern global topography dataset (National Geophysical Data Center, 2006). The initialized ice configuration and topography in the Northern Hemisphere are then passed to the GIA model, and merged with ICE-6G_C ice history and topography outside the ice sheet model domain (90 S to 35 N latitude). The initial topography for this domain (90 S to 35 N latitude) is computed from a standalone GIA-model simulation with ICE-6G_C over the last glacial cycle in which the predicted modern topography converges to the ETOPO2 topography.

At the start of a coupled simulation, the dynamic ice sheet model computes ice sheet change over the Northern Hemisphere every 0.5 years for the duration of a coupling interval (200 years) and passes the thickness of the ice sheets at the end of the coupling interval to the GIA model. The GIA model then merges ice cover predicted by the ice sheet model in the Northern Hemisphere and ICE-6G_C ice history in Antarctica and computes global variations in sea level due to ice loading changes across the current coupling interval. The resulting sea level change is passed back to update the bedrock elevation and sea level in the ice sheet model, and the ice sheet model runs forward for the next coupling interval. This process continues throughout the coupled simulation.

In order to consider the effects of solid Earth deformation and spatially-varying gravitational-field changes on the evolution of the NHIS throughout the last glacial cycle (i.e., deformational and gravitational effects), we perform four different coupled ice sheet-GIA model simulations in the main text: 1) a simulation on a viscoelastic, rotating Earth in which the GIA model accounts for spatially-varying gravitational field changes due to ice-ocean gravity (referred to as a “fully coupled” simulation), 2) a simulation on a viscoelastic rotating Earth in which ice-ocean gravity is not incorporated and the sea surface height shifts uniformly across the globe (referred to as a “deformable Earth-noIOG” simulation; as in Gomez et al., 2013), and 3) a simulation on a rigid, rotating Earth in which ice-ocean gravity is accounted for (referred to as a “rigid Earth-IOG” simulation). In Supporting Information, we review the modified sea level equation for these coupled simulations excluding ice-ocean gravity and solid Earth deformation. We note that we have varied our model setup by repeating these simulations at a range of ice sheet model resolutions adopting a range of model parameters (i.e., basal sliding coefficients, surface mass balance and Earth structure parameters) controlling the distribution of ice at the LGM and contribution of global mean sea level change during the deglaciation. Some of these results are shown in Supporting Information (Figs. 3.11-3.13).

3.3.1 Northern Hemisphere ice volume changes over the last glacial cycle

Figure 3.1 shows NHIS volume variations during the last glacial cycle in simulations performed with the coupled ice sheet-GIA model. In all of the simulations, the NHIS show multiple growth (marked in white bars in Fig. 3.1) and retreat (marked in light yellow bars in Fig. 3.1) phases across the glacial cycle, driven primarily by changes in solar insolation due to cyclical changes in Earth's orbit (i.e., Milankovitch cycles). The initial growth phase starts at ∼120 ka, reaching the first glacial peak at ∼110 ka. Other growth phases occur at 100-90 ka, 77-63 ka and a more gradual buildup into the LGM occurs from 52-20 ka. Retreat phases occur at 110-100 ka, 90-77 ka, 63-52 ka and 20-6 ka (the last deglaciation). We also provide snapshots of ice thickness at various times during the last glacial cycle in Fig. 3.8-3.10 to put our results into context with several published reconstructed ice histories (Peltier et al., 2004; Lambeck et al., 2014; Tarasov et al, 2012).

Figs. 3.2a and b show ice volume and the rate of change of volume, respectively, in North America, Eurasia and Greenland based on the fully coupled simulation (blue line in Fig. 3.1; Figs. 3.2c-d are based on the rigid-IOG simulation shown in the black line in Fig. 3.1). While the volume of the NAISC in our simulations is always greater than that of the EISC (Figs. 3.2a, c), the ice loss during retreat phases is not always dominated by the NAISC. The EISC is the dominant contributor to the global mean sea level changes during the first (110-100 ka) and the third (63-52 ka) retreat phases, while the NAISC is the dominant contributor during the second (90-77 ka) and the final (20-6 ka; the

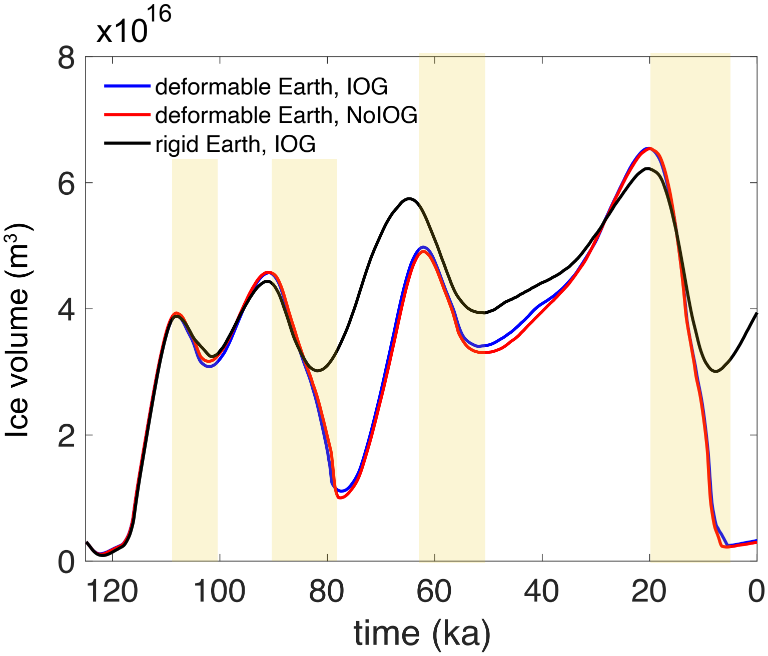

Figure 3.1: Changes in the Northern Hemisphere ice volume over the last glacial cycle. Time series of total Northern Hemisphere ice volume simulated with a coupled ice sheet-GIA model on a deformable Earth that captures the full multi-normal mode response (blue line), on a rigid Earth (black line), and for a simulation on a deformable Earth that neglects ice-ocean gravity (red line).

last deglaciation) retreat phases. Thus, our results suggest that the evolution of the NHIS over the last glacial cycle is complex and dynamic, and the EISC and the NAISC behave differently at each growth and retreat phase.

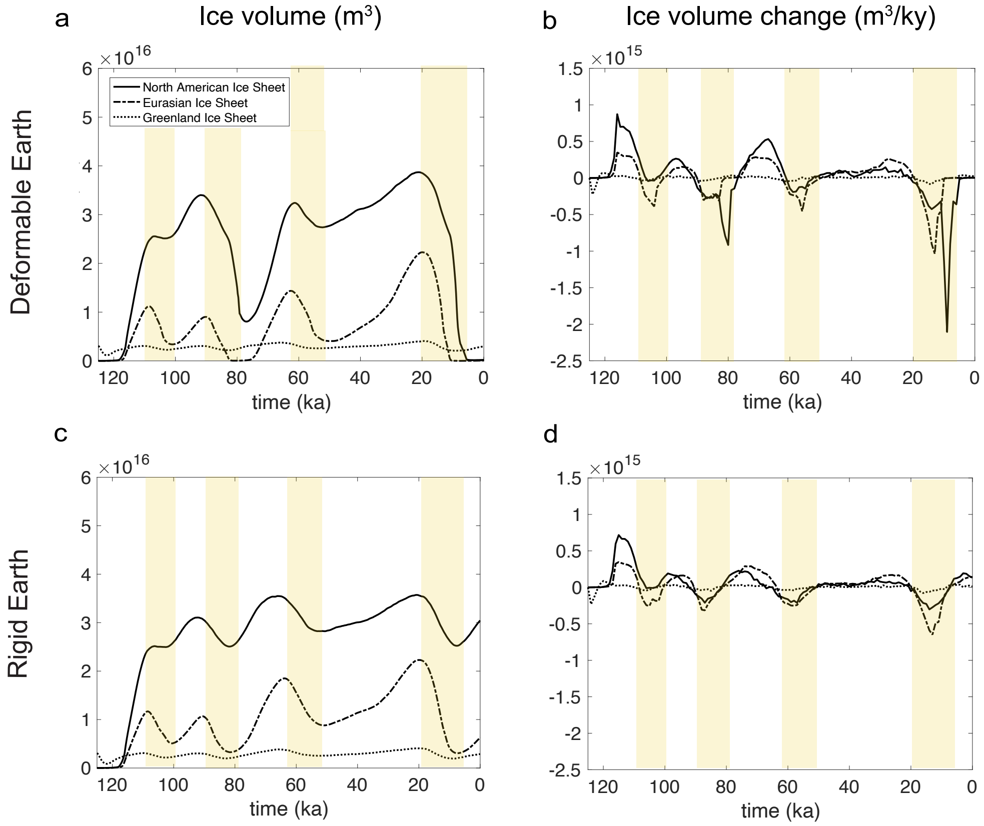

Figure 3.2: Changes in volume of individual ice sheets on the Northern Hemisphere over the last glacial cycle. (a) Time series of the volume of the North American Ice Sheet Complex (NAISC, solid line), Eurasian Ice Sheet Complex (EISC, dashed-dotted line) and the Greenland Ice Sheet (GIS, dotted line) based on the fully coupled simulation (i.e., blue solid line in Fig. 3.1). (b) Rate of change of volume of each ice sheet complex, in units of m^3/ky, calculated based on frame (a). (c, d) Equivalent to frames (a, b) but calculated from a simulation on a rigid Earth (rigid-IOG simulation, black line in Fig. 3.1).

3.3.2 Deformational effects during growth and retreat phases

In this section, we explore the impact of solid Earth deformation on NHIS evolution by comparing the fully coupled simulation (blue line in Fig. 3.1; Figs. 3.2a, b) to the rigid Earth-IOG simulation (black line in Fig. 3.1; Figs. 3.2c, d).

A comparison of the blue and red lines to the black line in Fig. 3.1 suggests that incorporating solid Earth deformation leads to larger variations in NHIS volume throughout the last glacial cycle. For example, from ∼77-63ka, the increase in the volume of the NHIS is ∼40 % greater for the deformable Earth case than for the rigid case, and the decrease in ice volume is ∼25 % greater during the last deglaciation. In particular, on a rigid Earth, the changes in volume of the NAISC are smaller in magnitude (Fig. 3.2c) and with less variable rates of change (Fig. 3.2d) compared to the deformable Earth case (Fig. 3.2a and b). The differences are most pronounced during the retreat phases between 90-77 ka and 20-6 ka (the last deglaciation). These results indicate that the modeled fluctuations in volume of the NAISC are more sensitive to solid Earth deformation than those of the EISC. The NAISC is larger and thicker than the EISC (e.g., see Fig. 3.3), leading to bedrock deformation that is both greater and more sensitive to deeper, higher viscous structure within the Earth's mantle. The solid Earth therefore takes longer to relax towards isostatic equilibrium following NAISC changes than following EISC changes, and the effects of the deformation on ice surface-elevation are enhanced. We also note that the two ice sheet complexes are underlain by different topographic features, which could also pre-dispose the NAISC to be more sensitive to solid earth deformation than the EISC.

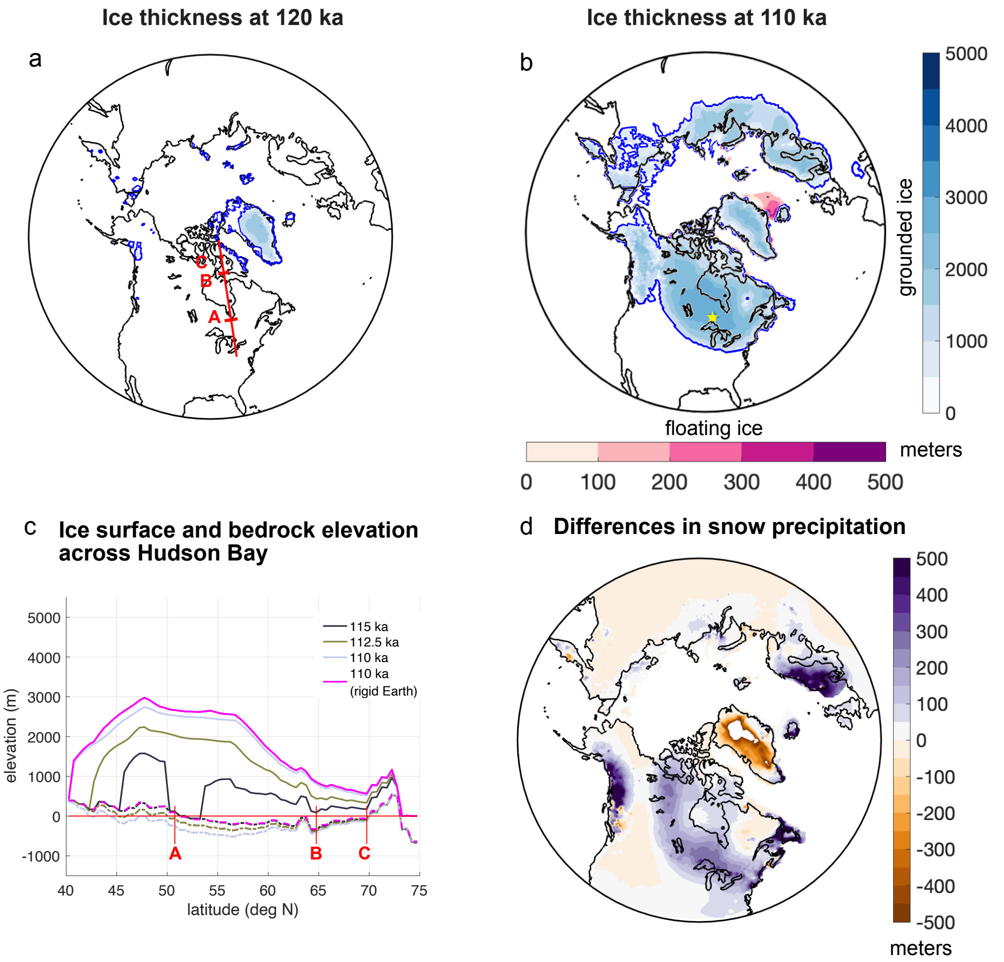

Figure 3.3: Initial buildup of ice sheet over the Northern Hemisphere between 120-110 ka. (a, b) Snapshot of the NHIS at (a) 120 ka and (b) 110 ka predicted in the fully coupled simulation. Grounded ice and floating ice are represented in blue and magenta, respectively. Blue contour lines show ice sheet grounding lines and black contour lines represent present-day coast lines. The yellow star in frame (b) shows the location where the NHIS reach a maximum thickness 110 ka. (c) Cross section of the elevation of the Laurentide Ice Sheet surface (solid lines) and the bedrock beneath the ice sheet (dashed lines) along Hudson Bay (red line in frame a) at the indicated times between 120 ka and 110 ka. Magenta lines correspond to the elevation of LIS surface (solid line) and bedrock (dashed line) at 110 ka simulated on the rigid Earth (red line in Fig. 3.1). (d) Difference (deformable minus rigid) in cumulative snowfall over continents, in meters, between the deformable and rigid Earth simulations from 120-100 ka.

Fig. 3.3 explores the impact of solid Earth deformation on changes in the distribution of ice over the Northern Hemisphere during the initial ice growth phase from 120-110 ka. During this phase, the Laurentide Ice Sheet (LIS) in North America advances to cover Hudson Bay (Fig. 3.3a to b) with a maximum thickness of ∼3080 m to the south of the bay (yellow star in Fig. 3.3b). The red line in Fig. 3.3a shows the location of the cross section displayed in Fig. 3.3c. Along this cross section, the LIS reaches a thickness of ∼2930 m to the south of James Bay at latitude ∼56-degrees North (Fig. 3.3c). The bedrock underneath the ice sheet subsides by up to 315 m from its initial elevation of 200 m below sea level and changes its slope as the ice sheet builds up, lowering the highest point of the ice surface on the cross section down to ∼2615 m at 110 ka (Fig. 3.3c). When the bedrock elevation is fixed in the rigid Earth-IOG simulation (dashed magenta line in Fig. 3.3c), the ice sheet along the cross section at the same location builds up to a smaller thickness of ∼2760 m by 110 ka. Since the bedrock elevation at this location remains at 200 m below sea level throughout the 10-ky period, the ice-surface elevation remains at ∼2960 m, which is ∼245 m higher than on deformable Earth (compare the solid magenta line to the lightest purple line in Fig. 3.3c). In the deformable Earth case, the ice surface remains lower in elevation and hence warmer in temperature with higher precipitation relative to the rigid Earth case, allowing the ice sheet to grow thicker (Fig. 3.3d). Note that both simulations begin from the same initial condition, and Fig. 3.3 focuses on the effect of solid Earth deformation during the first growth phase as bedrock elevation between the two simulations initially diverges. Later in the simulations, bedrock elevation differences, and hence deformational effects on ice cover, are larger (see Fig. 3.1).

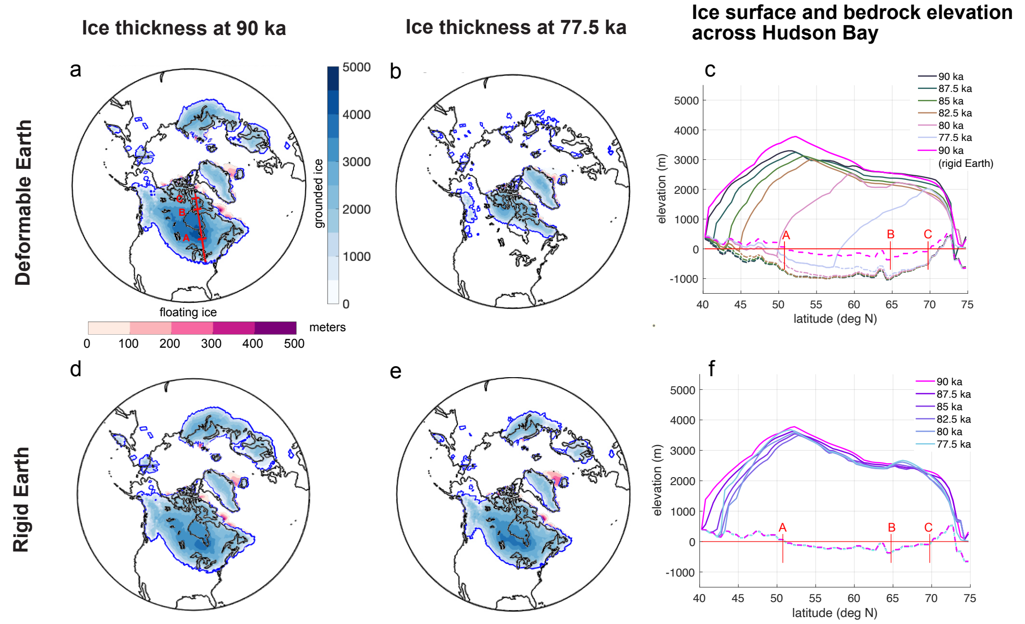

Figure 3.4: NHIS evolution during the 90-77 ka retreat phase. Snapshots of ice thickness at (a) 90 ka and (b) 77.5 ka. (c) Cross section of the surface elevation of the Laurentide Ice Sheet (solid lines) and bedrock elevation (dashed lines) along Hudson Bay (red line in frame a) at times between 90 ka and 77 ka modeled in the fully coupled simulation (solid blue line in Fig. 3.1a). Solid and dashed magenta lines represent the elevation of ice surface end bedrock at 90 ka, respectively, on a rigid Earth. Frames (d-f) are analogous to frames (a-c) but simulated on a rigid Earth.

Next, we explore the impact of solid Earth deformation on an ice cover retreat. Fig. 3.4 focuses on the retreat phase from ∼90-77 ka, during which differences between the rigid Earth and deformable Earth simulations are the largest (compare the black and blue lines in Fig. 3.1). Similar to the first growth phase shown in Fig. 3.3, the LIS builds up thicker on the deformable Earth than on the rigid Earth during the second growth phase from 100-90 ka. Across Hudson Bay by 90 ka on the deformable Earth, the LIS builds up to ∼680 m thicker than on the rigid Earth near latitude ∼63-degrees North. The highest points of ice-sheet surface are at near latitude ∼52-degrees North in both cases, but the ice-surface elevation is ∼535 m lower and ice thickness is 295 m greater on the deformable Earth than on the rigid Earth (compare the darkest blue and the magenta lines in Fig. 3.4c). This lower ice-surface elevation on a deformable Earth translates to ∼2.35-degree Celsius warmer surface air temperature relative to the rigid Earth case. Additionally, the slope of the bedrock at the edges of the ice sheet becomes more retrograde as the ice sheet advances on the deformable Earth. The resulting increase in surface ablation and the steeper bedrock slope in the deformable Earth case allows the edge of the ice sheet to retreat to Hudson Bay where the retreat accelerates (see the rapid grounding line retreat over the bay from 82.5-77.5 ka in Fig. 3.4c). This accelerated retreat is due to both the steeper bedrock slope on the edge of the ice sheet and a slippery marine bed allowing for faster flow over Hudson Bay (see Methods). Conversely, on the rigid Earth, the bedrock slope remains unchanged and not enough retreat occurs to reach the unstable region, and Hudson Bay remains ice covered in North America (see Figs. 3.4d-f).

Overall, Figs. 3.3 and 3.4 indicate that deformation of the solid Earth enhances thickening (thinning) of ice sheets during growth (retreat) phases in our model. During growth phases, our results show more snow precipitation over a large portion of the area in which ice sheets buildup on the deformable Earth compared to the rigid Earth case (Fig. 3.3d). Lowered ice-surface elevation and warmer air temperature due to solid Earth subsidence allows increased precipitation, which dominates over increased surface melting. During retreat phases, lowered ice surface and delayed uplift of the solid Earth keeps the ice surface lower in elevation, and surface melting dominates over increased precipitation. This positive feedback in both cases leads to greater-magnitude ice volume fluctuations on the deformable Earth than on the rigid Earth in our simulations (i.e., more ice buildup during growth phases between 77-63 ka and 52-20 ka and more ice loss during retreat phases between 90-77 ka and 20-6 ka, Fig. 3.1). In

Supporting Information, we show that our conclusions on the role of deformation on the NHIS evolution remain true in additional fully coupled simulations with varying surface mass balance parameters (Fig. 2.9).

3.3.3 Gravitational effects on marine-based ice sheets during retreat phases

The results above show that solid Earth deformation has a positive feedback on ice buildup and retreat over longer timescales ($\geq 10^3$ yr). Next, we focus on the negative feedback of gravitational field perturbations on the evolution of marine sectors of ice in North America and Eurasia on shorter timescales ($\leq 10^2$ yr). Fig. 3.5 illustrates the evolution of the LIS during its rapid retreat between 80-78.5 ka over Hudson Bay. Fig. 5a shows that until 80 ka, Hudson Bay is covered by the LIS both in the fully coupled simulation and the deformable Earth-noIOG simulation with similar extent (see the grounding lines in blue and red lines). By 79 ka (Fig. 3.5b), the LIS in both simulations undergo marine-based retreat over the bay (i.e., the bedrock elevation at the edge of the ice sheet is negative during the retreat, and hence the ice is marine-terminating). Then, between 79-78.5 ka, the ice sheet re-advances into the bay in the fully coupled simulation in which ice-ocean gravity is included. In contrast, the ice sheet continues to retreat when ice-ocean gravity is excluded (Fig. 3.5c). When ice-ocean gravity is incorporated, the sea surface height near the retreating ice sheet drops, increasing the sea level fall at the grounding line associated with ice loss. This stronger sea level fall when ice-ocean gravity is incorporated feeds back onto less ice flux across the grounding lines, eventually allowing the grounding lines to re-advance over Hudson Bay.

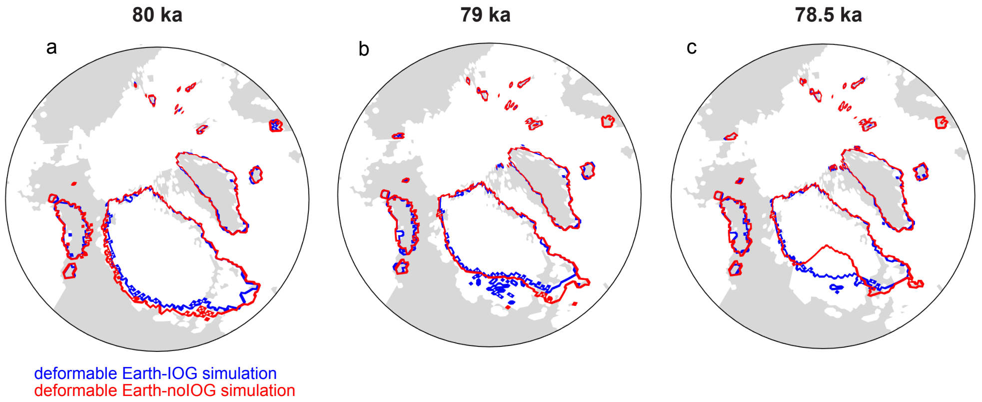

Figure 3.5: The effect of ice ocean gravity on the extent and timing of retreat over Hudson Bay towards the end of 90-80 ka deglacial phase. At (a) 80 ka, (b) 79 ka and (c) 78.5 ka. Blue and red lines represent the results from the coupled simulation on a deformable Earth in which ice-ocean gravity is incorporated (i.e., fully coupled simulation) and excluded (i.e., deformable Earth-noIOG coupled simulation), respectively. Positive bedrock topography at respective times is in gray.

The Barents-Kara Ice Sheet (BKIS) was a marine-based ice sheet that extended into the Barents and Kara Seas north of Siberia and Scandinavia at the LGM. Fig. 3.6 focuses on the impact of ice-ocean gravity on the extent and thickness of the BKIS during the last deglaciation by comparing the fully coupled and deformable Earth-noIOG simulations. In general, the largest differences occur in regions of ice-ocean interface where the ice is marine-terminating and the sea-level feedback on ice dynamics is active. Up until 13 ka, before major retreat in this region, the extent of the BKIS in the two simulations is similar, and differences in ice thickness along the grounding line are less than 100 m (Fig. 3.6a). Between 12.3-11.5 ka (Figs. 3.6b-d), the ice sheet retreat is delayed, and ice remains thicker in the fully coupled simulation, which includes ice-ocean gravity. For example, differences in ice thickness reach up to ∼1260 m in the Kara Sea at 11.8 ka (see the regions in dark yellow in Fig. 3.6c), and at the same time, the grounding line in the deformable Earth-noIOG simulation is up to ∼300 km further inland

(Fig. 3.6c). By 11 ka, the two simulations show the similar extent of grounding lines between the two simulations with and without ice-ocean gravity (there is some floating ice remaining in Barents Sea in the fully coupled simulation; see the yellow region outside of the grounding lines in Fig. 3.6e). The retreat of the BKIS is complete in both simulations by 10.5 ka (Fig. 3.6f). We note that the grounding line differences are relatively small for the NAISC, because not much of the NAISC margin was marine-retreating before 11 ka. Thus, Figs. 3.5 and 3.6 suggest that the sea-level feedback impacts the timing of marine-based ice sheet retreat during the last deglaciation in the Northern Hemisphere, leading to slowed retreat or re-advance of the ice margin, but does not play a big role in the evolution of ice sheet interiors.

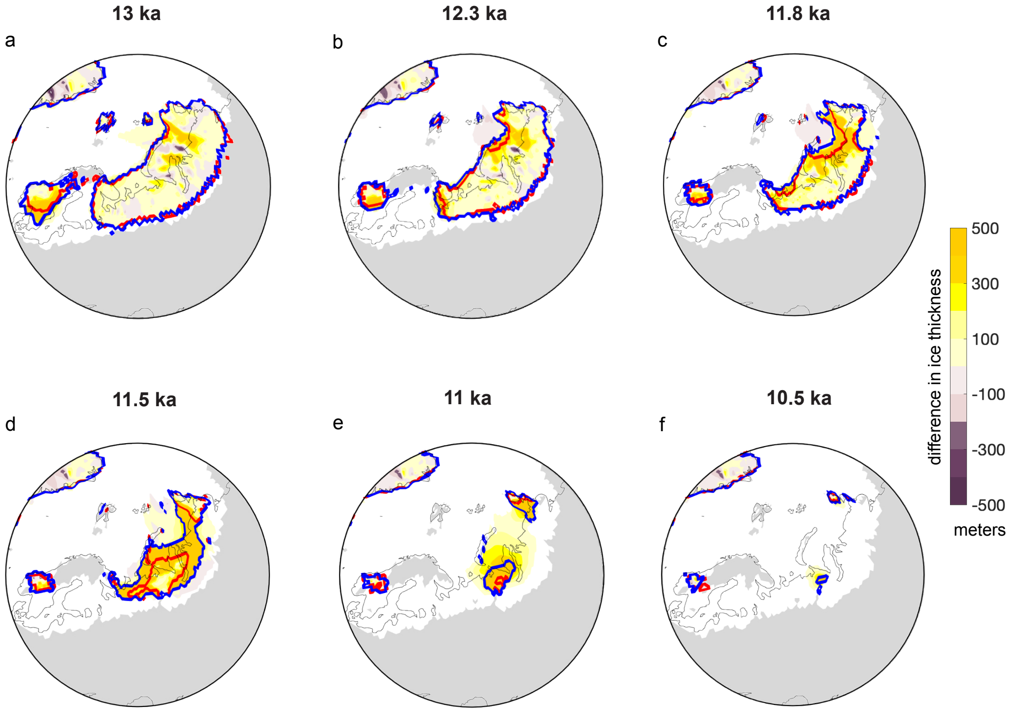

Figure 3.6: Stabilization of marine-terminating Barents-Kara Ice Sheets due to gravitational effects between 13-11ka during the last deglaciation. (a-f) Differences in ice thickness (in meters) modelled in the coupled simulation in which ice-ocean gravity is incorporated and not incorporated (i.e., fully coupled minus deformable Earth-noIOG) at (a) 13 ka, (b) 12.3 ka, (c) 11.8 ka and (d) 11.5 ka, (e) 11 ka and (f) 10.5 ka. Blue and red contour lines represent grounding lines of ice sheets in the fully coupled and deformable Earth-noIOG coupled simulations, respectively. Thin black contour lines represent present-day shorelines. Bedrock topography above sea level at respective times are in gray. Note that the color is saturated in frame (c) and (d).

3.4 Sensitivity of ice volume variations to adopted Earth and climate model parameters

Our results add to a body of literature showing that the modeled influence of Earth deformation on ice sheet evolution is sensitive to the parameters governing both the sensitivity of the ice sheet model the timing and magnitude of deformation in the Earth model and to climate. Previous studies have suggested the important role of solid Earth deformation in generating the ∼100-ky periodicity saw-tooth pattern of the Late Quaternary glacial cycles (e.g., Abe-Ouchi et al, 2013; Oerlemans, 1981) and debated the influence of solid Earth deformation during ice growth and retreat phases in the Northern Hemisphere (e.g., Crucifix et al. 2001; van den Berg et al. 2008). Incorporating a simple "Local Lithosphere Relaxing Asthenosphere" (LLRA; see Le Meur and Huybrechts, 1996) bedrock model in a 200 ky-long simulation, Crucifix et al. (2001) suggested that solid Earth deformation always acts to inhibit ice buildup during growth phases and to enhance ice loss during retreat phases. They also performed sensitivity tests varying bedrock density and relaxation time parameters and showed that their modeled ice volume changes are mainly controlled by the bedrock density parameter in the LLRA model. This parameter influences the equilibrium depression of the bedrock under loading (e.g., a smaller value of bedrock density results in a higher value of equilibrium depression). Their simulations showed that a smaller (higher) value of bedrock density leads to a smaller (higher) ice volume. Later, van den Berg et al. (2008) performed 1-D ice sheet model simulations using an Elastic Lithosphere and Relaxed Asthenosphere (ELRA; see Le Meur and Huybrechts, 1996) bedrock model that incorporates elastic flexure of the lithosphere as well as isostatic relaxation of the asthenosphere and a surface ice mass balance model that better captures the ice-elevation feedback at ice sheet margins. They showed that solid Earth deformation can feed back either positively or negatively on ice buildup depending on the choice of flexural rigidity, which controls the bending of the lithosphere in the bedrock model. They also performed 3-D ice sheet model simulations over Eurasia and showed that a lower value of the flexural rigidity (i.e., more bending of the lithosphere, resulting in more depression under loading and a higher peripheral bulge at the edge of the loading) results in a larger ice sheet.

Unlike the studies mentioned above, our results indicate that solid Earth deformation feeds back positively on ice volume changes, enhancing both ice sheet buildup and retreat (Figs. 3.1-3.4). In this study, we incorporate a self-gravitating, viscoelastic, spherical Earth model (SGVE) that takes a systematically different and more sophisticated approach to treating isostatic deformation. Previous studies have shown that the largest differences between ELRA and SGVE Earth models occur in the peripheral regions of an ice sheet (e.g., Le Meur and Huybrecht, 1996; van den Berg et al., 2008; Konrad et al., 2014), and the differences also depend on the size of the loading. To test sensitivity of the NHIS dynamics and the effects of solid Earth deformation on NHIS dynamics to varying Earth Structure and surface mass balance parameters, we show the results of additional coupled simulations adopting a range of Earth structure profiles (i.e., lithospheric thickness, upper and lower mantle viscosities) in the SGVE model (Fig. 3.11) and the surface mass balance parameters in the ice sheet model in Supporting Information (Figs. 3.12 and 3.13). Fig. 3.11 indicates that the NHIS volume is not very sensitive to any single parameter but is more sensitive to a combination of the parameters. Simulations with an Earth model that combines a thinner lithosphere and lower mantle viscosities produce larger variations in ice volume than those adopting a thicker lithosphere and higher mantle viscosities. We find that ice volume changes are even more sensitive to the choice of lapse rate and temperature correction (surface mass balance) parameters determining the climate forcing (Fig. 3.12). In particular, we find that both the modeled NHIS volume changes and the sensitivity of the ice volume to solid Earth deformation vary with these parameters (Fig. 3.13); the latter sensitivity increases with the adopted lapse rate. However, we highlight that our main conclusion on the role of deformational effects on NHIS dynamics still holds for the range of surface mass balance parameters and Earth model parameters we explored: Solid Earth deformation acts to enhance ice buildup during growth phases and enhance ice loss during retreat phases. In the context of existing literature, our results suggest that the role of solid Earth deformation on modeled ice sheets depends on both the adopted Earth model (e.g., LLRA, ELRA, or SGVE, with the latter being most realistic; Le Meur and Huybrecht, 1996) and their parameters, and on the surface mass balance model incorporated in the ice sheet model.

3.5 Discussion and Conclusions

In this study, we coupled a dynamic ice sheet model to a GIA model and applied the coupled model to the Northern Hemisphere over the last glacial cycle. We simulated glaciologically-consistent ice sheet dynamics, gravitationally self-consistent sea level change and solid Earth deformation, and explored the feedbacks that arise between these systems. Our results demonstrate that solid Earth deformation enhances buildup during growth phases and melting during retreat phases, leading to more dynamic ice cover changes throughout the last glacial cycle (Figs. 3.1-3.4). Gravitational effects have a stabilizing influence on marine-sectors of ice sheets in both North America and Eurasia during more rapid $O(\leq 10^2 \text{ yr})$ retreat phases (Figs. 3.5-3.6).

Our results suggest that the dynamics and sensitivity to climate of each ice sheet complex in the Northern Hemisphere differed due to deformational effects (Figs. 3.1 and 3.2). In particular, we find that solid Earth deformation enhances the sensitivity of the NAISC to climate more than the EISC (Fig. 3.2). These findings are in agreement with Bonelli et al. (2009), who simulated the NHIS over the last glacial cycle using a fully coupled climate-ice sheet model and showed that the Laurentide and Fennoscandian Ice Sheets have different responses to atmospheric CO2 concentration and insolation. Adding to their results, we find that the different responses of the EISC and the NAISC to climate may also be associated with differences in solid Earth deformation in response to different sizes of surface loading changes. The dependence of solid Earth deformation on the size of the load has been well explored in other studies (e.g., Crucifix et al., 2001; Le Meur and Huybrechts, 1996; Peltier, 1974; van den Berg et al., 2008).

In addition to being sensitive to the details of the bedrock and climate forcing models (See Figs. 3.11-3.13 and discussion in Section 4), our results comparing simulations that include and exclude solid Earth deformation suggest that the magnitude of ice volume variations is sensitive to the initial bedrock elevation at the start of every growth and retreat phase. Thus, ice volume changes during the earlier part of the last glacial cycle in our simulations may also depend on the initial bedrock elevation in the last interglacial. The solid Earth was not at isostatic equilibrium at the start of the last glacial cycle, since the glacial maximum of the penultimate glacial cycle (192-135 ka) was only established around 150-140 ka (Colleoni et al., 2016; Grant et al., 2014; Jakobsson et al., 2016; Rohling et al., 2014), and sea level records and modeling indicate ongoing GIA effects throughout the last interglacial (e.g., Clark et al., 2020; Dendy et al., 2017). This ongoing GIA could have influenced initial buildup of the NHIS at the start of the last glacial cycle. In subsequence work, we will apply the coupled model over multiple glacial cycles. The dependence of the rate and magnitude of ice cover changes on initial bedrock state may also provide insight into a possible setting for a rapid glaciation of the LIS from a small-sized configuration during the Marine Isotopoe Stage 3 to the LGM extent suggested by recent studies on the LIS configuration (e.g., Batchelor et al., 2019; Carlson et al., 2018; Dalton et al., 2019; Pico et al., 2017).

While deformational effects have a strong influence on ice volume variations over continental regions, gravitational effects due to ice-ocean gravity impact the timing and extent of ice sheet retreat regionally in marine terminating areas. For example, we found that the gravitationally driven draw-down of the sea surface due to local ice loss caused marine-ice sheet grounding lines to re-advance or to be delayed in retreat over Hudson Bay and Barents-Kara Seas near the end of retreat phases (Figs. 3.5 and 3.6). Existing work has applied coupled ice sheet-sea level modeling to show the stabilizing influence of gravitational effects on marine-sectors of the Antarctic Ice Sheet (Gomez et al., 2013, 2015; deBoer et al., 2014; Konrad et al., 2015). This study suggests that coupled models, which more precisely capture ice sheet-sea level feedbacks in marine areas than models that do not take into account ice-ocean gravity and complex solid Earth deformation, can potentially provide insight into the mechanisms driving marine-based ice sheet dynamics not only in Antarctica but also in Eurasia and North America. For example, these effects may play a role in the suggested rapid collapse of marine-sectors of the EISC that contributed to the Meltwater Pulse 1A event (Brendryen et al., 2020), in ice stream surging (Andreassen et al., 2014; Bjarnadóttir et al., 2014) and ice-rafted debris fluxes from the EISC during Heinrich Stadial 1 (e.g., Ng et al., 2018; Toucanne et al., 2015), and in the suggested Hudson Bay ice saddle collapse that might explain the 8.2 ka cold event (Gregoire et al., 2012; Lochte et al., 2019; Matero et al., 2017). Furthermore, studying the observed rapid collapse of paleo marine-terminating ice sheets such as the BKIS may in turn provide insight into the conditions, mechanisms, timing and extent of future collapse of marine sectors of the Antarctic Ice Sheet, which are a significant source of uncertainty in future sea-level projections (Church et al., 2013).

3.6 Supplementary material

3.6.1 Modified sea-level equation

As introduced in the main text (Methods), here we show modified sea-level equations adopted in the four coupled simulations that we performed to explore the role of solid Earth deformation and ice-ocean gravity on the NHIS dynamics: 1) fully-coupled simulation, 2) deformable Earth-noIOG simulation and 3) rigid Earth-IOG simulation.

The full sea-level theory is described in Kendall et al. (2005) and here we only show the part of the theory that we modify (note that these equations are written in form of a numerical algorithm). Global sea-level change as a response to surface (ice and ocean) loading redistribution, is calculated based on the viscoelastic Love number theory (Peltier, 1974). That is, the geographically varying component of globally defined sea level change is computed by convolving Greens functions for gravity and deformation with surface loading over space and time as expressed in Equation (B28) in Kendall et al. (2005):

$$
\begin{aligned}
[\Delta\, \mathcal{SL}_{lm}(t_j)]^{i-1,k} = {} & T_l\, E_l\, (\rho_i\, [\Delta I^*_{lm}(t_j)]^{k-1} + \rho_w\, [\Delta S_{lm}(t_{j-1})]^{i=\infty,k} + \rho_w\, [\delta S_{lm}(t_j)]^{i-1,k}\,) \\
& + T_l \sum_{n=0}^{j-1} \beta(l, t_n, t_j)\, (\, \rho_i\, [\delta I^*_{lm}(t_n)]^{k-1} + \rho_w\, [\delta S_{lm}(t_n)\,]^{i=\infty,k}\,) \\
& + \frac{1}{g}\, E_l^T\, ([\, \Delta\Lambda_{lm}(t_{j-1})\,]^{i=\infty,k} \,+\, [\delta\Lambda_{lm}(t_j)]^{i-1,k}) \\
& + \frac{1}{g} \sum_{n=0}^{j-1} \beta^T(l, t_n, t_j)\, [\, \delta\Lambda_{lm}(t_n)\,]^{i=\infty,k}\,,
\end{aligned}
\tag{3.1}
$$

where l and m are the spherical harmonic degree and order, respectively (thus, variables with a subscript lm are expanded in spherical harmonics), ρ_i and ρ_w are the density of ice and water, respectively, ΔI^* and ΔS represent the total change in land-based or grounded marine ice thickness (I^*) and ocean depth (S) from t_0 to t_j, δI^* and δS represent changes in land-based or grounded marine ice thickness and ocean depth over the time interval from t_{j-1} to t_j. $T_l = \frac{4\pi a^3}{M_e(2l+1)}$, M_e and a are the mass and radius of the Earth. The parameters E_l and β are determined by combining elastic and viscous components of surface load Love numbers k_l^E, h_l^E, r_k^l and $r_k^{\prime l}$ that describe the impulse response of a viscoelastic Earth to loading as a function of harmonic degree l. Similarly, E_l^T and β^T are described by combining elastic and viscous tidal Love numbers, respectively. The expressions for the four parameters are as follow,

$$E_l = 1 + k_l^E - h_l^E \tag{3.2}$$

$$\beta(l, t_n, t_j) = \sum_{k=1}^{K} \frac{r_k^{\prime l} - r_k^l}{s_k^l}[1 - e^{s_k^l(t_j - t_n)}] \tag{3.3}$$

$$E_l^T = 1 + k_l^{T,E} - h_l^{T,E} \tag{3.4}$$

$$\beta^T(l, t_n, t_j) = \sum_{k=1}^{K} \frac{r_k^{\prime l,T} - r_k^{l,T}}{s_k^l}[1 - e^{s_k^l(t_j - t_n)}] \tag{3.5}$$

Below describes the physical correspondence of each Love number used to form the above parameters:

h_l^E is an elastic surface load Love number corresponding to the instantaneous vertical displacement of the solid Earth.

k_l^E is an elastic surface load Love number corresponding to changes in the gravitational field associated with instantaneous, elastic vertical displacement of the solid Earth.

$r_k^{\prime l}$ is a viscous surface load Love number corresponding to changes in the gravitational field associated with viscous vertical displacement of the solid Earth.

r_k^l is a viscous surface Love number corresponding to the viscous vertical displacement of the solid Earth.

$h_l^{T,E}$ is an elastic tidal Love number corresponding to instantaneous vertical displacement of the solid Earth due to rotational vector perturbations caused by the total GIA forcing (i.e. load changes and viscoelastic response).

$k_l^{T,E}$ is an elastic tidal Love number corresponding to changes in the gravitational field due to instantaneous vertical displacement of the solid Earth driven by rotational vector perturbations.

$r_k^{\prime l,T}$ is a viscous tidal Love number corresponding to changes in the gravitational field due to viscous deformation of the solid Earth driven by rotational vector perturbations.

$r_k^{l,T}$ is a viscous tidal Love number corresponding to viscous vertical displacement of the solid Earth due to rotational vector perturbations.

To perform the coupled simulations in four different scenarios as described above (also in the method section of the main text), we modify Eqns. 3.2-3.5, and thus Eqn. 3.1.

Simulation 1. Coupled simulation on a deformable Earth with ice-ocean gravity (i.e. fully coupled simulation)

Eqn. 1 is not modified.

Simulation 2. Coupled simulation on a deformable Earth with no ice-ocean gravity (i.e. deformable Earth-noIOG simulation):

Love numbers associated with gravitational potential and the direct effect of the surface loading on the gravitational field (the term ‘1’ in Eqn. 3.2 and 3.4) are set to zero, that is,

$$r_k^{\prime l} = r_k^{\prime l,T} = k_l^E = k_l^{T,E} = 0.$$

Simulation 3. Coupled simulation on a rigid Earth with ice-ocean gravity (i.e. rigid Earth-IOG):

For a rigid Earth, Love numbers associated with deformation are set to zero, that is,

$$k_l^E = h_l^E = r_k^{\prime l} = r_k^l = r_k^l = k_l^{T,E} = h_l^{T,E} = r_k^{\prime l,T} = r_k^{l,T} = 0.$$

3.6.2 Orbital forcing for ice sheet-GIA model simulations

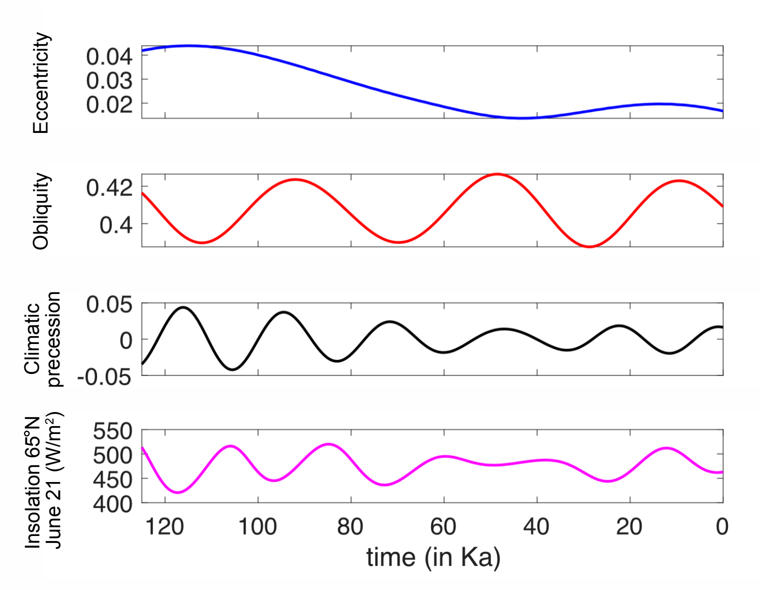

Figure 3.7: Milankovitch orbital forcing and mean daily insolation (65 °N) over the last 125 ky. (a) eccentricity, (b) obliquity, (c) climatic precession and (d) Summer (June 21st) insolation (W/m^2), based on Laskar et al. 2004.

3.6.3 Snapshots of ice sheets at different timings during the last glacial cycle

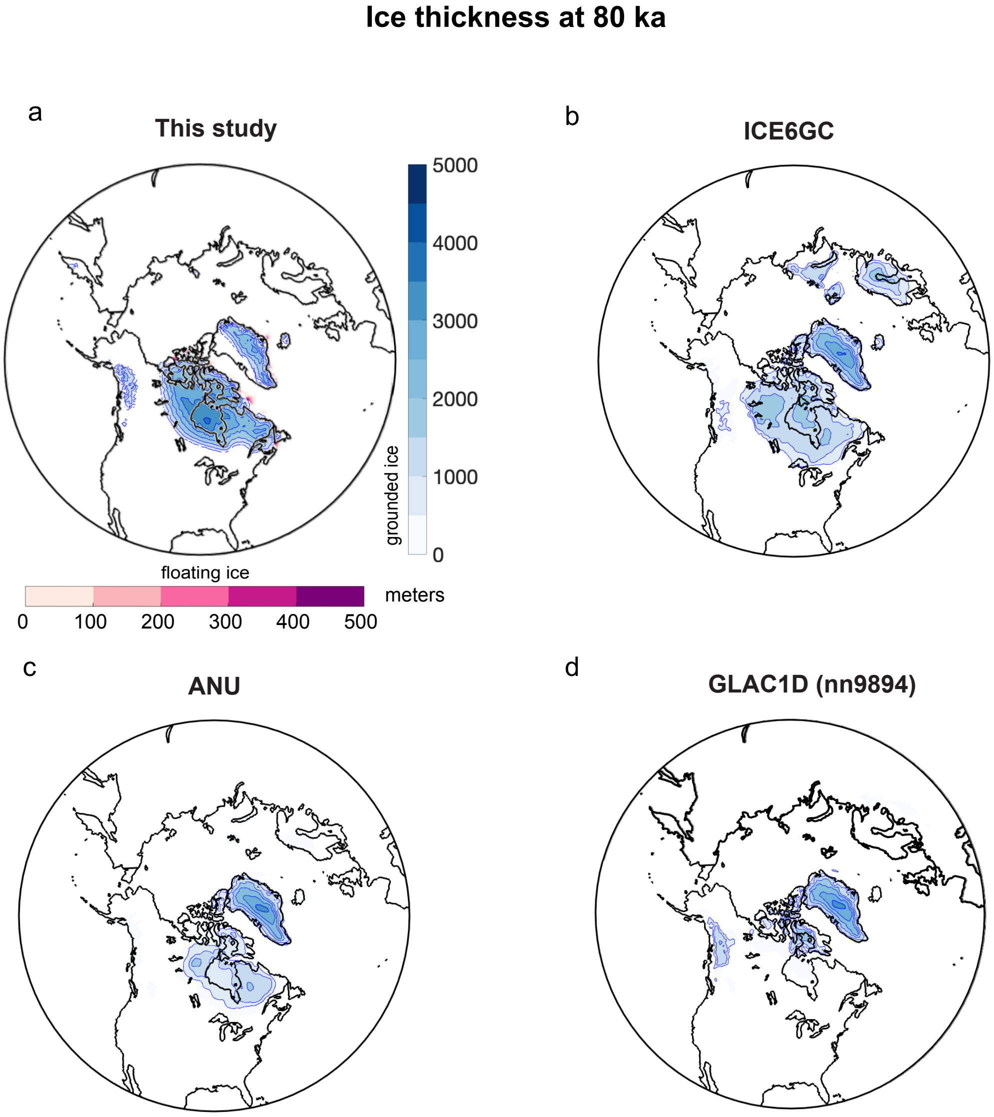

Figure 3.8: Snapshots of ice thickness at 80 ka from this study and other published ice history reconstructions. Ice thickness modeled from (a) the fully coupled simulation in this study, (b) ICE5G (Peltier et al., 2004), (c) ANU (Lambeck et al., 2014) and (d) GLAC1D-nn9984 (Tarasov et al, 2012). Note that GLAC1D is only provided over North America and Greenland, with no ice in Eurasia.

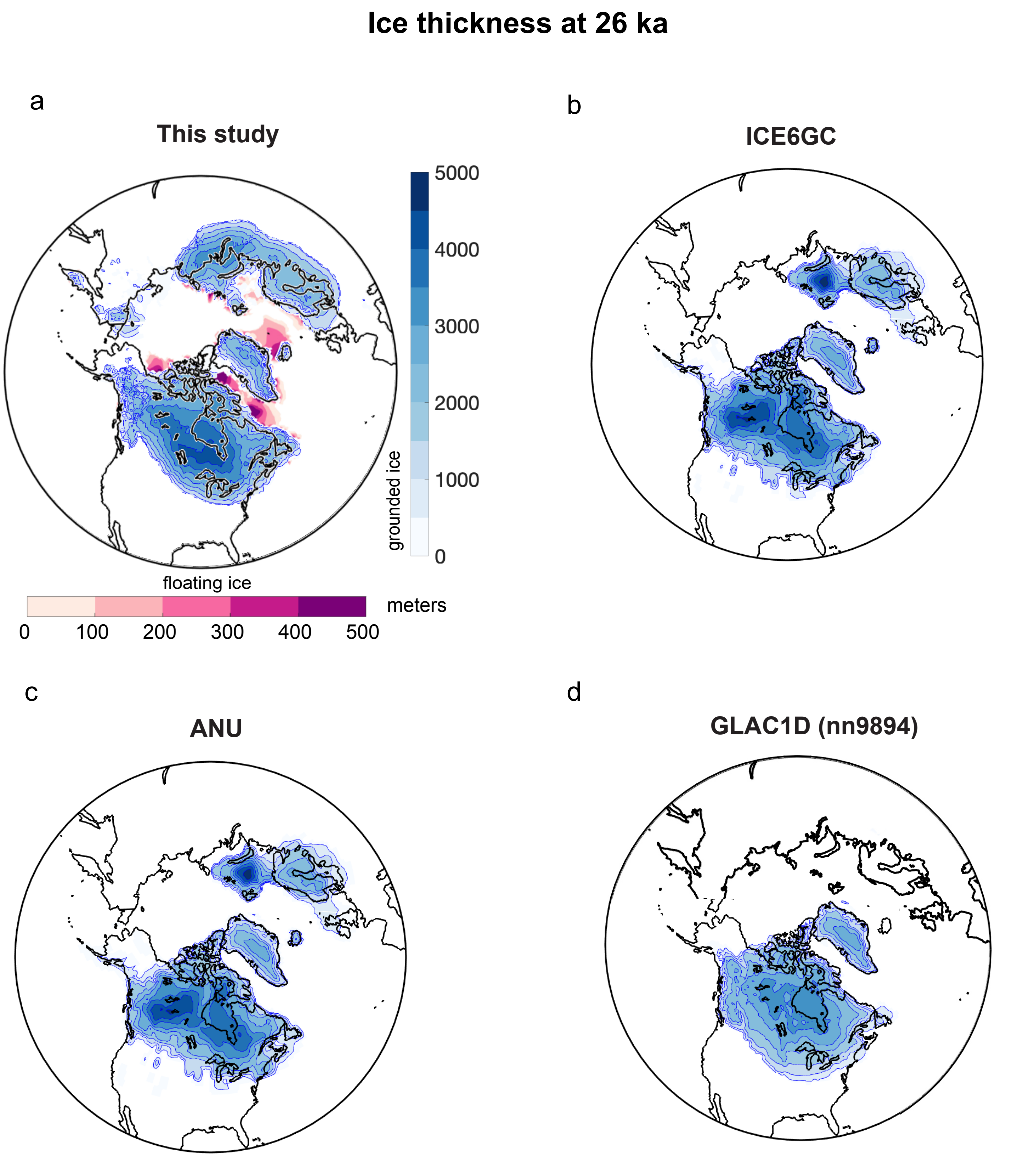

Figure 3.9: As in Fig. 3.8 but at 26 ka

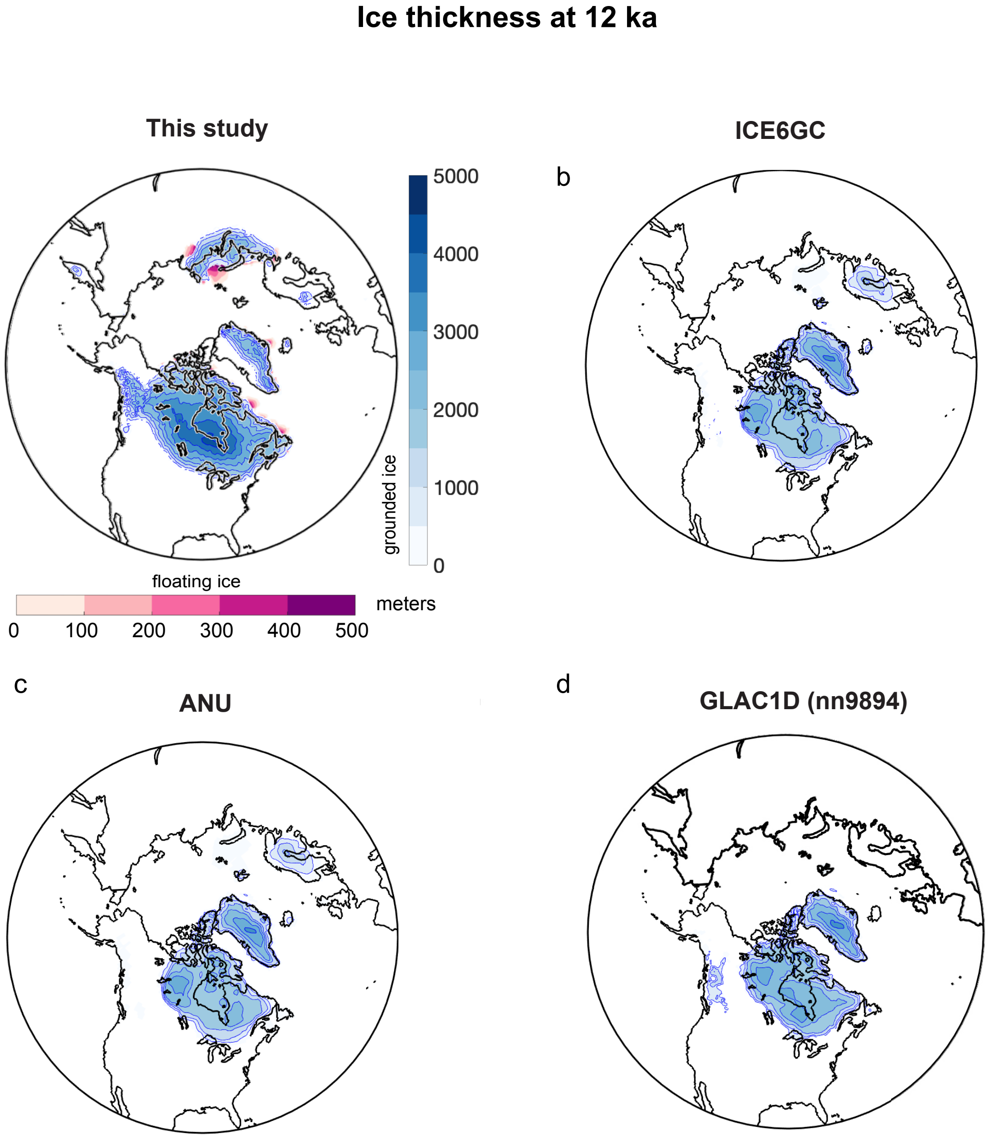

Figure 3.10: As in Fig. 3.8 but at 12 ka

In Fig. 3.8-3.10, we provide snapshots of the ice sheets over the Northern Hemisphere at different timings during the last glacial cycle from our simulation and ice sheet history reconstructions in the literature based on glacial isostatic adjustment modeling and relative sea level and ice sheet constraints. While there are differences in ice thickness and extent across all of the figure panels, the most noticeable differences between our results and other reconstructed ice sheets occur over the Siberian and Laurentide regions at LGM and during the last deglaciation (see Fig. 3.9 and 3.10). In our results, the ice extent in Siberia at 26 ka is overestimated towards inland (Fig. S2-2), and the Laurentide Ice Sheet remains largely glaciated until 12 ka, whereas data suggest the earlier onset of deglaciation over Laurentide region (Fig. 3.10). This could be due to limitations in the representation of the climate forcing in our model, an aspect that we will be focusing on improving in future work.

3.6.4 Sensitivity of the NHIS volume to the Earth Structure

To explore the sensitivity of results to the adopted Earth structure model, we performed additional simulations varying the lithospheric thickness from 120-245 km, upper mantle viscosity from 2-10$\times 10^{20}$ PaS and lower mantle viscosity from 5-30$\times 10^{21}$ PaS. Parameter ranges are chosen based on values that have been typically used in GIA simulations over North America (Lambeck et al., 2014; Lau et al., 2016; Mitrovica and Forte, 2004). Fig. 3.11 shows the predicted ice volume as a function of time in these additional simulations.

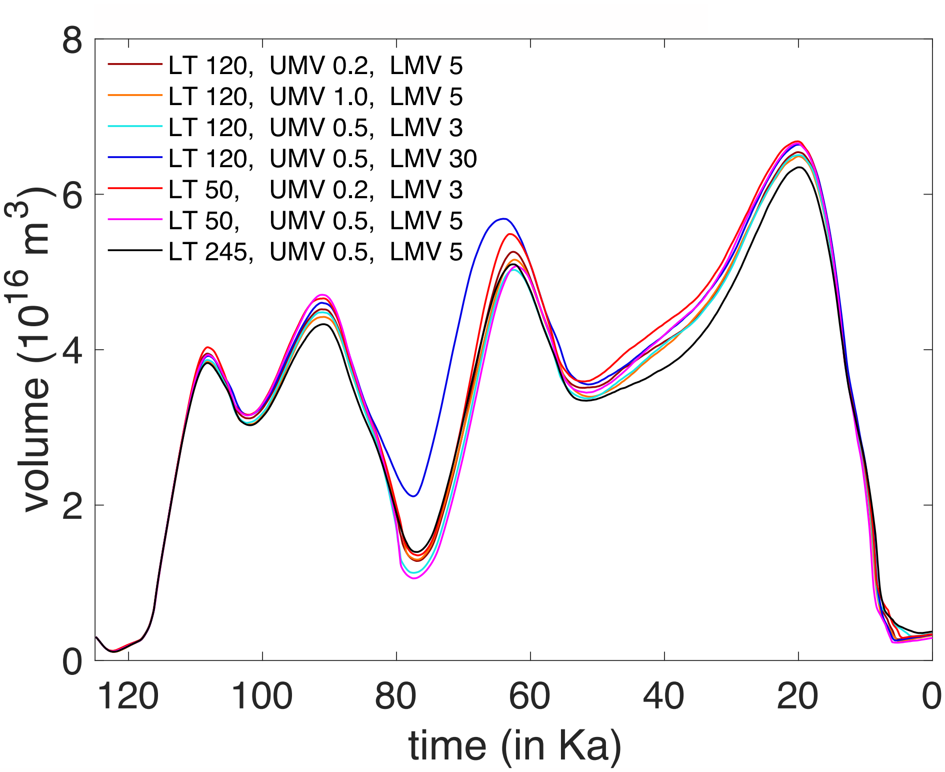

Figure 3.11: Sensitivity of Northern Hemispheric ice volume to the self-gravitating viscoelastic (SGVE) Earth model parameters over the last glacial cycle. Time series of Northern Hemisphere ice volume calculated in the fully coupled ice sheet-GIA model simulations in which solid Earth deformation and ice-ocean gravity are incorporated, with varying lithosphere thickness (LT), upper mantle viscosity (UMV) and lower mantle viscosity (LMV). Values of LT, in km, and UMV and LMV, in units of 10^{21} PaS, in each simulation are shown in the legend.

3.6.5 Sensitivity of the NHIS volume to surface mass balance parameters

To take into account the differences in ice surface elevation in the ice sheet model and the GCM climate data, we apply a lapse rate correction to temperature and precipitation based on Equations (34a and b) in Pollard and DeConto (2012).

The temperature correction is given by the following equation (Pollard and

DeConto, 2012; Eqn. 34a):

$$T_a^{'} = T_a - \gamma(h_s - h_s^{gcm}), \tag{3.6}$$

where $T_a^{'}$ and T_a are lapse-rate corrected- and uncorrected- annual surface air temperature on the ice model grid, respectively, γ is the lapse rate, h_s is the model ice surface elevation and $h_s^{gcm}$is the ice elevation in the GCM climate data.

The difference in air temperature is then taken into account in precipitation as follows (Pollard and DeConto, 2012; Eqn. 34b):

$$P^{'} = P \times 2^{(T_a^{'} - T_a)/\Delta T}, \tag{3.7}$$

Where $P^{'}$ and P are lapse-rate corrected- and uncorrected- annual precipitation on the ice model grid, respectively, and ΔT is a spatially uniform shift in air temperature used to scale the temperature correction $(T_a^{'} - T_a)$, or equivalently, $-\gamma(h_s - h_s^{gcm})$.

Thus, incorporating Eqn. 3.6 into 3.7 yields as follows:

$$P^{'} = P \times 2^{-\gamma(h_s - h_s^{gcm})/\Delta T}, \tag{3.8}$$

Notice that both the lapse rate (γ) and the temperature shift ΔT act as scales to the annual precipitation. The term $(h_s - h_s^{gcm})$ is usually a positive value and thus the greater ratio of the lapse rate γ to the temperature shift ΔT (i.e. $\gamma/\Delta T$) leads to a smaller value of precipitation $P^{'}$ applied to ice sheet in the ice model. The simulations in the main text adopt values $\gamma = 8$ °C/km and $\Delta T = 10$ °C, and we show the results of additional simulations in Fig. 3.12) in which we vary the values of the climate forcing parameters: γ between 5-10 °C/km and ΔT between 5-15 °C.

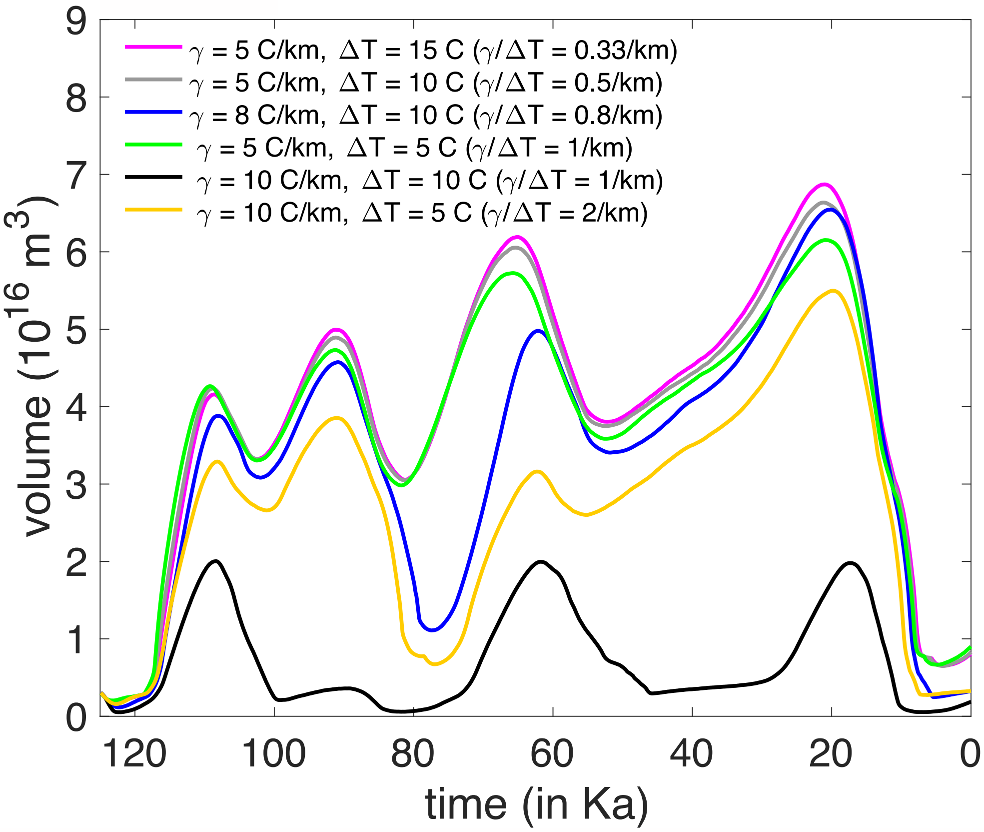

Figure 3.12: Changes in the Northern Hemispheric ice volume with varying surface mass balance parameters over the last glacial cycle. Time series of Northern Hemisphere ice volume calculated in the fully coupled simulation in which solid Earth deformation and ice-ocean gravity are accounted for. Values of γ (lapse rate) and ΔT (temperature shift) adopted in each simulation are indicated in the legend.

As suggested by the equations and text above, Fig. 3.12 shows that the NHIS volume over the last glacial cycle increases with the decreasing ratio of the lapse rate to the temperature shift, or with either the decreasing value of lapse rate at a fixed temperature shift, or the increasing value of temperature shift at fixed lapse rate.

Note that the green line (representing the profile $\gamma = 5$ °C/km and $\Delta T = 5$

°C) and the black line (γ = 10 °C/km and ΔT = 10 °C) in Fig. 3.12) have one-to-one ratio between the lapse rate and the temperature shift terms but the black line has a smaller magnitude of growth in ice volume. This is because the lapse rate (γ) also affects the annual temperature in addition to affecting the precipitation (Eqn. 3.1). The lapse-rate-corrected annual temperature $T_a^{'}$ in Eqn. 3.1 decreases with an increasing value of lapse rate, yielding a colder annual atmospheric temperature applied to the ice sheet model. Therefore, a colder (and thus the drier) atmosphere results in a smaller amount of precipitation. For a smaller value of lapse rate (e.g., 5 °C/km), the annual atmospheric temperature is warmer (and thus more moist but still cold enough to precipitate snow), yielding greater ice volume (see the magenta, grey and green lines in Fig. 3.12). Thus, a warmer atmosphere results in more precipitation, accumulating more ice during growth phases.

3.6.6 Sensitivity of the NHIS volume to solid Earth deformation in cases with different surface mass balance parameters

Next we consider the sensitivity of NHIS volume to solid Earth deformation in cases with different surface mass balance parameters. We choose four sets of parameters, $\gamma = 5$ °C/km and $\Delta T = 10$ °C; $\gamma = 10$ °C/km and $\Delta T = 10$ °C; $\gamma = 5$ °C/km and $\Delta T = 5$ °C; and $\gamma = 10$ °C/km and $\Delta T = 5$ °C from Fig. 3.12 and perform additional simulations on the rigid Earth as shown by the dashed-dotted lines in Fig. 3.13, and compare them to the fully coupled simulations.

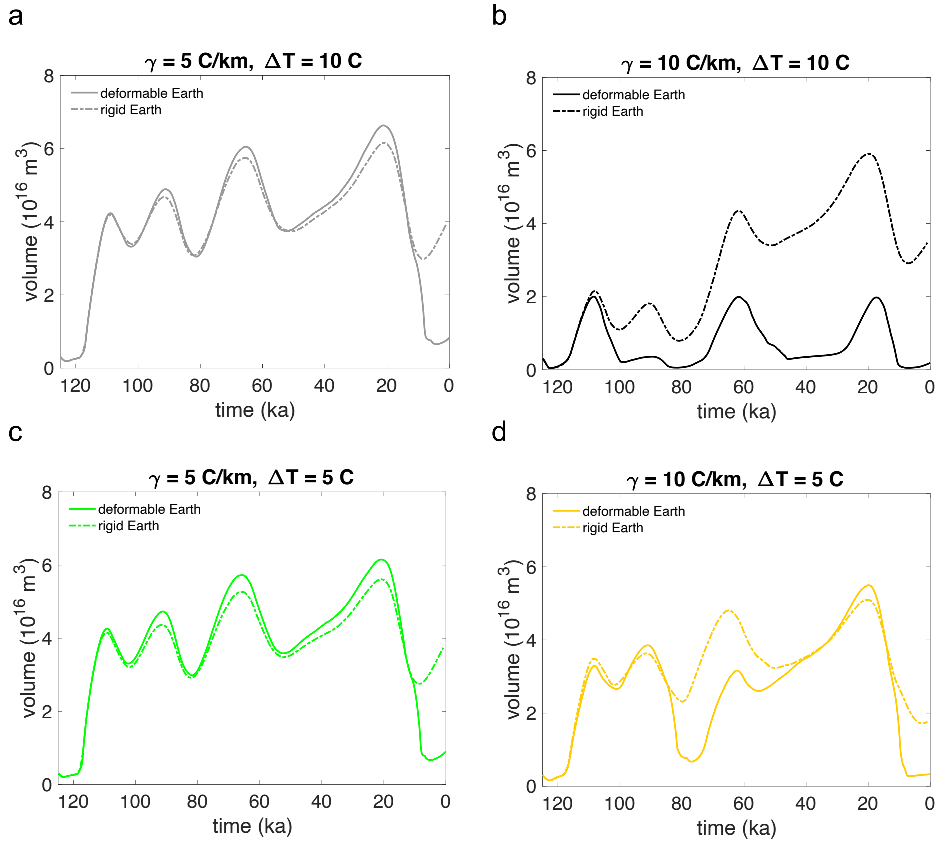

Figure 3.13: Changes in the Northern Hemisphere ice volume over the last glacial cycle on the deformable Earth (solid lines) and on the rigid Earth (dashed-dotted lines) with varying surface mass balance parameters. (a) $\gamma = 5$ °C/km and $\Delta T = 10$ °C (solid grey line is as in Fig. 3.12), (b) $\gamma = 10$ °C/km and $\Delta T = 10$ °C (solid black line is as in Fig. S4), (c) $\gamma = 5$ °C/km and $\Delta T = 5$ °C (solid green line is as in Fig. 3.12), (d) $\gamma = 10$ °C/km and $\Delta T = 5$ °C (solid yellow line as in Fig. 3.12).

Fig. 3.13 shows that the sensitivity of the NHIS volume to solid Earth deformation varies with the two surface mass balance parameters. Comparing the differences in ice volume between solid and dashed-dotted lines in panel (d) to those in the other three panels indicates that the differences (and thus the NHIS' sensitivity to deformation) increase with both the lapse rate and temperature shift. Comparing panel (a) to (b) and panel (c) to (d) shows that at a higher value of lapse rate (i.e. $\gamma = 10$ °C/km), the NHIS volume is higher on the rigid Earth than on the deformable Earth at every phase during the last glacial cycle regardless of the temperature shift. Comparing panels (a) to (c) and panels (b) to (d) indicates that a larger temperature shift yields greater differences in NHIS volume between the rigid and deformable Earths with fixed lapse rate. We note that while Fig. 3.13 shows the impact of varying SMB parameters on the integrated volume, the impact also varies spatially. For example, similar to what is suggested in the main text, the biggest differences between the rigid-Earth and deformable-Earth cases occur over North America, where the ice sheet is more sensitive to deformational effects than the EISC because of its bigger size.

Overall, Figs. 3.12 and 3.13 indicate that the role of solid Earth deformation on modeled NHIS dynamics during the last glacial cycle is sensitive to the applied surface mass balance parameters. However, deformational effects act as a positive feedback on both ice sheet growth and retreat in all cases.

3.6.7 Sensitivity of the NHIS volume to the spatial pattern of basal sliding coefficients

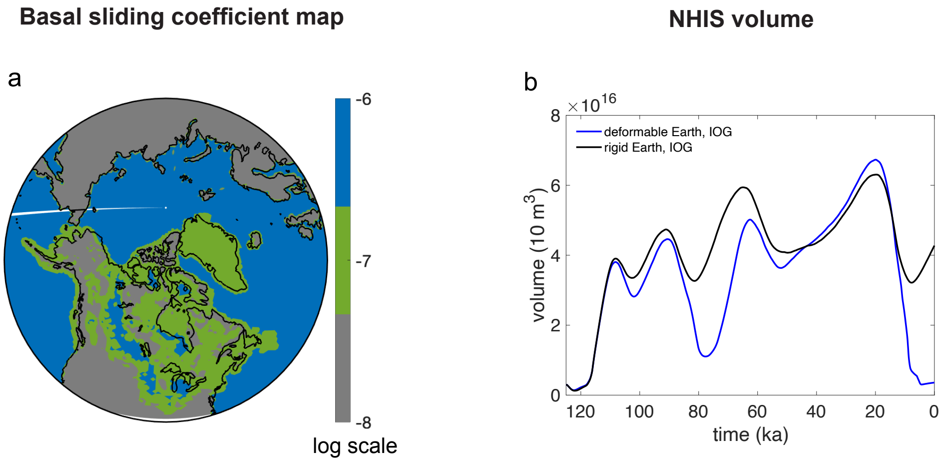

Figure 3.14: Map of basal sliding coefficients based on Gowan et al. (2019) and changes in the Northern Hemispheric ice volume over the last glacial cycle. (a) Spatially varying basal coefficients based on Gowan et al. (2019) incorporated in the sensitivity test simulations. Regions mapped in blue, green and grey have basal sliding coefficients of 10^{-6} m a^{-1} Pa^{-2}, 10^{-7} m a^{-1} Pa^{-2}, and 10^{-8} m a^{-1} Pa^{-2}, respectively. (b) NHIS volume predicted on the deformable Earth (blue line) and the rigid Earth (black line) incorporating the map of basal sliding coefficients shown in (a).

References

[1] Abe-Ouchi, A., T. Segawa, and F. Saito, Climatic conditions for modelling the Northern Hemisphere ice sheets throughout the ice age cycle, *Climate of the Past*, *3*, 423–438, doi:10.5194/cp-3-423-2007, 2007.

[2] Abe-Ouchi, A., F. Saito, K. Kawamura, M. E. Raymo, J. Okuno, K. Takahashi, and H. Blatter, Insolation-driven 100,000-year glacial cycles and hysteresis of ice-sheet volume, *Nature*, *500*, 190–193, doi:10.1038/nature12374, 2013.

[3] Andreassen, K., M. C. Winsborrow, L. R. Bjarnadóttir, and D. C. Rüther, Ice stream retreat dynamics inferred from an assemblage of landforms in the northern Barents Sea, *Quaternary Science Reviews*, *92*, 246–257, doi: 10.1016/j.quascirev.2013.09.015, 2014.

[4] Argus, D. F., W. R. Peltier, R. Drummond, and A. W. Moore, The Antarctica component of postglacial rebound model ICE-6G_C (VM5a) based on GPS positioning, exposure age dating of ice thicknesses, and relative sea level histories, *Geophysical Journal International*, *198*, 537–563, doi: 10.1093/gji/ggu140, 2014.

[5] Austermann, J., J. X. Mitrovica, K. Latychev, and G. A. Milne, Barbados-

based estimate of ice volume at Last Glacial Maximum affected by subducted plate, *Nature Geoscience*, *6*, 553–557, doi:10.1038/ngeo1859, 2013.

[6] Banderas, R., J. Alvarez-Solas, A. Robinson, and M. Montoya, A new approach for simulating the paleo-evolution of the Northern Hemisphere ice sheets, *Geoscientific Model Development*, *11*, 2299=2314, doi:10.5194/gmd-11-2299-2018, 2018.

[7] Bassis, J. N., S. V. Petersen, and L. Mac Cathles, Heinrich events triggered by ocean forcing and modulated by isostatic adjustment, *Nature*, *542*, 332–334, doi:10.1038/nature21069, 2017.

[8] Batchelor, C. L., M. Margold, M. Krapp, D. K. Murton, A. S. Dalton, P. L. Gibbard, C. R. Stokes, J. B. Murton, and A. Manica, The configuration of Northern Hemisphere ice sheets through the Quaternary, *Nature Communications*, *10*, 3713, doi:10.1038/s41467-019-11601-2, 2019.

[9] Beghin, P., S. Charbit, C. Dumas, M. Kageyama, D. M. Roche, and C. Ritz, Interdependence of the growth of the Northern Hemisphere ice sheets during the last glaciation: The role of atmospheric circulation, *Climate of the Past*, *10*, 345–358, doi:10.5194/cp-10-345-2014, 2014.

[10] Berends, C. J., B. De Boer, and R. S. Van De Wal, Application of HadCM3@Bristolv1.0 simulations of paleoclimate as forcing for an ice-sheet model, ANICE2.1: Set-up and benchmark experiments, *Geoscientific Model Development*, *11*, 4657–4675, doi:10.5194/gmd-11-4657-2018, 2018.

[11] Bjarnadóttir, L. R., M. C. Winsborrow, and K. Andreassen, Deglaciation of the central Barents Sea, *Quaternary Science Reviews*, *92*, 208–226, doi:10.1016/j.quascirev.2013.09.012, 2014.

[12] Bonelli, S., S. Charbit, M. Kageyama, M. N. Woillez, G. Ramstein, C. Dumas, and A. Quiquet, Investigating the evolution of major northern hemisphere ice sheets during the last glacial-interglacial cycle, *Climate of the Past*, *5*, 329–345, doi:10.5194/cp-5-329-2009, 2009.

[13] Brendryen, J., H. Haflidason, Y. Yokoyama, K. A. Haaga, and B. Hannisdal, Eurasian Ice Sheet collapse was a major source of Meltwater Pulse 1A 14,600 years ago, *Nature Geoscience*, *13*, 363–368, doi:10.1038/s41561-020-0567-4, 2020.

[14] Carlson, A. E., L. Tarasov, and T. Pico, Rapid Laurentide ice-sheet advance towards southern last glacial maximum limit during marine isotope stage 3, *Quaternary Science Reviews*, *196*, 118–123, doi:10.1016/j.quascirev.2018.07.039, 2018.

[15] Charbit, S., C. Ritz, G. Philippon, V. Peyaud, and M. Kageyama, Numerical reconstructions of the Northern Hemisphere ice sheets through the last glacial-interglacial cycle, *Climate of the Past*, *3*, 15–37, doi:10.5194/cp-3-15-2007, 2007.

[16] Charbit, S., C. Dumas, M. Kageyama, D. M. Roche, and C. Ritz, Influence of ablation-related processes in the build-up of simulated Northern Hemisphere ice sheets during the last glacial cycle, *The Cryosphere*, *7*, 681–698, doi:10.5194/tc-7-681-2013, 2013.

[17] Clark, P. U., A. S. Dyke, J. D. Shakun, A. E. Carlson, J. Clark, B. Wohlfarth, J. X. Mitrovica, S. W. Hostetler, and A. M. McCabe, The Last Glacial Maximum, *Science*, *325*, 710–714, doi:10.1126/science.1172873, 2009.

[18] Clark, P. U., F. He, N. R. Golledge, J. X. Mitrovica, A. Dutton, J. S. Hoffman, and S. Dendy, Oceanic forcing of penultimate deglacial and last inter-

glacial sea-level rise, *Nature*, *557*, 660–664, doi:10.1038/s41586-020-1931-7, 2020.

[19] Colleoni, F., C. Wekerle, J. O. Näslund, J. Brandefelt, and S. Masina, Constraint on the penultimate glacial maximum Northern Hemisphere ice topography (140 kyrs BP), *Quaternary Science Reviews*, *137*, 97–112, doi: 10.1016/j.quascirev.2016.01.024, 2016.

[20] Crucifix, M., M. F. Loutre, K. Lambeck, and A. Berger, Effect of isotatic rebound on modelled ice volume variations during the last 200 kyr, *Earth and Planetary Science Letters*, *184*, 623–633, doi:10.1016/S0012-821X(00) 00361-7, 2001.

[21] Cuzzone, J. K., et al., Final deglaciation of the Scandinavian Ice Sheet and implications for the Holocene global sea-level budget, *Earth and Planetary Science Letters*, *448*, 34–41, doi:10.1016/j.epsl.2016.05.019, 2016.

[22] Dalton, A. S., S. A. Finkelstein, S. L. Forman, P. J. Barnett, T. Pico, and J. X. Mitrovica, Was the Laurentide Ice Sheet significantly reduced during Marine Isotope Stage 3?, *Geology*, *47*, 111–114, doi:10.1130/G45335. 1, 2019.

[23] De Boer, B., P. Stocchi, and R. S. Van De Wal, A fully coupled 3-D ice-sheet-sea-level model: Algorithm and applications, *Geoscientific Model Development*, *7*, 2141–2156, doi:10.5194/gmd-7-2141-2014, 2014.

[24] DeConto, R. M., and D. Pollard, Rapid Cenozoic glaciation of Antarctica induced by declining atmospheric CO2, *Nature*, *421*(6920), 245–249, doi: 10.1038/nature01290, 2003.

[25] Dendy, S., J. Austermann, J. R. Creveling, and J. X. Mitrovica, Sensitivity of Last Interglacial sea-level high stands to ice sheet configuration during

Marine Isotope Stage 6, *Quaternary Science Reviews*, *171*, 234–244, doi:10.1016/j.quascirev.2017.06.013, 2017.

[26] Denton, G. H., and T. J. Hughes, *Last great ice sheets.*, 484 pp., Johan Wiley and Sons, New York, 1981.

[27] Drouet, A. S., D. Docquier, G. Durand, R. Hindmarsh, F. Pattyn, O. Gagliardini, and T. Zwinger, Grounding line transient response in marine ice sheet models, *The Cryosphere*, *7*, 395–406, doi:10.5194/tc-7-395-2013, 2013.

[28] Dyke, A. S., An outline of North American deglaciation with emphasis on central and northern Canada, in *Quarternary Glaciations - Extent and Chronology, Part II*, edited by Elsevier, in j. ehle ed., pp. 373–424, Amsterdam, doi:10.1016/S1571-0866(04)80209-4, 2004.

[29] Dyke, A. S., J. T. Andrews, P. U. Clark, J. H. England, G. H. Miller, J. Shaw, and J. J. Veillette, The Laurentide and Innuitian ice sheets during the Last Glacial Maximum, *Quaternary Science Reviews*, *21*, 9–31, doi:10.1016/S0277-3791(01)00095-6, 2002.

[30] Dziewonski, A. M., and D. L. Anderson, Preliminary reference Earth model, *Physics of the Earth and Planetary Interiors*, *25*, 297–356, doi:10.1016/0031-9201(81)90046-7, 1981.

[31] Erokhina, O., I. Rogozhina, M. Prange, P. Bakker, J. Bernales, A. Paul, and M. Schulz, Dependence of slope lapse rate over the Greenland ice sheet on background climate, *Journal of Glaciology*, *63*(239), 568–572, doi:10.1017/jog.2017.10, 2017.

[32] Fairbanks, R. G., A 17,000-year glacio-eustatic sea level record: Influence

of glacial melting rates on the Younger Dryas event and deep-ocean circulation, *Nature*, *342*, 637–642, doi:10.1038/342637a0, 1989.

[33] Farrell, W. E., and J. A. Clark, On Postglacial Sea Level, *Geophysical Journal of the Royal Astronomical Society*, *46*, 647–667, doi:10.1111/j.1365-246X.1976.tb01252.x, 1976.

[34] Fleming, K., and K. Lambeck, Constraints on the Greenland Ice Sheet since the Last Glacial Maximum from sea-level observations and glacial-rebound models, *Quaternary Science Reviews*, *23*, 1053–1077, doi:10.1016/j.quascirev.2003.11.001, 2004.

[35] Ganopolski, A., R. Calov, and M. Claussen, Simulation of the last glacial cycle with a coupled climate ice-sheet model of intermediate complexity, *Climate of the Past*, *6*, 229–224, doi:10.5194/cp-6-229-2010, 2010.

[36] Gomez, N., J. X. Mitrovica, P. Huybers, and P. U. Clark, Sea level as a stabilizing factor for marine-ice-sheet grounding lines, *Nature Geoscience*, *3*, 850–853, doi:10.1038/ngeo1012, 2010.

[37] Gomez, N., D. Pollard, and J. X. Mitrovica, A 3-D coupled ice sheet - sea level model applied to Antarctica through the last 40 ky, *Earth and Planetary Science Letters*, *384*, 88–99, doi:10.1016/j.epsl.2013.09.042, 2013.

[38] Gomez, N., D. Pollard, and D. Holland, Sea-level feedback lowers projections of future Antarctic Ice-Sheet mass loss, *Nature Communications*, *6*, 8798, doi:10.1038/ncomms9798, 2015.

[39] Gomez, N., K. Latychev, and D. Pollard, A coupled ice sheet-sea level model incorporating 3D earth structure: Variations in Antarctica during the Last Deglacial Retreat, *Journal of Climate*, *31*, 4041–4054, doi:10.1175/JCLI-D-17-0352.1, 2018.

[40] Gowan, E. J., L. Niu, G. Knorr, and G. Lohmann, Geology datasets in North America, Greenland and surrounding areas for use with ice sheet models, *Earth System Science Data*, *11*, 375–391, doi:10.5194/essd-11-375-2019, 2019.

[41] Grant, K. M., et al., Sea-level variability over five glacial cycles, *Nature Communications*, *5*, 5076, doi:10.1038/ncomms6076, 2014.

[42] Gregoire, L. J., A. J. Payne, and P. J. Valdes, Deglacial rapid sea level rises caused by ice-sheet saddle collapses, *Nature*, *487*, 219–222, doi:10.1038/nature11257, 2012.

[43] Gregoire, L. J., P. J. Valdes, and A. J. Payne, The relative contribution of orbital forcing and greenhouse gases to the North American deglaciation, *Geophysical Research Letters*, *42*, 9970–9979, doi:10.1002/2015GL066005, 2015.

[44] Harrison, S., D. E. Smith, and N. F. Glasser, Late Quaternary meltwater pulses and sea level change, *Journal of Quaternary Science*, *34*, 1–15, doi:10.1002/jqs.3070, 2019.

[45] Heinrich, H., Origin and consequences of cyclic ice rafting in the Northeast Atlantic Ocean during the past 130,000 years, *Quaternary Research*, *29*(2), 142–152, doi:10.1016/0033-5894(88)90057-9, 1988.

[46] Hughes, A. L., R. Gyllencreutz, Ø. S. Lohne, J. Mangerud, and J. I. Svendsen, The last Eurasian ice sheets - a chronological database and time-slice reconstruction, DATED-1, *Boreas*, *45*, 1–45, doi:10.1111/bor.12142, 2016.

[47] Jakobsson, M., et al., Evidence for an ice shelf covering the central Arctic Ocean during the penultimate glaciation, *Nature Communications*, *7*, 10,365, doi:10.1038/ncomms10365, 2016.

[48] Kendall, R. A., J. X. Mitrovica, and G. A. Milne, On post-glacial sea level - II. Numerical formulation and comparative results on spherically symmetric models, *Geophysical Journal International*, *161*(3), 679–706, doi:10.1111/j.1365-246X.2005.02553.x, 2005.

[49] Kleman, J., K. Jansson, H. De Angelis, A. P. Stroeven, C. Hättestrand, G. Alm, and N. Glasser, North American Ice Sheet build-up during the last glacial cycle, 115-21kyr, *Quaternary Science Reviews*, *29*, 2036–2051, doi:10.1016/j.quascirev.2010.04.021, 2010.

[50] Kleman, J., J. Fastook, K. Ebert, J. Nilsson, and R. Caballero, Pre-LGM northern hemisphere ice sheet topography, *Climate of the Past*, *9*, 2365–2378, doi:10.5194/cp-9-2365-2013, 2013.

[51] Konrad, H., M. Thoma, I. Sasgen, V. Klemann, K. Grosfeld, D. Barbi, and Z. Martinec, The deformational response of a viscoelastic solid Earth model coupled to a thermomechanical ice sheet model, *Surveys in Geophysics*, *35*, 1441–1458, doi:10.1007/s10712-013-9257-8, 2014.

[52] Konrad, H., I. Sasgen, D. Pollard, and V. Klemann, Potential of the solid-Earth response for limiting long-term West Antarctic Ice Sheet retreat in a warming climate, *Earth and Planetary Science Letters*, *432*, 254–264, doi:10.1016/j.epsl.2015.10.008, 2015.

[53] Lambeck, K., H. Rouby, A. Purcell, Y. Sun, and M. Sambridge, Sea level and global ice volumes from the Last Glacial Maximum to the Holocene, *Proceedings of the National Academy of Sciences of the United States of America*, *111*, 15,296–15,303, doi:10.1073/pnas.1411762111, 2014.

[54] Laskar, J., P. Robutel, F. Joutel, M. Gastineau, A. C. Correia, and B. Levrard, A long-term numerical solution for the insolation quantities of the

Earth, *Astronomy and Astrophysics*, *428*, 261–285, doi:10.1051/0004-6361:20041335, 2004.

[55] Lau, H. C., J. X. Mitrovica, J. Austermann, O. Crawford, D. Al-Attar, and K. Latychev, Inferences of mantle viscosity based on ice age data sets: Radial structure, *Journal of Geophysical Research: Solid Earth*, *121*, 6991–7012, doi:10.1002/2016JB013043, 2016.

[56] Le Meur, E., and P. Huybrechts, A comparisonon if different ways of dealing with isostasy: Examples from modelling the Antarctic ice sheet during the last grlacial cycle, *Annals of Glaciology*, *23*, 309–317, doi:10.1017/s0260305500013586, 1996.

[57] Levermann, A., and R. Winkelmann, A simple equation for the melt elevation feedback of ice sheets, *The Cryosphere*, *10*, 1799–1807, doi:10.5194/tc-10-1799-2016, 2016.

[58] Liakka, J., M. Löfverström, and F. Colleoni, The impact of the North American glacial topography on the evolution of the Eurasian ice sheet over the last glacial cycle, *Climate of the Past*, *12*, 1225–1241, doi:10.5194/cp-12-1225-2016, 2016.

[59] Lisiecki, L. E., and M. E. Raymo, A Pliocene-Pleistocene stack of 57 globally distributed benthic δ 18O records, *Paleoceanography*, *20*, PA1003, doi:10.1029/2004PA001071, 2005.

[60] Lochte, A. A., J. Repschläger, M. Kienast, D. Garbe-Schönberg, N. Andersen, C. Hamann, and R. Schneider, Labrador Sea freshening at 8.5 ka BP caused by Hudson Bay Ice Saddle collapse, *Nature Communications*, *10*, 586, doi:10.1038/s41467-019-08408-6, 2019.

[61] MacAyeal, D. R., Binge/purge oscillations of the Laurentide Ice Sheet as a cause of the North Atlantic's Heinrich events, *Paleoceanography*, *8*(6), 775–784, doi:10.1029/93PA02200, 1993.

[62] Marshall, S. J., T. S. James, and G. K. Clarke, North American Ice Sheet reconstructions at the last glacial maximum, *Quaternary Science Reviews*, *21*, 175–192, doi:10.1016/S0277-3791(01)00089-0, 2002.

[63] Matero, I. S., L. J. Gregoire, R. F. Ivanovic, J. C. Tindall, and A. M. Haywood, The 8.2 ka cooling event caused by Laurentide ice saddle collapse, *Earth and Planetary Science Letters*, *473*, 205–214, doi:10.1016/j.epsl.2017.06.011, 2017.

[64] Mitrovica, J. X., and A. M. Forte, A new inference of mantle viscosity based upon joint inversion of convection and glacial isostatic adjustment data, *Earth and Planetary Science Letters*, *225*(1–2), 177–189, doi:10.1016/j.epsl.2004.06.005, 2004.

[65] Mitrovica, J. X., and G. A. Milne, On the origin of late Holocene sea-level highstands within equatorial ocean basins, *Quaternary Science Reviews*, *21*, 2179–2190, doi:10.1016/S0277-3791(02)00080-X, 2002.

[66] Mitrovica, J. X., and G. A. Milne, On post-glacial sea level: I. General theory, *Geophysical Journal International*, *154*, 253–267, doi:10.1046/j.1365-246X.2003.01942.x, 2003.

[67] Mitrovica, J. X., G. A. Milne, and J. L. Davis, Glacial isostatic adjustment on a rotating earth, *Geophysical Journal International*, *147*, 562–578, doi:10.1046/j.1365-246x.2001.01550.x, 2001.

[68] National Geophysical Data Center, 2-minute Gridded Global Relief Data (ETOPO2) v2. NOAA, 2006.

[69] Ng, H. C., L. F. Robinson, J. F. McManus, K. J. Mohamed, A. W. Jacobel, R. F. Ivanovic, L. J. Gregoire, and T. Chen, Coherent deglacial changes in western Atlantic Ocean circulation, *Nature Communications*, *9*, 2947, doi:10.1038/s41467-018-05312-3, 2018.

[70] Niu, L., G. Lohmann, S. Hinck, E. J. Gowan, and U. Krebs-Kanzow, The sensitivity of Northern Hemisphere ice sheets to atmospheric forcing during the last glacial cycle using PMIP3 models, *Journal of Glaciology*, *65*(252), 645–661, doi:10.1017/jog.2019.42, 2019.

[71] Oerlemans, J., Some basic experiments with a vertically-integrated ice sheet model, *Tellus*, *33*(1), 1–11, doi:10.3402/tellusa.v33i1.10690, 1981.

[72] Pattyn, F., and G. Durand, Why marine ice sheet model predictions may diverge in estimating future sea level rise, *Geophysical Research Letters*, *40*, 4316–4320, doi:10.1002/grl.50824, 2013.

[73] Pattyn, F., et al., Results of the marine ice sheet model intercomparison project, MISMIP, *The Cryosphere*, *6*, 573–588, doi:10.5194/tc-6-573-2012, 2012.

[74] Pattyn, F., et al., Grounding-line migration in plan-view marine ice-sheet models: Results of the ice2sea MISMIP3d intercomparison, *Journal of Glaciology*, *59*, 410–422, doi:10.3189/2013JoG12J129, 2013.

[75] Peltier, W. R., The impulse response of a Maxwell Earth, *Reviews of Geophysics*, *12*(4), 649–669, doi:10.1029/RG012i004p00649, 1974.

[76] Peltier, W. R., Global glacial isostasy and the surface of the ice-age earth: The ICE-5G (VM2) model and GRACE, *Annual Review of Earth and Planetary Sciences*, *32*, 111–149, doi:10.1146/annurev.earth.32.082503.144359, 2004.

[77] Peltier, W. R., D. F. Argus, and R. Drummond, Space geodesy constrains ice age terminal deglaciation: The global ICE-6G_C (VM5a) model, *Journal of Geophysical Research: Solid Earth*, *120*, 450–487, doi:10.1002/2014JB011176, 2015.

[78] Pico, T., J. R. Creveling, and J. X. Mitrovica, Sea-level records from the U.S. mid-Atlantic constrain Laurentide Ice Sheet extent during Marine Isotope Stage 3, *Nature Communications*, *8*, 15,612, doi:10.1038/ncomms15612, 2017.

[79] Pollard, D., A retrospective look at coupled ice sheet-climate modeling, *Climatic Change*, *100*, 173–194, doi:10.1007/s10584-010-9830-9, 2010.

[80] Pollard, D., and R. M. DeConto, Hysteresis in Cenozoic Antarctic ice-sheet variations, *Global and Planetary Change*, *45*, 9–21, doi:10.1016/j.gloplacha.2004.09.011, 2005.

[81] Pollard, D., and R. M. DeConto, Modelling West Antarctic ice sheet growth and collapse through the past five million years, *Nature*, *458*, 329–332, doi:10.1038/nature07809, 2009.

[82] Pollard, D., and R. M. Deconto, Description of a hybrid ice sheet-shelf model, and application to Antarctica, *Geoscientific Model Development*, *5*, 1273–1295, doi:10.5194/gmd-5-1273-2012, 2012.

[83] Pollard, D., N. Gomez, and R. M. Deconto, Variations of the Antarctic Ice Sheet in a coupled ice sheet-Earth-sea level model: Sensitivity to viscoelastic Earth properties, *Journal of Geophysical Research: Earth Surface*, *122*, 2124–2138, doi:10.1002/2017JF004371, 2017.

[84] Rohling, E. J., G. L. Foster, K. M. Grant, G. Marino, A. P. Roberts, M. E. Tamisiea, and F. Williams, Sea-level and deep-sea-temperature

variability over the past 5.3 million years, *Nature*, *508*, 477–482, doi: 10.1038/nature13230, 2014.

[85] Schoof, C., Ice sheet grounding line dynamics: Steady states, stability, and hysteresis, *Journal of Geophysical Research: Earth Surface*, *112*, F03S28, doi:10.1029/2006JF000664, 2007.

[86] Shepherd, A., et al., Mass balance of the Antarctic Ice Sheet from 1992 to 2017, *Nature*, *558*, 219–222, doi:10.1038/s41586-018-0179-y, 2018.

[87] Stokes, C. R., L. Tarasov, and A. S. Dyke, Dynamics of the North American Ice Sheet Complex during its inception and build-up to the Last Glacial Maximum, *Quaternary Science Reviews*, *50*, 86–104, doi: 10.1016/j.quascirev.2012.07.009, 2012.

[88] Svendsen, J. I., et al., Late Quaternary ice sheet history of northern Eurasia, *Quaternary Science Reviews*, *23*, 1229–127, doi:10.1016/j.quascirev.2003.12.008, 2004.

[89] Tarasov, L., and W. R. Peltier, A high-resolution model of the 100 ka ice-age cycle, *Annals of Glaciology*, *25*, 58–65, doi:10.3189/s026030550001380x, 1997.

[90] Tarasov, L., A. S. Dyke, R. M. Neal, and W. R. Peltier, A data-calibrated distribution of deglacial chronologies for the North American ice complex from glaciological modeling, *Earth and Planetary Science Letters*, *315-316*, 30–40, doi:10.1016/j.epsl.2011.09.010, 2012.

[91] Thompson, S. L., and D. Pollard, Greenland and Antarctic mass balances for present and doubled atmospheric CO2 from the GENESIS version-2 global climate model, *Journal of Climate*, *10*, 871–900, doi: 10.1175/1520-0442(1997)010⟨0871:GAAMBF⟩2.0.CO;2, 1997.

[92] Timmermann, A., J. Knies, O. E. Timm, A. Abe-Ouchi, and T. Friedrich, Promotion of glacial ice sheet buildup 60-115 kyr B.P. by precessionally paced Northern Hemispheric meltwater pulses, *Paleoceanography*, *25*, PA4208, doi:10.1029/2010PA001933, 2010.

[93] Toucanne, S., G. Soulet, N. Freslon, R. Silva Jacinto, B. Dennielou, S. Zaragosi, F. Eynaud, J. F. Bourillet, and G. Bayon, Millennial-scale fluctuations of the European Ice Sheet at the end of the last glacial, and their potential impact on global climate, *Quaternary Science Reviews*, *123*, 113–133, doi:10.1016/j.quascirev.2015.06.010, 2015.

[94] Ullman, D. J., A. E. Carlson, F. S. Anslow, A. N. Legrande, and J. M. Licciardi, Laurentide ice-sheet instability during the last deglaciation, *Nature Geoscience*, *8*, 534–537, doi:10.1038/ngeo2463, 2015.

[95] Ullman, D. J., A. E. Carlson, S. W. Hostetler, P. U. Clark, J. Cuzzone, G. A. Milne, K. Winsor, and M. Caffee, Final Laurentide ice-sheet deglaciation and Holocene climate-sea level change, *Quaternary Science Reviews*, *152*, 49–59, doi:10.1016/j.quascirev.2016.09.014, 2016.

[96] van den Berg, J., R. S. van de Wal, G. A. Milne, and J. Oerlemans, Effect of isostasy on dynamical ice sheet modeling: A case study for Eurasia, *Journal of Geophysical Research: Solid Earth*, *113*, B05,412, doi:10.1029/2007JB004994, 2008.

[97] Weertman, J., Stability of the junction of an ice sheet and an ice shelf, *Journal of Glaciology*, *13*, 3–11, doi:10.3189/s0022143000023327, 1974.

[98] Yokoyama, Y., S. Hirabayashi, K. Goto, J. Okuno, A. D. Sproson, T. Haraguchi, N. Ratnayake, and Y. Miyairi, Holocene Indian Ocean sea

level, Antarctic melting history and past Tsunami deposits inferred using sea level reconstructions from the Sri Lankan, Southeastern Indian and Maldivian coasts, *Quaternary Science Reviews*, *206*, 150–161, doi: 10.1016/j.quascirev.2018.11.024, 2019.

[99] Zweck, C., and P. Huybrechts, Modeling of the northern hemisphere ice sheets during the last glacial cycle and glaciological sensitivity, *Journal of Geophysical Research Atmospheres*, *110*(D7), doi:10.1029/2004JD005489, 2005.

Chapter 4

Capturing the interactions between ice sheets, sea level and the solid Earth on a range of timescales: A new "time window" algorithm

The previous chapter investigated the roles of solid Earth deformation and gravitational field perturbations on the glacial-interglacial evolution of continental and marine based ice sheets. Results highlighted that the interactions between ice sheets, sea level and the solid Earth occur over a range of timescales. However, precisely capturing short-term interactions in coupled simulations becomes computationally infeasible as the length and/or temporal resolution of the simulations increase. In this chapter, I develop an algorithm for the sea-level module of a coupled ice sheet – sea level model that overcomes this computational challenge.

4.1 Abstract

Retreat and advance of ice sheets perturb the gravitational field, solid surface and rotation of the Earth, leading to spatially variable sea-level changes over a range of timescales $O(10^6$ yr), which in turn feed back onto ice sheet dynamics. Coupled ice-sheet – sea-level models have been developed to capture the interactive processes between ice sheets, sea level and the solid Earth, but it is computationally challenging to capture short-term interactions $O(\leq 10^2$ yr) precisely within longer $O(> 10^2$ yr) simulations. The classic coupling algorithm assigns a uniform temporal resolution in the sea-level model, causing a quadratic increase in total CPU time with the total number of input ice history steps, which increases with either the length or temporal resolution of the simulation. In this study, we introduce a new "time window" algorithm for sea-level models that enables users to define the temporal resolution at which the ice loading history is captured during different time intervals before the current simulation time. Utilizing the time window, we assign a fine temporal resolution for the period of ongoing and recent history of surface ice and ocean loading changes and a coarser temporal resolution for earlier periods in the simulation. This reduces the total CPU time and memory required per model time step while maintaining the precision of the model results. We explore the sensitivity of sea-level model results to the model's temporal resolution and show how this sensitivity feeds back onto ice sheet dynamics in coupled modelling. We apply the new algorithm to simulate the sea-level changes in response to global ice-sheet evolution over two glacial cycles and the rapid collapse of marine sectors of the West Antarctic Ice Sheet in the coming centuries, providing appropriate time window profiles for each of these applications. The time window algorithm improves the total computing time by ~50 % in each of these examples, and this improvement would increase with longer simulations than considered here. Our algorithm also allows coupling

time intervals of annual temporal scale for coupled ice-sheet – sea-level modelling of regions such as the West Antarctic that are characterized by rapid solid Earth response to ice changes due to the thin lithosphere and low mantle viscosities.

4.2 Introduction

It is well established that sea-level changes in response to ice-sheet changes feed back onto the evolution of ice sheets (e.g., Gomez et al., 2012; 2015; de Boer et al., 2014; Konrad et al., 2015; Larour et al., 2019). Changes in grounded ice cover perturb the Earth's gravitational field, rotation and viscoelastic solid surface, leading to spatially non-uniform changes in the heights of the sea surface geoid and the solid Earth, i.e., sea-level changes (e.g., Woodward, 1888; Peltier, 1974; Farrell and Clark, 1976; Mitrovica and Milne, 2003). Sea-level changes occur as an instantaneous response to the surface (ice and water) loading changes associated with elastic deformation of the solid Earth and changes in gravity and rotation, followed by a slower response over $O(10^2 - 10^4)$ years due to the viscous mantle flowing back towards isostatic equilibrium, once again accompanied by gravitational and rotational effects. The spatial and temporal scales of the solid Earth response to ice loading changes depend on the rheological structure of the crust and mantle, which are both radially and laterally heterogeneous (e.g., Dziewonski and Anderson, 1981; Morelli and Danesi, 2004; Nield et al., 2014; An et al., 2015; Lloyd et al., 2020). The contribution from viscous deformation to sea-level changes in regions with thinner lithosphere and lower mantle viscosities such as the West Antarctica occurs on shorter timescales ($O \leq 10^2$ yr; e.g., Barletta et al., 2018) compared to regions with thicker lithosphere and higher mantle viscosities such as North America (e.g., Mitrovica and Forte, 2004) and is more localized to the loading changes, calling for higher spatiotemporal resolution for modelling applications in these regions.

The mechanisms through which spatially variable sea-level change influences ice sheets vary in importance depending on whether the ice sheet is marine based or not. The evolution of a marine-based ice sheet is strongly dependent on the slope of bedrock underneath the ice sheet and local ocean depth at the grounding line (e.g., Weertman, 1974; Thomas and Bentley, 1978; Schoof, 2007). Thus, deformation of the bedrock beneath the ice and sea level changes at the grounding line in response to the marine-based ice sheet's growth and retreat affect the ice flux across the grounding line (Gomez et al., 2010, 2012, 2020). In a continental setting, solid Earth deformation beneath an evolving land-based ice sheet alters the slope and elevation of the ice surface in the atmosphere. This, in turn, influences the ice sheet's surface mass balance (e.g., Crucifix et al., 2001; Han et al., 2021; van den Berg et al., 2008).

The interactions between ice sheets, sea level and the viscoelastic solid Earth are active over a range of timescales, and several studies have developed coupled ice sheet-sea level models to investigate these interactions (Gomez et al., 2012, 2013; deBoer et al., 2014; Konrad et al., 2014). Studies have applied coupled modelling to simulate the evolution of the Antarctic Ice Sheet (AIS) during the last deglaciation (Gomez et al., 2013, 2018, 2020; Pollard et al., 2017), the Pliocene (Pollard et al., 2018) and the future (Gomez et al., 2015; Konrad et al., 2015; Larour et al., 2019), the evolution of the Northern Hemisphere ice sheets over the last glacial cycle (Han et al., 2021) and the global ice sheets over multiple glacial cycles (deBoer et al., 2014). These studies capture the interactions between ice sheets and sea level at a temporal resolution of as short as 50 years for the millennial timescale simulations and 200 years for the glacial timescale simulations, but moving to longer simulations or greater spatiotemporal resolution presents a computational challenge.

There is a need to overcome this challenge in order to understand ice sheets and sea-level changes over a wider range of timescales and in greater spatial detail, especially as the spatiotemporal resolution and extent of paleo records improves (e. g., Khan et al., 2019; Rovere et al., 2020; Gowan et al., 2021). Motivations include running simulations over longer time periods in the past (e.g., from the warm mid-Pliocene to the modern), or in higher spatiotemporal resolutions in order to accurately capture rapid paleo ice-sheet variability and sea-level rise events observed in geological records (e.g., Ice Rafted Debris events – Weber et al., 2014; Meltwater Pulse 1A event – Fairbanks, 1989; Deschamps et al., 2012; Brendryen et al., 2019). Furthermore, the present-day WAIS sits atop rapidly responding bedrock (e.g., Barletta et al., 2018; Lloyd et al., 2020; Powell et al., 2020) and is under the threat of rapid retreat in a warming climate (e.g., SROCC, 2019). To capture the dynamics of such rapid ice retreat and the associated sea-level changes, models may need to employ annual-decadal scale resolution (e.g., Larour et al., 2019).

The computational challenge introduced above arises only in a coupled ice sheet – sea level modelling context where (unlike in stand-alone sea level modelling applications where ice cover changes are prescribed, e.g., Peltier 2004; Lambeck 2014) the ice cover changes are unknown at the start of a simulation and predicted by the ice sheet model as the simulation progresses. That is, with the stand-alone ice age sea-level model algorithm described in Kendall et al. (2005), the model takes in the full history of ice loading at the start of the simulation and computes associated sea-level changes across all time steps and outputs results at once at the end of the simulation. On the other hand, in a coupled ice-sheet – sea-level simulation, ice cover changes are predicted by a dynamic ice-sheet model and provided to the sea-level model. The sea-level model, in turn, provides updated bedrock elevation and sea surface heights to the ice-sheet model. This exchange of model output happens at every coupling time interval, which necessitates a ‘forward modelling’ scheme (as described in Gomez et al. 2010) in the sea-level model: The sea-level calculation at every new coupling time interval requires the history of ice loading since the beginning of the coupled simulation as input. The classic forward sea-level modelling algorithm adopted in coupled models employs a uniform temporal resolution throughout a simulation, which leads to a linear increase in the amount of surface loading history with the length of a simulation. The sea-level calculation thus becomes more computationally expensive as the simulation progresses and can make very long or very finely temporally resolved simulations computationally infeasible (e.g., using this framework, coupled simulations in past studies have been limited to 40-125 ky with a temporal resolution of 200 years; Gomez et al., 2013; Han et al., 2021).

To overcome this challenge, de Boer et al. (2014) presented what they called a “moving time window” algorithm in a sea-level model (SELEN, Spada and Stocchi, 2007) and performed coupled ice-sheet – sea-level model simulations over four glacial cycles (410 ky). Using the characteristics of exponentially decaying viscous deformation of the mantle, de Boer et al. (2014) interpolated “future” viscous deformation associated with ongoing surface loading changes and added up the interpolated values at later time steps to obtain deformation due to “past” loading changes (refer to Discussion for more detail). They also applied a coupling time interval of 1 ky, while other studies have demonstrated that simulations over the last deglaciation require coupling intervals of at least 200 years (Gomez et al., 2013) and coupled simulations of future retreat of the Antarctic ice sheet have adopted coupling times of tens of years or less (Gomez et al., 2015; Pollard et al., 2017; Larour et al., 2019) to capture the decadal to centennial-scale interactions between ice sheets, sea level and the solid Earth.

In this study, we develop a new time window algorithm, which takes a different approach from deBoer et al. (2014) to overcome the computational challenges posed in coupled ice-sheet – sea-level modelling. We modify the classic forward model sea-level algorithm introduced in Gomez et al. (2010) by systematically reducing the temporal resolution of earlier ice history while maintaining high resolution in recent loading. We present the algorithm in Section 4.3 and perform a suite of simulations with idealized ice sheet evolution and bedrock geometry to show how the temporal resolution of a sea-level model influences the predicted sea level (Section 4.4.1) and its influence on Northern Hemispheric Ice Sheet dynamics through the last glacial cycle (Section 4.4.2). Next, we apply our time window algorithm to simulate sea-level changes due to the evolution of the global ice sheets over the last two glacial cycles and due to future Antarctic Ice Sheet evolution in the coming centuries (Section 4.4.3), presenting appropriate time window parameters for each scenario. We also demonstrate the efficacy of the time window algorithm in the coupled future Antarctic Ice Sheet-sea level simulation. We finish with a discussion of the results and concluding remarks in Section 4.5.

4.3 Methods

We incorporate our time window algorithm into the forward sea-level model presented in Gomez et al. (2010), which draws on the theory and numerical formulations in Mitrovica and Milne (2003), Kendall et al. (2005), and Mitrovica et al. (2005). In the forward modelling, at every time step t_j, the sea-level model performs a one-step computation between times t_{j-1} and t_j of the global sea-level change associated with ongoing (between t_{j-1} and t_j) and past (between t_0 and t_{j-1}) ice loading changes. The numerical form of this is shown in Equation 18 from Gomez et al. (2010):

$$\begin{aligned}\delta S_j = &- \Delta S_{j-1} + \Delta \mathcal{SL}_j(\delta I_{m(0\leq m\leq j)}; \delta S_{m(0\leq m<j)}; \delta S_j; \delta\omega_{m(0\leq m<j)}; \delta\omega_j)C_j^* \\ &+ \frac{\Delta\Phi_j}{g}C_j^* - T_0\,[\,C_j^* - C_0^*\,].\end{aligned} \tag{4.1}$$

where j is an index for the current time step, δ represents changes over a single time step (e.g., from t_{j-1} and t_j) and Δ represents the total change since the initial time t_0. Thus, δI_j, δS_j and $\delta\omega_j$represent changes in ice thickness (I), ocean loading (S) and rotation vector (ω) between t_{j-1} and t_j and ΔS_{j-1} represents the change in ocean loading before the current time step between t_0 and t_{j-1}. $\Delta\mathcal{SL}_j$ and $\frac{\Delta\Phi_j}{g}$ represent the geographically non-uniform and uniform components of the globally defined total sea-level change, respectively. C^* represents an ocean-mask function, defined as 1 where sea level is positive and there is no grounded ice, or zero otherwise. T_0 represents initial topography at t_0, where the topography is defined as the negative of the globally defined sea level ($\Delta SL_j = \Delta\mathcal{SL}_j + \frac{\Delta\Phi_j}{g}$). Since the focus of this paper is to modify the traditional implementation of the sea-level equation, we refer readers to Mitrovica and Milne (2003), Kendall et al. (2005) and Gomez et al. (2010) for the detailed derivation of this equation and implementation of its numerical algorithm.

Figure 4.1a represents the classic forward sea-level model algorithm (Gomez et al., 2010) where the time interval dt between each time step of the ice history is uniformly fixed throughout a simulation. By the end of the simulation, the total number of ice history steps (N_j) considered in the calculation across the final time step from $t_{j=f-1}$ to $t_{j=f}$ is simply the length of the simulation (L_{SIM}) divided by the prescribed time interval (dt). Thus, the number of time steps in a simulation increases either by performing a longer simulation (i.e., larger L_{SIM} or increasing the temporal resolution (i.e., smaller dt) of a simulation, and the

CPU time increases quadratically.

Figure 4.1b shows the time window scheme that we developed to save computation time in the sea-level model. This algorithm allows users to assign non-uniform time steps across simulations by dividing the simulations into as many as four time intervals. During setup, users define the internal time window lengths (L_{ITW_k}) and temporal resolutions (dt_k) such that each L_{ITW_k} is divisible by dt_k and each dt_k is divisible by the finest temporal resolution of the simulation time window ($dt_{k=1}$, i.e., the coupling time between a dynamic ice-sheet model and the sea-level model). In addition, the sum of all L_{ITW_k}'s must be equal to the total length of a simulation, L_{SIM}. The algorithm then generates a template mask of binary values to resolve the prescribed non-uniform time steps (see Fig. 4.1b-1). It also creates an array of iceload file numbers that, by convention, start at 0 and increment by 1 each time step forward. When the simulation begins (i.e., takes one step forward from $j = 0$ to $j = 1$), the first two elements of this array (iceload files '0' and '1') overlap the last two elements of the binary template (see the top red box in Fig. 4.1b-2). Overlapping elements are multiplied together to generate masked iceload history files for the sea-level model to read in at a given time step. The sea-level model only reads in those ice files masked with binary value of 1. However, to ensure that the solid Earth retains the memory of the initial loading, the sea-level model always reads the initial iceload file (see the dotted box and resulting masked iceload files in Fig. 4.1b-2).

At every simulation step $j > 1$, the template marches forward by one element relative to the iceload file array, and the multiplication process repeats followed by the sea-level calculation. Our algorithm starts filling in the first internal time window to its prescribed length (L_{ITW_1}), followed by the other internal windows in order (L_{ITW_k} for $k = 2, 3, 4$). By the end of the simulation, the time window grows to the full prescribed profile (see the $j = 8$ result in Fig. 4.1b-2).

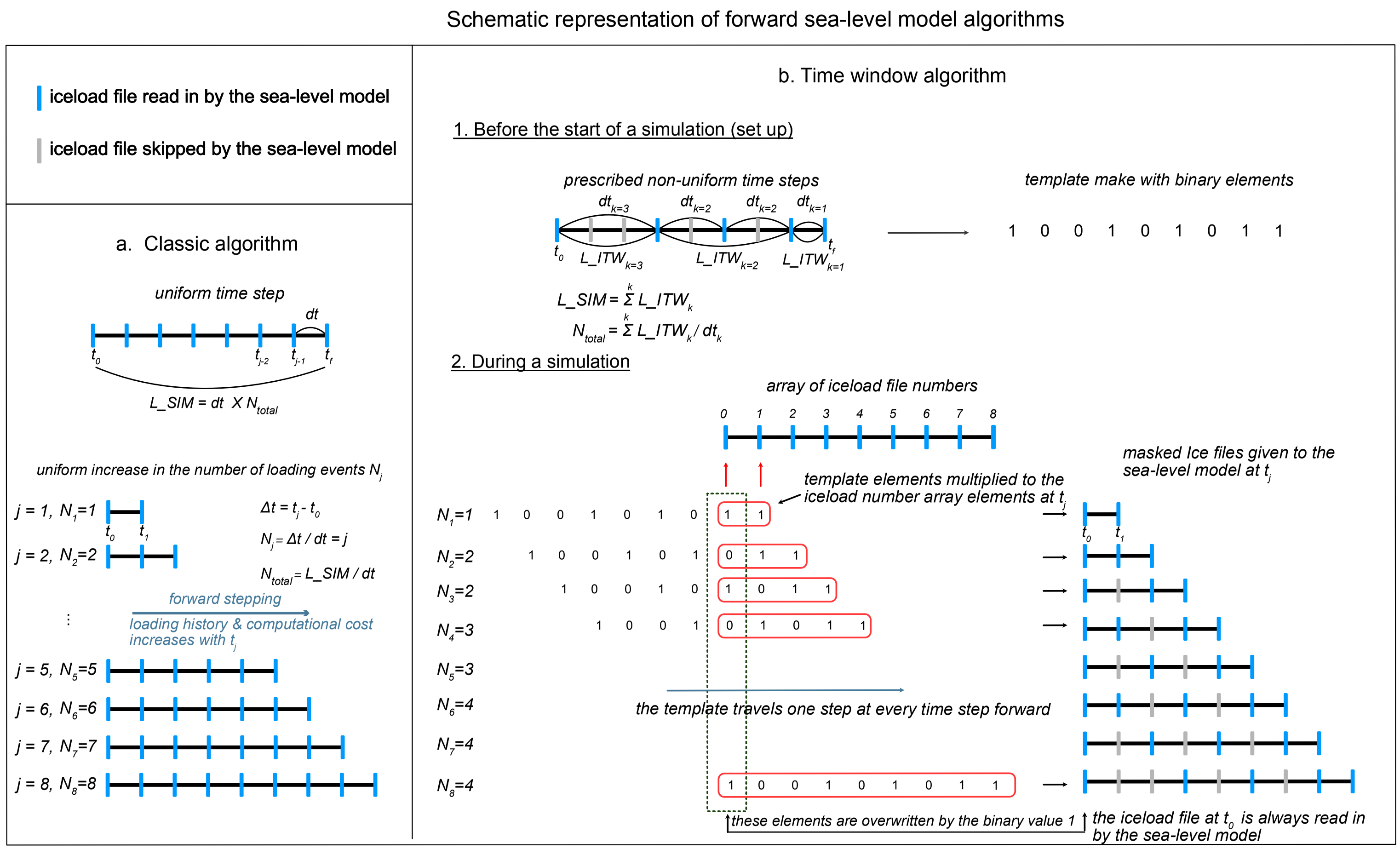

Schematic diagram of classic and time window algorithm in forward sea-level modelling. (a) The classic forward model algorithm in which the details of surface (ice sheet and ocean) loading history are captured in uniformly discretized temporal resolution. (b) The time window algorithm that captures the details of the loading history in non-uniformly discretized temporal resolution. The user assigns *k* number of internal time windows, each of which has a total length of L_ITW_k and internal time steps of size dt_k. The ice load files shown as blue vertical bars are the ones that are multiplied by a template element with a value ‘1’, and grey bars are multiplied by ‘0’.

Figure 4.1

Overall, this time window algorithm limits the increase in the amount of surface loading history with simulation length or temporal resolution, improving the computational efficiency of the sea-level model calculations (compare N_j values in Fig. 4.1a and Fig. 4.1b-2). The time window algorithm also enables the sea-level model to capture both short- and long-term interactions between ice sheets, sea level and the solid Earth in coupled ice-sheet - sea-level simulations.

In the next section, we perform a suite of sensitivity tests performing standalone sea-level simulations and coupled ice-sheet – sea-level simulations to test the sensitivity of model results to the temporal resolution of the sea-level model. The sea-level model takes two inputs, an Earth model and an ice history model. We adopt a 1-D Earth model in all simulations; the elastic and density profile of the Earth structure are given by the seismic model PREM (Dziewonski and Anderson, 1981). For mantle viscosity, we adopt a lithospheric thickness of 120 km and upper mantle viscosity of 5×10^{20} Pas and lower mantle viscosity of 5×10^{21} Pas in Sections 4.4.1-4.4.3.1. For Section 4.4.3.2 in which we perform simulations over Antarctica, we adopt the best-fitting radially varying Earth model from Barletta et al. (2018), characterized by a lithospheric thickness of 60 km and upper mantle viscosities of $\sim 10^{18} - 10^{19}$ Pas. Ice history inputs are described in each section. In all simulations, we perform sea-level calculations using a spherical harmonics expansion up to degree and order 512. For coupled ice sheet-sea level simulations, we couple the 3D-PSU ice sheet-shelf model (Pollard and DeConto, 2012) to the sea-level model. The flux across the grounding line is parameterized following Schoof (2007). The ice-sheet model does not include the marine ice-cliff instability (MICI) mechanism. Readers are referred to Han et al. (2021) and DeConto et al. (2021) for more detailed set-ups for the Northern Hemispheric and Antarctic Ice Sheet simulations.

4.4 Results

4.4.1 Sensitivity of sea-level model outputs to temporal resolution

Before exploring the new time window algorithm in Sections 4.4.2 and 4.4.3, we begin by performing a series of experiments with a standalone sea-level model adopting the classic algorithm to demonstrate how predicted topography changes (that is, negative of sea-level changes) at near and far-field locations vary with the (uniform) temporal resolution of the ice history (as in Fig. 4.1a). We generate an idealized axis symmetric input ice history based on the equation for an equilibrium ice surface profile for viscous ice provided in Cuffey and Paterson (1969, The Physics of Glaciers), with the ice sheet centred at the South Pole (Fig. 4.2g). The initial topography for the ice growth-phase is idealized such that its elevation is 1000 m between latitudes 60-90 °S and -1000 m (ocean with a depth of 1000 m) everywhere else. In Fig. 4.2, we consider predicted changes in topography at three locations: A location at the centre of loading (90 °S), near the periphery of the ice sheet at its maximum extent (65 °S, where the peripheral bulge formed around the ice sheet is largest), and in the far-field at the equator (0 ° latitude). We begin by discussing the general behaviour of topography at these sites in benchmark simulations performed at a temporal resolution of 1 ky (shown by the black dots in Fig. 4.2).

Figures 4.2a-c show results from buildup-phase simulations. The ice sheet thickness and extent grow over 20 ky at a uniform rate at the centre and the edge of the loading, to the thickness of 3500 m (top frame of Fig. 4.2a) and the extent reaching latitude 65 °S. In response, the topography subsides at the centre of loading (middle frame of Fig. 4.2a) and uplifts at the peripheral point (middle frame of Fig. 4.2b). Far-field equatorial sites experience a decrease in sea level

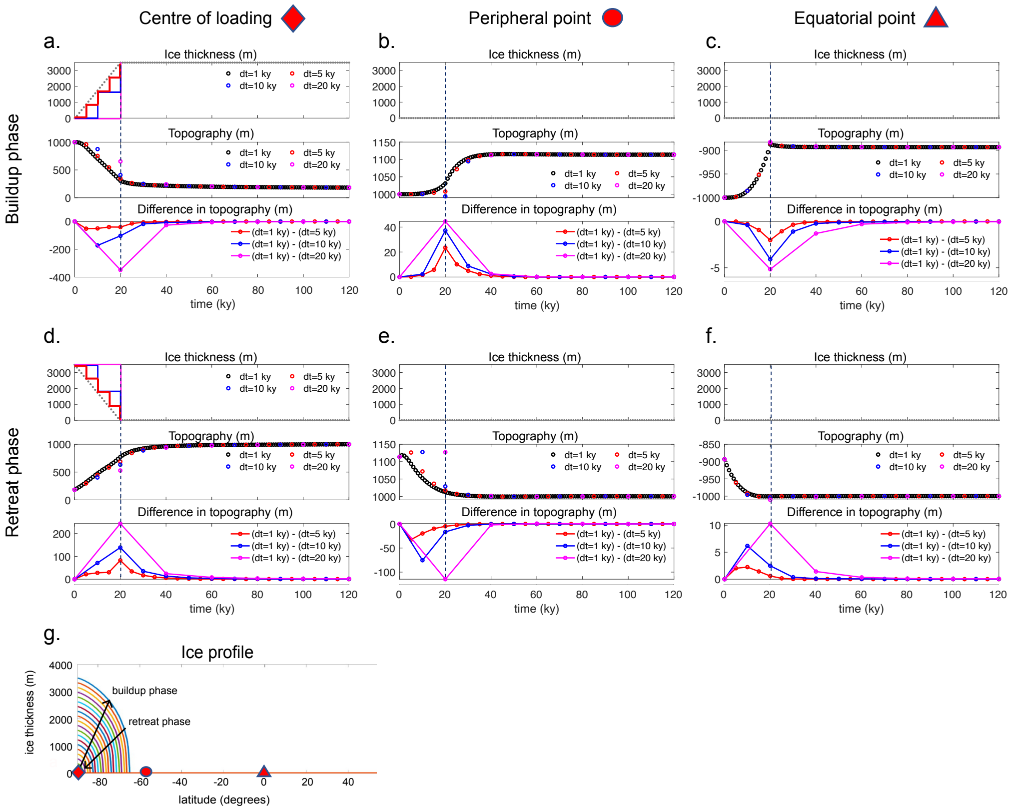

Figure 4.2: The sensitivity of predicted topography (sea level) changes to the temporal resolution (*dt*) of the sea-level model. (a-f) Results of idealized simulations in which input ice history evolves at a uniform rate in axis symmetric dome-shape during a buildup phase (panels a-c) and a retreat phase (d-f) at the centre of loading (first column), peripheral point (second column) and far-field equatorial point (third column). On each panel, the top frame shows ice thickness in meters, middle frame shows the elevation of topography in meters from simulations that incorporate the uniform time stepping of dt =1 ky (black dots), 5 ky (red dots), 10 ky (blue dots), and 20 ky (magenta dots), and bottom frame shows differences in predicted topography from the simulation with the benchmark resolution (black dots in the middle panel, $dt = 1$ ky) and coarser temporal resolution (red, blue and magenta dots in the middle panel). Dashed vertical lines at 20 ky mark the timing at which the ice stops loading. The staircase-like solid lines in (a) and (d) represent the step function of ice loading change in respective simulations. (g) schematic showing the evolution of ice in the idealized simulations and the locations of the center of loading and peripheral and equatorial sites discussed in frames (a-f). Coloured curves show snapshots of ice thickness at 1 ky intervals during the retreat/advance that occurs in the first 20 ky of the simulation.

(increase in topography) as ice becomes locked up on land (middle frame of Fig. 4.2c).

Figures 4.2d-f show results over a 20-ky long retreat phase. The initial topography for these simulations is adopted from the final topography modelled in the benchmark buildup-phase simulation with $dt = 1$ ky (i. e., black dots in the middle frame of Fig. 4.2a). As the ice sheet retreats, the topography uplifts at the center of the ice load (middle frame of Fig. 4.2d), subsides at locations peripheral to the ice (middle frame Fig. 4.2e) and the far-field regions experience sea-level rise (middle frame of Fig. 4.2f).

Next, we compare simulations performed at lower temporal resolutions of 5 ky, 10 ky and 20 ky to our benchmark simulations at 1 ky resolution. Though all of the simulations capture the main characteristics of deformation at each location, the magnitude of the deformation during both the ice-sheet buildup and retreat phases at all three locations decreases with decreasing temporal resolution (i.e., higher dt). For example, when comparing the 5 ky-resolution simulation to the benchmark simulation for the buildup phase (red line in the bottom frame of Fig. 4.2a), the subsidence beneath the ice during ice growth is reduced by up to 51.7 m. Likewise, the simulations with 10-ky and 20 ky-resolution (blue and pink lines) underestimate the subsidence by up to 173 m and 349 m, respectively. The underestimation is due to the timing of the applied load in each simulation; as shown by the step function ice loading increases in the top frames of Figs. 4.2a and d, simulations with coarser temporal resolution have delayed increases in ice loading. For example, the loading change for the first 10 ky and the 5 ky resolution simulation is applied in two steps at 5 and 10 ky, while in the 10 ky resolution simulation, the full load is applied once at 10 ky. The latter thus does not capture the viscous signal due to the loading that takes place before 10 ky. These maximum differences ("errors") and the spread of the errors decrease gradually towards zero with time. For these simulations, the errors in total topography change become less than 1 % of the total subsidence (801 m) in the benchmark simulation by 60 ky (i.e., within 40 ky after the completion of loading/unloading event at 20 ky).

Note that at the equatorial site, the rate at which the error decreases towards zero is slower than the near-field sites (e.g., see the pink line after reaching its peak in Figs. 4.2c and f). This is because there is active water loading occurring at this site even after the ice has stopped evolving, which prolongs the differences in deformation of the lower resolution simulations compared to the benchmark simulation ("water-loading effects", e.g., Han et al., 2018).

The timing of the maximum errors at each site corresponds to the size of topography changes at the site, which in turn depends on the distance to, and size of an evolving ice sheet. For example, at the near-field sites during the buildup phase, the peak differences in simulations occur as soon as the ice starts loading at the centre-of-loading site (bottom frame of Fig. 4.2a) while at the peripheral-bulge site the peak differences occur at 20 ky when the ice sheet reaches its maximum volume and extent (bottom frame of Fig. 4.2b). During the retreat phase, the peak differences at the peripheral-bulge site occur as soon as the ice starts retreating. The differences then get smaller at this site as the ice sheet and its peripheral bulge retreat further away from the site towards the pole (bottom frame of Fig. 4.2e). The ice sheet's centre, on the other hand, experiences the peak differences at 20 ky when ice loading directly above this site disappears (bottom frame of Fig. 4.2d).

While the timing of the maximum differences in the near-field sites is most sensitive to the size and proximity of ice to the sites, at the equatorial site it is the most sensitive to the ice volume change. During the buildup phase, the greatest sea-level changes at the equatorial site (and thus the maximum errors) occur at

20 ky (bottom frame of Fig. 4.2c). During the retreat phase, the errors peak as soon as the ice starts retreating and the rate of change of ice volume is largest (bottom frame of Fig. 4.2f). For both phases, the timing of maximum error is related to the maximum ice volume change. We note that the ice thickness at the centre of loading (as shown in the top frames of Figs. 4.2a and d) changes linearly, but the actual volume change is nonlinear because of the changes in the ice sheet's extent; the volume change across one time step is greater when the ice sheet is more extensive.

Overall, the idealized-loading simulations show that sea-level model outputs are sensitive to the model temporal resolution. This is because the timing of ice loading is different with different temporal resolutions. The sensitivity at a location depends on its setting (above or below sea level), the size of ice loading changes and the distance (near-field or far-field) to the changing ice load. However, the sensitivity at all sites decreases with time after the ice loading event. These results suggest (as expected from the literature on the viscoelastic response of the Earth to surface loading, e.g., Peltier, 1974) that higher resolution information about ice cover changes is required for the ice history immediately prior to the current time step in a simulation, and lower resolution will suffice for earlier ice cover changes. The specific temporal resolution required will depend on both the rates of change of the ice cover and the Earth's viscosity structure, which we explore in two contrasting examples in Section 4.4.3.

In this section, we have highlighted the sensitivity of predicted sea-level changes to the temporal resolution of the inputted ice history in classic, standalone sea-level simulations. In the following section, we explore how the differences in sea level predicted with different temporal resolution influence the ice sheet evolution in coupled ice sheet – sea level simulations and how the time window algorithm can reconcile the errors.

4.4.2 Sensitivity of modelled ice sheet dynamics to temporal resolution with a coupled sea-level model

This section explores how the differences in predicted sea-level change due to temporal resolution of the input ice history discussed in the previous section impact ice dynamics in coupled ice-sheet-sea-level model simulations. To do this, we perform a suite of coupled simulations over the Northern Hemisphere through the last glacial cycle (125 ky) incorporating different sizes of uniform time steps with the standard algorithm (Fig. 4.3a) and nonuniform time steps applying the time window algorithm (Fig. 4.3b). We employ the PSU 3D dynamic ice-sheet model by Pollard and DeConto (2012) and adopt the same set of ice model parameters (e.g., climate forcing, basal friction, spatial and temporal domain and resolutions) used in the simulations from Ch. 3.3 of this thesis. The ice-sheet model has a standalone time step of 0.5 yr. We note that the coupling interval over which the ice-sheet model and sea-level model exchange their outputs (i.e., ice thickness and topography, respectively) corresponds to the size of the most recent time step within the sea-level model (i.e., dt_1 in Fig. 4.1b).

Figure 4.3a demonstrates that the simulations with a higher temporal resolution (i.e., smaller ‘dt’ in the sea-level model and thus more frequent exchange of outputs between the ice-sheet model and the sea-level model) yield a higher volume of modelled NHIS during the time between ∼80-20 ka. Differences in ice volume between the simulations start diverging around 80 ka and persist until the Last Glacial Maximum (20 ka) in the model time. The difference in sea-level-equivalent ice volume is up to 11.6 m between the simulations with time intervals of $dt = 0.1$ ky and $dt = 1$ ky at 80 ka (compare black dotted line and blue line in Fig. 4.3a). Spatially, the differences occur mainly in the Laurentide Ice Sheet in North America (we don’t show this in the figure). As illustrated in Fig. 4.2, a lower temporal resolution of the ice history during the Laurentide Ice

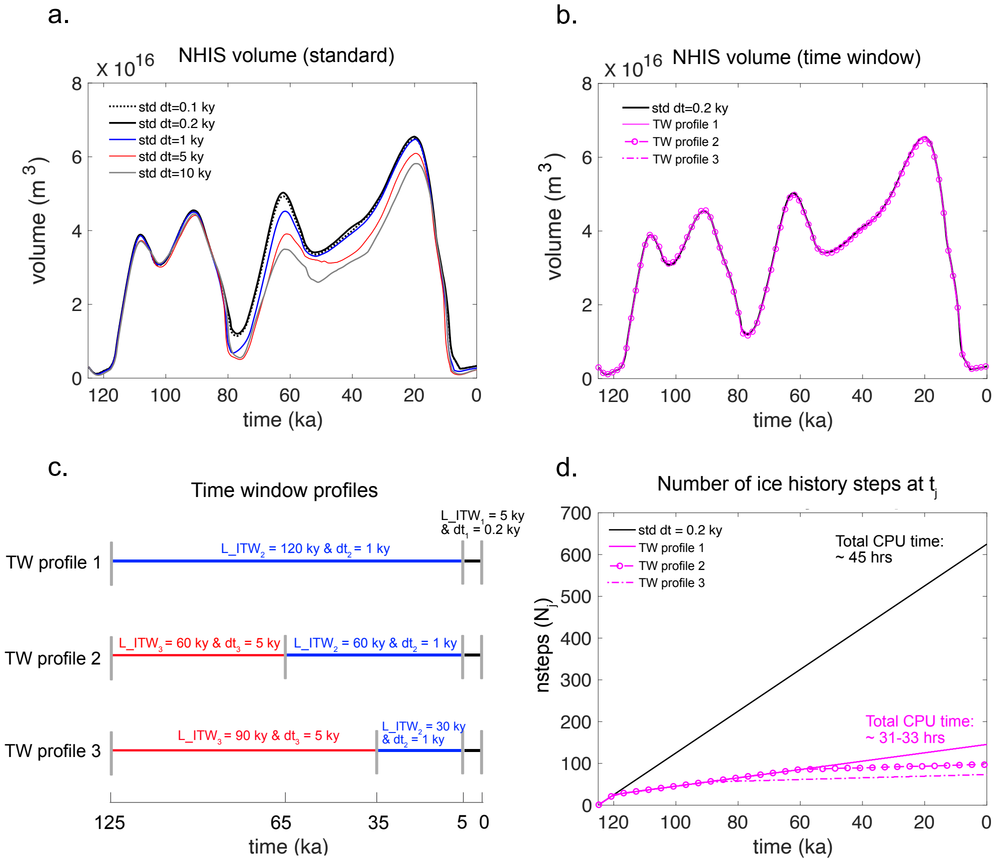

Figure 4.3: Modelled Northern Hemispheric Ice Sheet volume through the last 125 ky from ice-sheet – sea-level coupled simulations that incorporate (a) "standard", uniform time stepping (and thus coupling time interval) of 0.1 ky (black-dotted line), 0.2 ky (black line), 1 ky (blue line), 5 ky (red line) and 10 ky (grey line). (b) Non-uniform time intervals assigned by the time windows of three different profiles (magenta lines) as schematically shown in (c): TW profile 1 applies two internal time windows L_{ITW_1} and L_{ITW_2}, each of which covers 5 ky and 120 ky over the entire simulation with $dt_1 = 0.2$ ky and $dt_2 = 1$ ky. TW profile 2 applies three internal time windows, $L_{ITW_1} - L_{ITW_3}$, each of which covers 5 ky, 30 ky and 90 ky with $dt_1 = 0.2$ ky, $dt_2 = 1$ ky and $dt_3 = 5$ky, and TW profile 3 also applies three internal time steps, each of which covers 5 ky, 60 ky and 60 ky with $dt_1 = 0.2$ ky, $dt_2 = 1$ ky and $dt_3 = 5$ ky, respectively. Note that all three profiles assign the first internal time window (L_{ITW_1}) to a 5-ky length with the internal time step (dt_1) of 0.2 ky. (d) the number of ice history steps (N_j) that the sea-level model considers at every time step t_j.

Sheet retreat before 80 ka leads to less uplift of the bedrock beneath the ice sheet, keeping the ice surface at a lower (and thus warmer) elevation in the atmosphere. This lower ice elevation causes more intense deglaciation of the Laurentide Ice Sheet. It also prohibits the ice sheet from growing large during buildup phases later on (the role of deformational effects on ice sheet dynamics is discussed in detail in Han et al. 2021). Furthermore, The NHIS volume fluctuation becomes less smooth when the coupling time interval is increased to $dt = 5$ ky and $dt = 10$ ky (red and grey lines in Fig. 4.3a). We presume that this is because a larger change in bedrock height over a longer coupling time causes the ice-sheet model to respond more strongly. These results suggest that Northern Hemisphere coupled simulations over the last glacial cycle require a coupling time of hundreds of years or less to accurately capture the interactions between the ice sheets, bedrock elevation and sea level (compare the black-dotted, black and blue lines in Fig. 4.3a).

While we might expect that the compute time would always increase with higher temporal resolution in the case of uniform time stepping (Fig. 4.1a), it is interesting to note that the 10-ky time-step simulation took an hour longer than the 5-ky case. This is because in the former simulation, the ice model took longer to converge to a solution because of infrequent and dramatic bedrock changes provided by the sea-level model (as hinted by the unstable fluctuation in the ice volume - the grey line in Fig. 4.3a). Finally, while there are very small differences in predicted ice volume between the $dt = 0.2$ ky and $dt = 0.1$ ky simulations (black and black- dotted lines in Fig. 4.3a), CPU time increases from ∼45 to ∼98 hr, suggesting that $dt = 0.2$ ky is a suitable choice of coupling time for glacial cycle simulations.

In Fig. 4.3b, we apply the time window algorithm to the coupled glacial-cycle simulation rather than adopting uniform temporal resolution in the ice history.

We perform three simulations with different time window profiles illustrated in Fig. 4.3c. All simulations incorporating the time window predict the ice volume changes of the standard simulation with the uniform time stepping of 0.2 ky well (see the magenta lines and the black line overlapping in Fig. 4.3b), and the CPU time is reduced by ∼12-14 hr (Fig. 4.3d). In the standard simulation, the number of ice history files that the sea-level model needs to read in at a given time step increases linearly with time (black line in Fig. 4.3d). In contrast, with the time window algorithm, it increases linearly initially within the first internal time window ($L_{ITW_1} = 5$ ky), and then nearly capped, increasing by one intermittently when transitioning from one internal time step to the next. (e.g., in Fig. 5c, g and k, colored lines nearly flatten). The number of files is capped at 145 files in time window profile 1, at 97 files in profile 2, and at 73 files in time window profile 3. In all cases, the time window algorithm allows for faster computation while maintaining precision (Figs. 4.3b and d).

In this section, taking the last glacial cycle as an example, we have shown that a coarse temporal resolution (e.g., $dt = 1$ ky or longer) causes less precise coupled ice-sheet – sea-level simulation results. We have also demonstrated that how the time window algorithm can be used in coupled simulations to maintain the precision of the modelled topography changes and ice sheet dynamics while significantly reducing the computational cost compared to simulations with the standard algorithm. In the same way, the time window algorithm can be applied to other coupled simulations that are otherwise infeasible. In the next section, we derive time window profiles that are suitable for two-glacial-cycle global ice-sheet simulations and future projections of a rapidly retreating Antarctic Ice Sheet.

4.4.3 Derivation of time window profiles for different applications

In this section, we apply the time window algorithm in the sea-level model to two contrasting examples. First, we consider sea-level changes in response to the evolution of global ice sheets over the last two glacial cycles (240 ky) modified from Han et al. (2021). Then, we consider a simulation of the rapid future retreat of the West Antarctic Ice Sheet in the coming centuries taken from DeConto et al. (2021). West Antarctica is known to have an upper mantle viscosity up to several orders of magnitude lower than on average (Barletta et al., 2018; Lloyd et al., 2020; Nield et al., 2014). For each scenario, we perform a suite of simulations in which we vary the time window parameters (i.e., L_{ITW_k} and dt_k; Fig. 4.1) and compare them to a benchmark simulation with uniform high-resolution time stepping to arrive at an optimal choice of a time window profile. Here we note that the experiments are first done in standalone sea-level simulations (i.e., ice cover is prescribed rather than provided by a dynamic ice-sheet model). This is partly because the benchmark coupled simulation for the two glacial cycles NH simulation is infeasible without the time window algorithm. After we derive the respective time window profiles, we perform a suite of coupled future WAIS-sea level simulations to test the performance of the time window profile derived in the section.

4.4.3.1 Application to global ice cover changes over the last two-glacial cycles

Figure 4.4 shows ice volume changes over the last 240 ky and snapshots of the maximum and minimum extent of global ice cover predicted from a coupled ice sheet – sea-level model simulation in Han et al. (2021) that we adopt here as an input to the sea-level model. The original simulation covers the last glacial

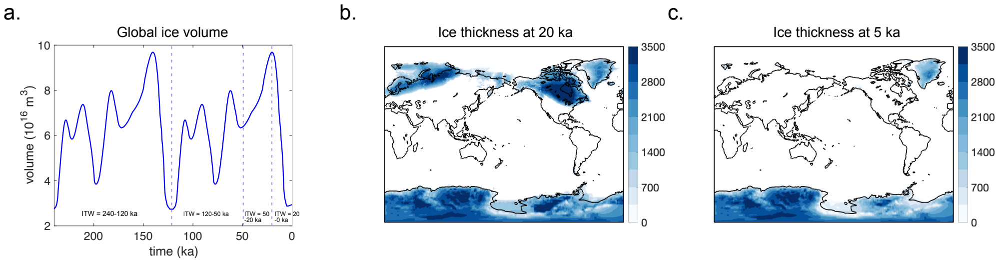

Figure 4.4: Changes in global ice sheet volume and thickness and in the 240-ky simulation. Vertical dashed lines mark the internal time windows. (a) Global volume variations through the last 240 ky. (b, c) Snapshots of ice thickness at (b) 20 ka and (c) 5 ka.

cycle (125 ka). It includes ice-cover changes predicted with the dynamic PSU ice-sheet model (Pollard and DeConto, 2012) in the Northern Hemisphere and Antarctic ice cover changes taken from the ICE-6GC ice history model (Argus et al., 2014; Peltier et al., 2015; see Section 3.3 of this thesis). To extend our ice history input to cover two glacial cycles, we first take the ice history for 120 ka from the original simulation (Han et al. 2021), then repeat this ice history to cover an additional glacial cycle going back to 240 ka. We replace the ice history between 125-120 ka with the ice history between 120-115 ka. This is to make the ice volume curve continuous at the last interglacial. We note that the goal of this experiment is not to produce an accurate glacial history but to produce a sample long timescale, global ice history that contains the spatiotemporal detail provided by a dynamic ice-sheet model.

To explore the choice of time window parameters for this global glacial-cycle scenario, we first perform a standard sea-level simulation in which we assign a uniform temporal resolution of 0.2 ky throughout the 240 ky simulation. We take this simulation as our benchmark, and then perform a suite of simulations in which we systematically vary the temporal resolution (dt) of internal time windows (ITW) that cover periods 240-120 ka, 120-50 ka and 50-20 ka in the simulation (see the internal time windows marked by dashed lines in Fig. 4.4a). We choose these internal time windows based on the timing of ice volume variations and the results of our idealized tests in Section 4.4.1. That is, our first internal time window covers the last deglaciation, the next covers the preceding growth phase in the simulation, then the rest of the glacial cycle back to the last interglacial, and finally the entire previous glacial cycle. We note that in the absence of knowing the specific details of the ice cover changes a priori (as in coupled model simulations), the internal time windows may also be set based on the timing of the climate forcing that serves as input to the model. Sensitivity tests (not shown here) varying the internal time windows lengths to account for potential offsets between the timing of climate forcing and ice sheet response indicate that the timing of these internal time windows need not be set very precisely, with less sensitivity for earlier ice history.

When we explore each internal time window in turn by varying the internal time step (i.e., temporal resolution dt), starting from the earliest, and fixing the temporal resolution at 0.2 ky for all periods beyond the internal time window. Then, we compare the total CPU time (Fig. 4.5d) and the precision of our results by calculating the root mean squared error (RMSE) in predicted topography at a given time step relative to the benchmark simulation. The RMSE is calculated based on the following expression:

$$RMSE(t_j) = \sqrt{\frac{1}{N}\sum_{l}^{L=512}\sum_{m}^{M=1024}[T(t_j,l,m)_{std} - T(t_j,l,m)_{tw}]^2} \qquad (4.2)$$

Where j represents the time index, N represents the number of grid points (in our case, 512 times 1024 for the Gauss-Legendre sea-level model grid), $T(t_j,l,m)_{std}$ and $T(t_j,l,m)_{tw}$ represent predicted topography at time t_j from the standard simulation and the time window simulation.

Once we choose an optimal temporal resolution for the internal time window based on the calculated RMSE and CPU time, we move on to explore the next internal time window and we repeat the same procedure.

We start by exploring the internal time window covering the earliest period between 240-120 ka (see the purple bar in Fig. 4.5a). Varying the internal time step between 5-40 ky for this period (Fig. 4.5a-d), the RMSE in predicted topography is zero for the first 120 ky (Fig. 4.5b) because the time window profile matches the 0.2 ky ice history time-stepping in the benchmark simulation (as shown in the black bar indicating 120-0 ka in Fig. 4.5a). RMSE then starts increasing for all simulations once the simulations proceed past 120 ka. The simulations with an internal time step of 20 ky and 40 ky show noticeably greater RMSE than the simulations with a smaller internal time step of 5 ky and 10 ky, both of which have RMSE below 0.2 m throughout the last glacial cycle except at 5ka when it rises to 0.35 m. The fluctuations in the RMSE curves are mainly associated with the sea-level model not capturing the highs and lows in the input ice history. Taking the simulation with the internal time step of $dt = 40$ ky (blue line in Fig. 4.5b) as an example, the RMSE peaks at around 40 ka because the sea-level model only captures snapshots of ice at their local minimum (at 240 ka, 200 ka and 160 ka), missing multiple glacial peaks at 230 ka, 210 ka and 190 ka within those periods (Fig. 4.4a).

Figure 4.5(c and d) shows the total number of ice history steps considered and the cumulative CPU time it has taken for the sea-level model to perform calculations at time step t_j in the standard simulation (grey line) and all other simulations that incorporate the time window parameters (non-grey lines). The standard simulation increases linearly in total number of ice history steps up to 1200 and quadratically in CPU time, and the entire 240-ky long simulation takes $\sim$ 58.4 hr. The total number of ice history steps starts flattening for the

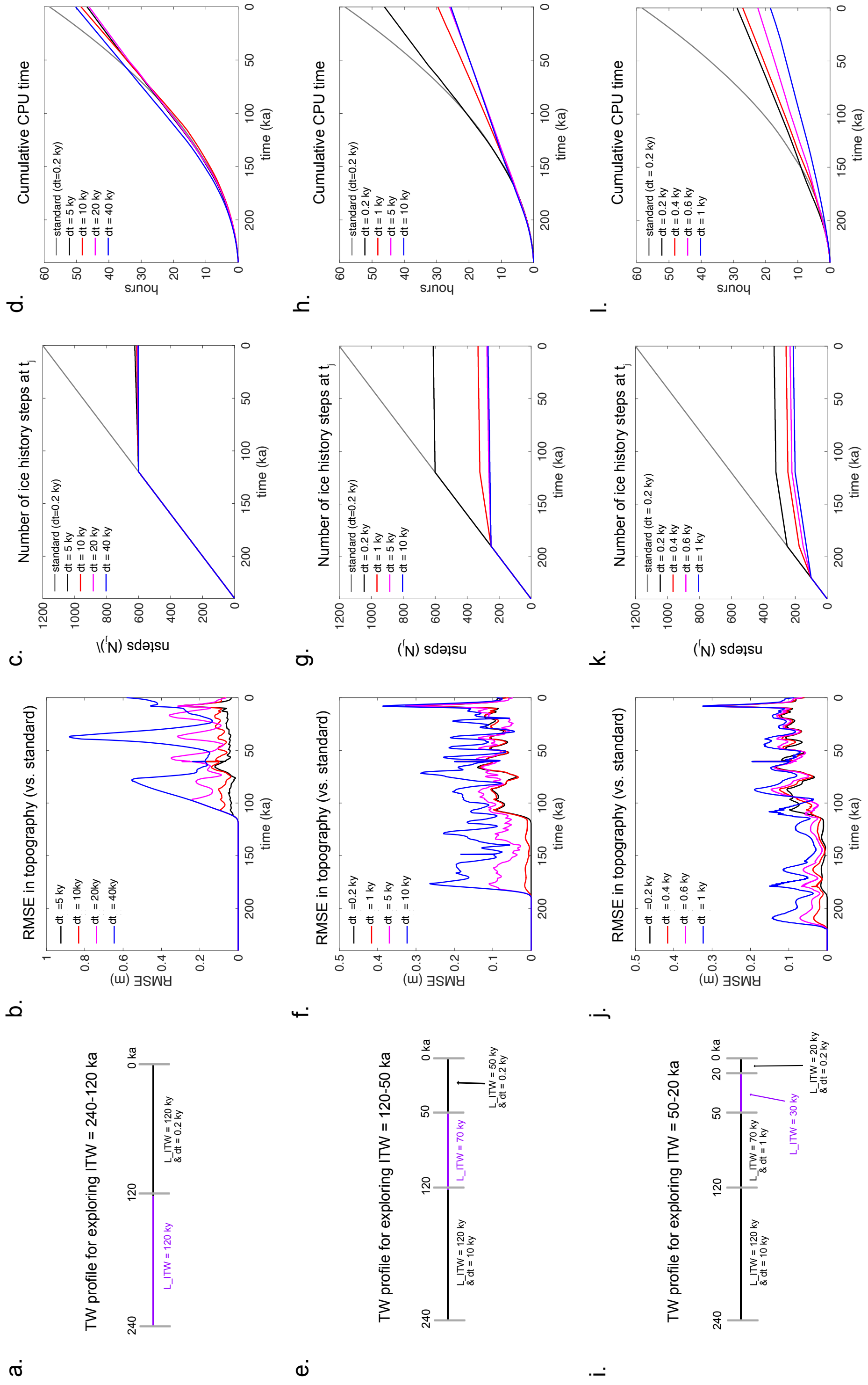

Figure 4.5: Time window profiles, RMSE in predicted topography, the number of loading events (nsteps, N_j) and the total CPU times in the global simulations through the last 240 ky. Results from the simulations in which we explore the internal time windows that cover the periods between (a-d) 240-120 ka, (e-j) 120-50 ka and (i-l) 50-20 ka. Note that the benchmark simulation assigns a uniform time step size of 0.2 ky throughout the simulation.

Figure 4.5

simulations with a travelling time window (coloured lines) at 120 ka, resulting in the reduction in the CPU time to ∼ 46.8-50.3 hr. We note that the CPU time starts diverging earlier than 120 ka, and this is because measured CPU times fluctuate by 10-17 % even with the same CPU (Intel Gold 6148 Skylake @ 2.4 GHz). Based on these results, we choose an internal time step of 10 ky for the first internal time window (240-120 ka) and proceed to explore the internal time steps for the next internal time window between 120-50 ka.

Figure 4.5(e-h) shows the results of simulations in which we vary the internal time step for the period between 120-50 ka (purple bar in Fig. 4.5e) while fixing the first period from 240-120 ka to $dt = 10$ ky. Here we see that the simulation with temporal resolution of 1 ky (red line in Fig. 4.5f-h) has comparable RMSE to the RMSE in the simulation with temporal resolution of 0.2 ky for this internal time window (black line in Figs. 4.5f-h) with comparably low computing time to the other lower temporal resolution simulations (pink and blue lines in Figs. 4.5f-h). The total CPU time is reduced to ∼29.7 hr in this case, a 49 % reduction compared to the benchmark simulation for this internal time window (compare red and grey line in Fig. 4.5h). Hence, we adopt a temporal resolution of 1 ky for this period.

Finally, Figure 4.5(i-l) explores the effects of varying the size of the internal time step for the period between 50-20 ka (purple bar in Fig. 4.5i). Based on the above discussion, the size of the internal time steps for the periods 240-120 ka and 120-50 ka are fixed at $dt = 10$ ky and 1 ky, respectively. We arrive at the final optimal time window profile by identifying $dt = 0.4$ ky (red line in 5h-i) as an optimal internal time step for this internal time window. This profile keeps the RMSE in output topography below 0.4 m throughout the entire simulations. The total CPU time is reduced to ∼26.9 hr, a 54% reduction compared to the benchmark with uniform time stepping of 0.2 ky. We note that the CPU times shown in Fig. 4.5 are based on standalone sea-level simulations only. This time window algorithm is designed for sea-level calculations performed within a coupled ice sheet – sea level simulation, and compute times will be similarly reduced in this context. Moreover, the reduction will grow for longer simulations as the CPU time in the standard simulation will increase quadratically whereas the time window simulation will suppress the rapid growth of rate of increase.

4.4.3.2 Application to future Antarctic Ice Sheet changes

In this section, we develop a time window profile for application to simulating future West Antarctic Ice Sheet (WAIS) collapse based on the same methodology that we use for the global glacial-cycle scenario in the previous subsection. We adopt a simulation of future AIS evolution from DeConto et al. (2021) in which marine sectors of the WAIS collapse over hundreds of years. The simulation does not include ice shelf hydrofracture and ice cliff instability (Pollard et al., 2015) and the East Antarctic Ice Sheet remains intact during the simulation. The rapid retreat of the WAIS and the weak solid Earth structure together suggest that ice sheet-solid Earth interactions may need to be captured at decadal timescales or less. We therefore perform our benchmark sea-level simulation for this scenario with a uniform (standard) temporal resolution of $dt = 1$ yr. We also perform additional standard simulations with a coarser temporal resolution of $dt = 5$ yr, 10 yr and 50 yr for comparison. We then perform a suite of simulations in which we vary the temporal resolution between $dt =$ 5-50 yr within the four internal time windows shown in Fig. 4.6a (also see the purple bars in Figs. 4.7a, e and i).

Figure 4.6 shows AIS volume changes and maps of the AIS thickness at the beginning and end of the 550-yr simulation beginning in 1950 from Deconto et al. (2021) along with total sea-level change in Antarctica across the simulation predicted from our benchmark standalone sea-level simulation. Marine-grounded

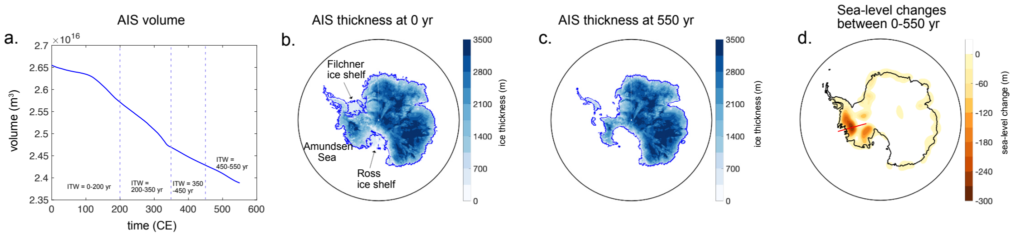

Figure 4.6: Changes in Antarctic Ice Sheet volume and thickness and total sea-level changes over 550 years. (a) AIS volume variations through 550 yr. (b, c) Snapshots of ice thickness (blue) and grounding lines (blue contour lines) at (b) 0 yr and (c) 550 yr. (d) Total sea-level changes between 0-550 yr associated with the ice loading changes between 0-550 yr. Note that the regions (in yellow and red) that show negative sea-level changes are where sea level has fallen because of solid Earth uplift and the drawdown of sea surface height associated with ice mass loss. Red line represents a cross section perpendicular to a grounding line in the West Antarctic region where the most intense sea-level change (fall) happens.

ice sheets in the Amundsen Sea Embayment in West Antarctica retreats completely along with the Ross and Ronne-Filchner Ice Shelves (Figs. 4.6b-c) and strong sea-level fall occurs in the region (shown in dark orange in Fig. 4.6d). Accordingly, in these marine sectors, it becomes important to capture deformation at the grounding line accurately within coupled model simulations. In the remainder of this section, we first select a time window profile based on global RMSE in Fig. 4.7 and then we test the performance of the chosen time window at capturing deformation at the grounding line in Fig. 4.8.

We start by finding an optimal internal time step (i.e., temporal resolution) for the period between 0-200 yr simulation time (Fig. 4.6a; also marked as a purple bar in Fig. 4.7a) during which the WAIS starts retreating, and the rate of retreat starts accelerating just after 100 yr. Fig. 4.7b shows that RMSE in predicted topography compared to the benchmark simulation start increasing after 350 yr (this is because the temporal resolution is set to be the same as that in the benchmark simulation during the first 350 yr). The RMSE remain smaller than 10 cm for simulations with an internal time step of 10 yr and 25 yr (red and magenta lines in Fig. 4.7b) and below 0.85 cm with an internal time step of 5 yr (black line in Fig. 4.7b). The number of ice history steps (N_j) that the sea-level model considers at time step t_j starts diverging after 350 yr. At the last time step of the simulation, the benchmark simulation considers 550 ice history steps while N_j considered for the simulations with an internal time step $dt = 5 - 50$ yr are reduced by ∼ 29-36 %, respectively (Fig. 4.7c). The total CPU times are reduced by ∼ 4-8 %, from ∼17 hr with the standard simulation to between ∼15.6-16.3 hr for the others (Fig. 4.7d). We choose $dt = 5$ yr as an appropriate internal time step for the period between 0-200 yr (the black lines in Figs. 4.7b-d), which minimizes the RMSE with comparable CPU time to the other simulations.

Next, we explore the period 200-350 yr (Figs. 4.7e-h) during which the most intense ice loss occurs (Fig. 4.6a). The simulations with internal time step of 25 yr and 50 yr show a noticeable increase in RMSE compare to those with a smaller internal time step (compare the blue and magenta lines to red and black lines in Fig. 4.7f). Comparing the simulations with a finer resolution of $dt = 5$ yr (black line) and coarser resolution of $dt = 50$ yr (blue line), the former considers a total of 270 ice history steps and the compute time is ∼11.5 hr, which is 27 more ice history steps and ∼2 hr longer compute time than the latter simulation. Since the simulation with the fine internal time step of 5 yr is entirely feasible, and the RMSE in predicted topography is minimal below 0.04 m, we choose $dt = 5$ yr (black lines in Figs. 4.7f-h) as our temporal resolution for this period.

Finally, Figure. 4.7i-l show the results of exploring the temporal resolution for the period between 350-450 yr. Again, the simulation with the internal time step of 5 yr outperforms the other simulations that have a coarser temporal resolution, keeping the RMSE in predicted topography below 0.07 m throughout the simulation (black line in Fig. 4.7j), without a significant increase in compute

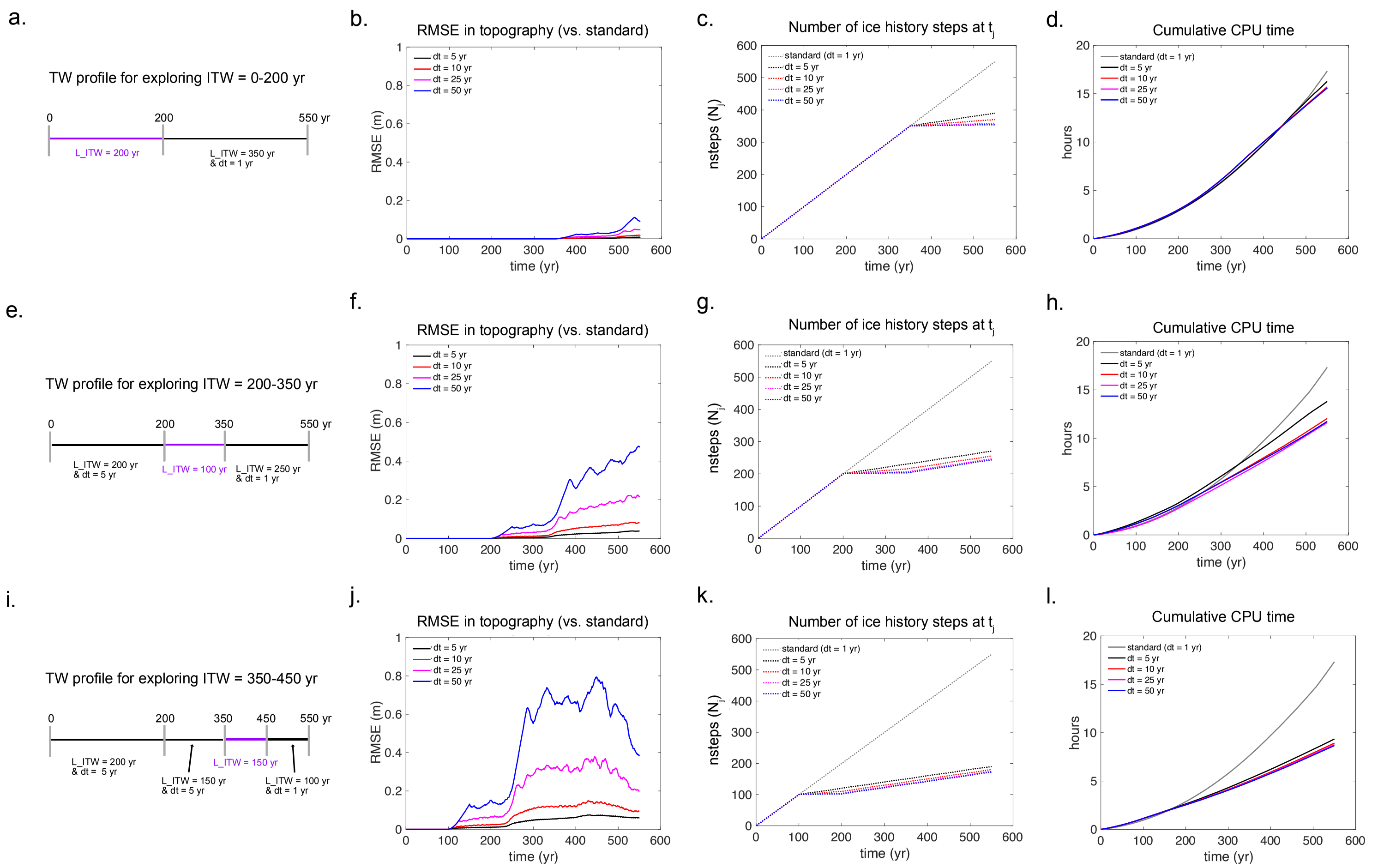

Figure 4.7: Time window profiles, RMSE in predicted topography, the number of loading events (nsteps, N_j) and the total CPU times in the 550 yr-long AIS-scenario simulations. Results from the simulations in which we explore the internal time windows that cover the periods between (a-d) 0-200 yr, (e-j) 200-350 yr and (i-l) 350-450 yr. Note that the standard simulation for the AIS scenario assigns a uniform time step size of 1 year throughout the simulation.

Figure 4.7

time and ice history steps compared to the other coarser simulations (Fig. 4.7k). The total computing time for the 5 yr simulation is $\sim$ 8.5 hr (Fig. 4.7l), which is a $\sim$ 50 % reduction from the computing time of the benchmark simulation ($\sim$ 17 hr) and only $\sim$ 3-6 % longer than the other simulations ($dt = 10$ yr, 25 yr and 50 yr). Thus, we arrive at an ideal time window profile (black line shown in Figs. 4.7j-l).

Having chosen the time window profile for the future AIS retreat scenario, we compare predicted topography from this time window simulation to that from the standard simulations that incorporate coarser uniform temporal resolution of 5 yr, 10 yr and 50 yr. Fig. 4.8 shows the snapshots ice thickness and predicted topography at model times 250 yr, 350 yr and 550 yr relative to 0 yr along a cross-section in Amundsen Sea Embayment across which the grounding line retreats during the simulations (shown by the red line in Fig. 4.6d). Figs. 4.8a-c indicate a rapid retreat of the marine-based West Antarctic Ice Sheet on a reverse-sloped bed between 250-550 yr and substantial bedrock uplift in response to the ice unloading. When the ice-sheet retreat and associated topography changes are small in the first 250 years of the simulation (see the solid blue and dotted blue lines in Fig. 4.8c), the differences in predicted topography from standard simulations with resolutions of 5-50 years (blue, red and magenta lines) compared to the benchmark 1 yr simulation reach up to 10 m. The spread of the differences increases even more as the retreat becomes more intense after 250 yr (see the changes in the differences from Fig. 4.8d to e). By 350 yr, after $\sim$330 km of grounding line retreat along the cross section (solid blue to dashed blue lines in Fig. 4.8b), the standard simulation that incorporates $dt = 50$ yr shows up to 80 m of difference in predicted topography compared to the benchmark simulation. The standard simulation that incorporates a relatively fine resolution of 5 yr still shows topographic differences in the grounding zone reaching a maximum of 5 m

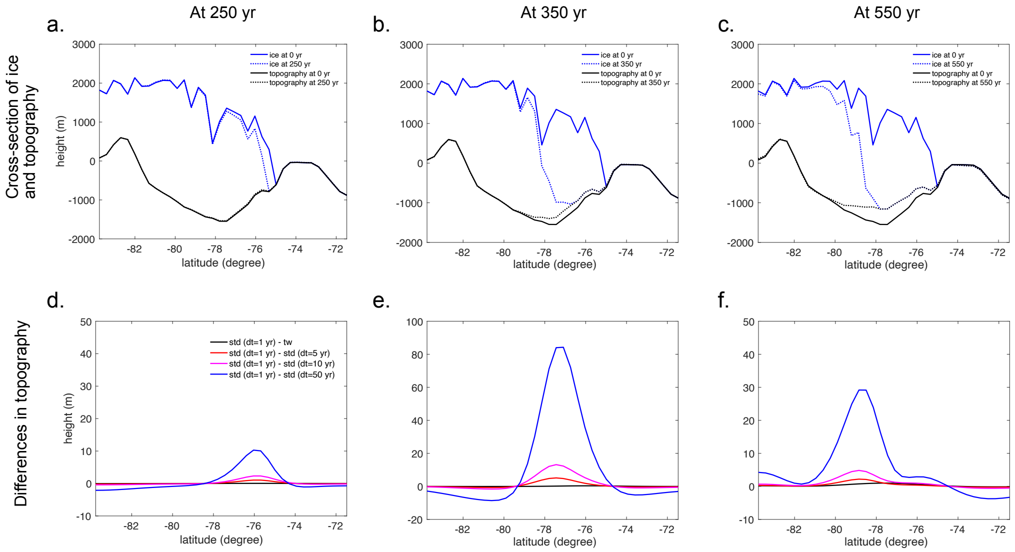

Figure 4.8: Elevations of the ice sheet and topography across the grounding line in the West Antarctic region and the sensitivity of predicted topography to temporal resolution in standard and time window simulations. (a-c) Ice surface (blue lines) and topography (black lines) predicted from the standard (std) simulation at (a) 250 yr (dashed lines), (b) 350 yr (dashed lines) and (c) 550 yr (dashed lines) relative to the initial simulation time 0 yr (solid lines). The cross-section of the grounding line is shown by a red line in Fig. 4.6d. (d-f) Differences in topography elevation at (d) 250 yr, (e) 350 yr and (f) 550 yr between the benchmark simulation ($dt = 1$ yr) and the i) time window simulation (black lines) that incorporates $dt = 1$ yr for the most recent 100 yr and $dt = 5$ yr for the rest of 450 yr of the simulation (i.e., black line in Fig. 4.7h), standard simulation with $dt = 5$ yr (red lines), $dt = 10$ yr (magenta lines), and $dt = 50$ yr (blue lines). Note the change in the y-axis in (e).

during the simulation (red line in Fig. 4.8e). Meanwhile the maximum difference in topography in the grounding zone in the simulation adopting the time window algorithm is less than 0.1 m by 350 yr and less than 1 m by 550 yr, or 0.24 % of the total deformation (up to 391 m by the end of the simulation).

To test the performance of the time window derived in Fig. 4.7, we incorporate it into a coupled Antarctic Ice Sheet - sea level simulation under RCP 8.5 climate forcing (as in the ice model used in Fig. 4.6; Deconto et al., 2021) and compare results to coupled simulations with a range of coupling time intervals and uniform time stepping in the ice history.

Figure 4.9 shows that Antarctic ice loss is over estimated when the standard algorithm with coupling intervals of dt=25 and 50 years is adopted, compared to a benchmark simulation with uniform dt=1 yr simulation. This is because a shorter coupling interval results in a stronger negative feedback of sea level on grounding line migration. The largest differences in ice thickness of 100s of meters occur near the grounding line in marine sectors of the West Antarctic where the sea level feedback is active (Fig. 4.9 c-d, g-h, k-l). In contrast, results from coupled simulations that incorporate the time window algorithm (i.e. that adopt a 1 yr coupling interval but non-uniform ice history in the sea level calculation) show minimal differences in ice thickness and volume relative to the benchmark simulation (Fig. 4.9 a, e, i, m). This is further highlighted shown in Fig. 4.10, which shows differences in ice thickness and topography between simulations along a cross-section across the grounding line (along the red line shown in Fig. 4.6d) of ice thickness and topography and their differences between coupled simulations. The grounding line retreat happens earlier when the coupling interval is longer (Fig. 4.10a-c), and differences in topography reach 14 m and 16 m by the end of the simulations with 25 and 50 yr coupling intervals, respectively, relative to the benchmark. (Fig. 4.10i). The simulation that incorporates the time window

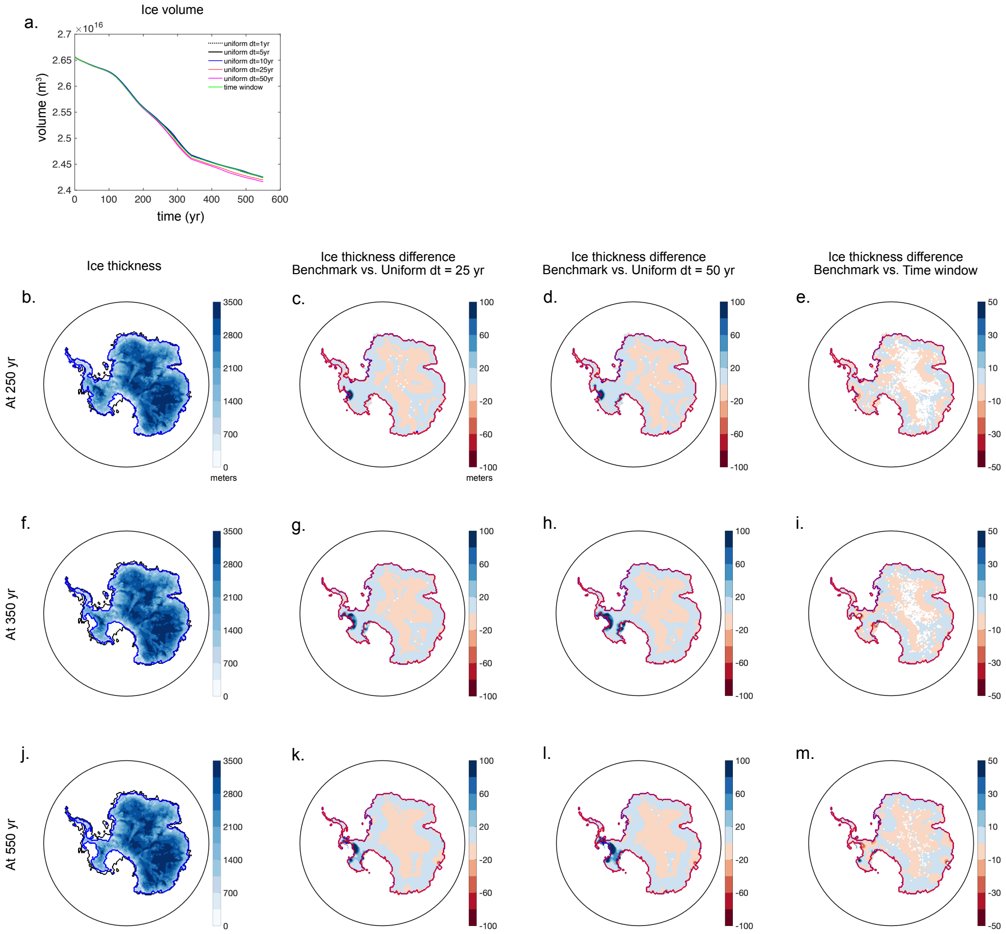

Figure 4.9: Changes in Antarctic Ice Sheet volume and thickness predicted from coupled ice sheet-sea level model projections over 550 years. (a) AIS volume variations through the next 550 years from simulations that incorporate uniform (standard) coupling interval of 1 yr (benchmark), 5, 10, 25 and 50 yr and that incorporate the time window profile derived in Fig. 4.7. (b, f, j) ice thickness modelled in the benchmark simulation, and differences in ice thickness between the benchmark and the standard simulations that incorporate coupling interval of (c, j, k) 25 yr and (d, h, l) 50 yr and that incorporates the time window profile (e, i, m). Each row shows results at a different timing at (b-e) 250 yr, (f-i) 350 yr and (j-m) 550 yr.

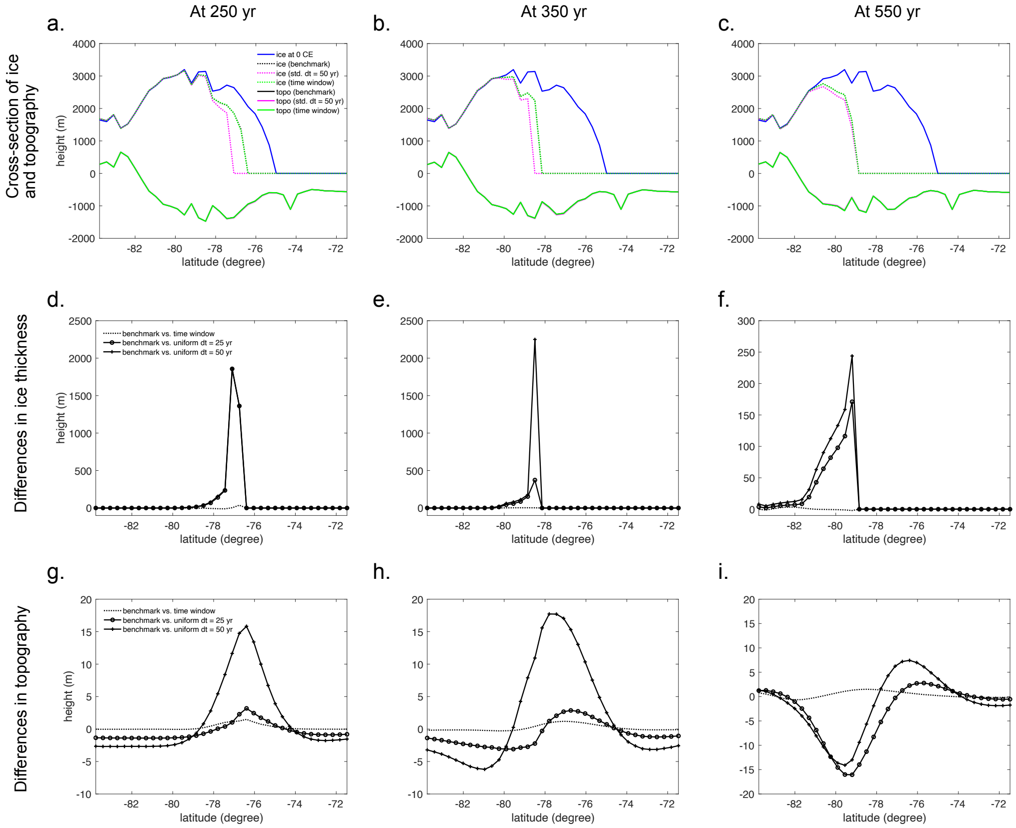

Figure 4.10: Topography and ice surface elevations in the Amundsen Sea Embayment as labeled by the red line in Fig. 4.6d and their sensitivity to temporal resolution. (a-c) cross section of ice thickness and topography at (a) 250 yr, (b) 350 yr and (c) 550 yr. (d-f) Differences in ice thickness between the benchmark coupled simulation at the indicated times (uniform dt = 1 yr) and the simulation incorporating the time window profile derived in Fig. 4.7 (dotted line), uniform dt = 25 yr (solid line with circles) and uniform dt 50 yr (solid line with crosses). (g-i) Same as (d-f) but showing differences in topography.

algorithm performs much better, with differences in ice thickness and topography compared to the benchmark simulation remaining below 2 m and 1.5 m, respectively, but with substantially reduced computation time (as indicated by Fig. 4.7l).

4.5 Discussion and Conclusions

We have developed a new time window algorithm that assigns nonuniform temporal resolution to the input ice cover changes in a forward sea-level model (Gomez et al., 2013), and restricts the linear increase in the number of ice history steps that a sea-level model has to consider at each time step. Our algorithm allows coupled ice-sheet-sea level models to capture short-term $O(\leq 10^2 \text{ yr})$ interactions between ice sheets, the solid Earth and sea level within simulations across a range of timescales. The algorithm improves computational feasibility while maintaining the precision of the sea-level (and thus coupled ice-sheet – sea-level) simulations.

In benchmarking the algorithm, we first tested the sensitivity of sea-level model outputs (i.e., predicted topography) to the temporal resolution adopted in idealized simulations (Fig. 4.2). Our results show that sea-level simulations with coarser temporal resolution do not accurately capture the timing and geometry of ice loading, and this leads to missing viscous signals and thus an underestimation of topography changes. We also found (as suggested in earlier literature, e.g., Peltier, 1974) that there is a stronger sensitivity to more recent loading, indicating that higher temporal resolution is required close to the current time step in a simulation. We then performed coupled ice-sheet – sea-level simulations through the last glacial cycle over the Northern Hemisphere with varying temporal resolution. Our results demonstrated that the underestimated magnitudes in predicted topography and infrequent topography updates in the coupled simulation with a lower-temporal resolution lead to smaller and sometimes unstable ice volume fluctuations (Fig. 4.3a). Our results also identify that 0.2 ky is the optimal coupling time interval for glacial-cycle simulations with broad spatial scale on a model of Earth structure representative of the global average Earth structure typically adopted in ice-age sea-level studies (e.g., Lambeck et al., 2014). When we utilize the time window algorithm and capture short-term, recent interactions while assigning coarser temporal resolution beyond the most recent 5 ky during the simulation, the NHIS dynamics through the last glacial cycle are captured well while saving the compute time by ~26-31 % (Figs. 4.3b-d).

After benchmarking the time window algorithm, we explored suitable time window parameters that improve computational efficiency while maintaining the precision of model outputs for two different sea-level model applications: A simulation of global ice-sheet evolution through two glacial cycles (Figs. 4.4-4.5); and a centennial-timescale future WAIS retreat scenario with an adopted Earth structure characteristic of the region with a thin lithosphere and low mantle viscosities (Figs. 4.6-4.10). The sample time window parameters we provide improve computational efficiency by ~54 % and ~50 % for each application, respectively, and the improvement would grow for longer simulations.

Overall, our results demonstrate that capturing short-term responses during a period including and temporally close to ongoing surface loading changes is important. At the same time, a coarser temporal resolution can be used for past loading changes. This is expected based on normal mode theory where the solid Earth signals comprised of normal modes with shorter decay times associated with the loading changes would have already relaxed out after simulations have proceeded (Peltier, 1974).

Previously, de Boer et al. (2014) developed what they call a “moving time window" algorithm in their coupled ice-sheet - sea-level model, which they applied to global ice sheets over four glacial cycles (410 ky). They utilized the characteristics of exponentially decaying viscous deformation and the linearity of 1-D Maxwell viscoelastic rheology and interpolated "future" bedrock deformation associated with ongoing surface loading changes at the current time step for a predefined length of "memory" of the solid Earth (they set the memory length to be 80 ky). Then, at every new time step, they calculated the total bedrock deformation associated with past loading changes by adding up the pre-interpolated bedrock deformation in the previous time steps. This algorithm allows them to perform global coupled simulations over multiple glacial cycles.

Rather than pre-calculating the future response as in deBoer et al. (2014), our time window recalls past ice loading changes in changing levels of detail as the simulation proceeds. In addition, our sea-level model with the time window is capable of iterative topography correction (as described in Kendall et al., 2005 and applied in a coupled context in Gomez et al., 2013) that allows for modelled present-day topography to converge to the observed present-day topography even when the model is coupled to a dynamic ice-sheet model. Considering that the topography correction is required in paleo glacial-cycle simulations in which initial topography is unknown and that the correction typically takes 2-3 additional iterations of the whole glacial-cycle simulation to achieve the convergence, the compute time saved by the time window algorithm becomes greater.

As for the coupling time interval, our results suggest that it should be at least 0.2 ky for glacial-cycle simulations, which is shorter than 1 ky suggested by deBoer et al. (2014) who claimed that 1 ky is a sufficiently short coupling interval for their glacial-cycle simulation. Our results indicate that a coupling time interval of 1 ky causes a significant difference of up to ~11.6 m of difference in the predicted sea-level equivalent Northern Hemispheric Ice Sheet volume compared to the simulation that incorporates the coupling time interval of 0.2 ky. In general, adopting a shorter coupling time comes at the expense of computational cost, and the choice of appropriate coupling time for a given application will depend on both the resolution and timescale of ice sheet variations and the adopted Earth structure model.

The sensitivity of a coupled ice-sheet – sea-level model to the coupling time interval depends on the Earth Structure. West Antarctica is underlain by low mantle viscosity (O $10^{18} - 10^{19}$ Pas; Barletta et al., 2018; Lloyd et al., 2020) and will respond viscously in a faster, more localized manner to surface loading changes, and this has the potential to have a significant impact on future evolution of marine ice in the region (Gomez et al., 2015). Furthermore, recent work by Larour et al. (2019) suggests that high spatial resolution and short time-stepping may be required to capture the elastic component of deformation in this region. This work together suggests that an annual to decadal scale coupling time is likely needed to capture the short-term interactions in a coupled model that may play a significant role in the stability of marine-based WAIS. In Section 4.4.3.2, we have performed a benchmark sea-level simulation with future WAIS evolution at 1 yr temporal resolution. We introduced a set of time window parameters that allows us to keep a coupling interval of 1 yr while improving the total CPU time by 50 % (Fig. 4.7) and maintaining the RMSE of predicted topography below 0.24 % across the grounding line in West Antarctica (Fig. 4.8). We have adopted the shortest temporal resolution suggested in the literature to date (Larour et al., 2019) for the benchmark sea-level simulation in our analysis, but given the complexity of Earth structure and ice dynamics in this region, further exploration with a coupled ice-sheet – sea-level model will be needed to rigorously assess the coupling time interval needed to simulate ice-sheet evolution in marine sectors of the AIS.

In this study, we have presented a new time window algorithm in a global sea-level model and provided sample time window parameters for applications to global glacial-cycle ice-sheet evolution and rapid marine ice sheet retreat in a region with weaker Earth structure. In addition to these applications, the time window algorithm has the potential to unlock opportunities to tackle a range of questions using coupled ice-sheet – sea-level modelling, such as evaluating shorelines during and since the warm mid-Pliocene (3 Ma; Raymo et al., 2011; Pollard et al., 2018), investigating the effects of short-term interactions between ice sheets, sea level and the solid Earth on the dynamics of the marine-based portion of Eurasian Ice Sheet during the last deglaciation phase (e. g., Petrini et al., 2020) and the associated impact on abrupt or episodic global sea-level events such as MWP-1A (e.g., Harrison et al., 2019) and understanding the dynamics of ice sheets during past warm interglacial periods (e. g., Clark et al., 2020). Finally, the improved computational feasibility with the time window could allow for ensemble simulations of coupled ice-sheet – sea-level dynamics for the future under different warming scenarios, which will provide useful insight into projected future sea-level hazard.

References

[1] An, M., D. A. Wiens, Y. Zhao, M. Feng, A. Nyblade, M. Kanao, Y. Li, A. Maggi, and J. J. Lévêque, Temperature, lithosphere-asthenosphere boundary, and heat flux beneath the Antarctic Plate inferred from seismic velocities, *Journal of Geophysical Research: Solid Earth*, *120*, 8720–8742, doi:10.1002/2015JB011917, 2015.

[2] Barletta, V. R., et al., Observed rapid bedrock uplift in amundsen sea embayment promotes ice-sheet stability, *Science*, *360*(6395), 1335–1339, doi: 10.1126/science.aao1447, 2018.

[3] Brendryen, J., H. Haflidason, Y. Yokoyama, K. A. Haaga, and B. Hannisdal, Eurasian Ice Sheet collapse was a major source of Meltwater Pulse 1A 14,600 years ago, *Nature Geoscience*, *13*, 363–368, doi:10.1038/s41561-020-0567-4, 2020.

[4] Clark, P. U., F. He, N. R. Golledge, J. X. Mitrovica, A. Dutton, J. S. Hoffman, and S. Dendy, Oceanic forcing of penultimate deglacial and last interglacial sea-level rise, *Nature*, *577*, 660–664, doi:10.1038/s41586-020-1931-7, 2020.

[5] Cuffey, K., and W. Paterson, *The physics of glaciers, 4th Edition*, 2010.

[6] De Boer, B., P. Stocchi, and R. S. Van De Wal, A fully coupled 3-D ice-sheet-sea-level model: Algorithm and applications, *Geoscientific Model Development*, *7*(5), 2141 – 2156, doi:10.5194/gmd-7-2141-2014, 2014.

[7] Deschamps, P., N. Durand, E. Bard, B. Hamelin, G. Camoin, A. L. Thomas, G. M. Henderson, J. Okuno, and Y. Yokoyama, Ice-sheet collapse and sea-level rise at the Bølling warming 14,600 years ago, *Nature*, *483*, 559–564, doi:10.1038/nature10902, 2012.

[8] Dziewonski, A. M., and D. L. Anderson, Preliminary reference Earth model, *Phys. Earth Planet. Inter*, *25*(4), 297–356, 1981.

[9] Fairbanks, R. G., A 17,000-year glacio-eustatic sea level record: Influence of glacial melting rates on the Younger Dryas event and deep-ocean circulation, *Nature*, *342*, 637–642, doi:10.1038/342637a0, 1989.

[10] Farrell, W. E., and J. A. Clark, On Postglacial Sea Level, *Geophysical Journal of the Royal Astronomical Society*, *46*, 64–667, doi:10.1111/j.1365-246X.1976.tb01252.x, 1976.

[11] Gomez, N., J. X. Mitrovica, P. Huybers, and P. U. Clark, Sea level as a stabilizing factor for marine-ice-sheet grounding lines, *Nature Geoscience*, *3*(12), 850–853, doi:10.1038/ngeo1012, 2010.

[12] Gomez, N., D. Pollard, J. X. Mitrovica, P. Huybers, and P. U. Clark, Evolution of a coupled marine ice sheet-sea level model, *Journal of Geophysical Research: Earth Surface*, *117*(1), 1–9, doi:10.1029/2011JF002128, 2012.

[13] Gomez, N., D. Pollard, and J. X. Mitrovica, A 3-D coupled ice sheet - sea level model applied to Antarctica through the last 40 ky, *Earth and Planetary Science Letters*, *384*, 88–99, doi:10.1016/j.epsl.2013.09.042, 2013.

[14] Gomez, N., D. Pollard, and D. Holland, Sea-level feedback lowers projections of future Antarctic Ice-Sheet mass loss, *Nature Communications*, *6*, 8798, doi:10.1038/ncomms9798, 2015.

[15] Gomez, N., K. Latychev, and D. Pollard, A coupled ice sheet-sea level model incorporating 3D earth structure: Variations in Antarctica during the Last Deglacial Retreat, *Journal of Climate*, *31*, 4041–4054, doi: 10.1175/JCLI-D-17-0352.1, 2018.

[16] Gomez, N., M. E. Weber, P. U. Clark, J. X. Mitrovica, and H. K. Han, Antarctic ice dynamics amplified by Northern Hemisphere sea-level forcing, *Nature*, *587*(7835), 600–604, doi:10.1038/s41586-020-2916-2, 2020.

[17] Gowan, E. J., et al., A new global ice sheet reconstruction for the past 80 000 years, *Nature Communications*, *12*, 1199, doi:10.1038/s41467-021-21469-w, 2021.

[18] Han, H. K., and N. Gomez, The impact of water loading on postglacial decay times in Hudson Bay, *Earth and Planetary Science Letters*, *489*, 156–165, doi:10.1016/j.epsl.2018.02.043, 2018.

[19] Han, H. K., N. Gomez, D. Pollard, and R. DeConto, Modeling Northern Hemispheric ice sheet dynamics, sea level change and solid Earth deformation through the last glacial cycle, *Journal of Geophysical Research: Earth Surface*, doi:10.1029/2020jf006040, 2021.

[20] Harrison, S., D. E. Smith, and N. F. Glasser, Late Quaternary meltwater pulses and sea level change, *Journal of Quaternary Science*, *34*, 1–15, doi: 10.1002/jqs.3070, 2019.

[21] Kendall, R. A., J. X. Mitrovica, and G. A. Milne, On post-glacial sea level - II. Numerical formulation and comparative results on spherically symmetric

models, *Geophysical Journal International*, *161*(3), 679–706, doi:10.1111/j.1365-246X.2005.02553.x, 2005.

[22] Khan, N. S., et al., Inception of a global atlas of sea levels since the Last Glacial Maximum, *Quaternary Science Reviews*, *220*, 359–371, doi:10.1016/j.quascirev.2019.07.016, 2019.

[23] Konrad, H., I. Sasgen, D. Pollard, and V. Klemann, Potential of the solid-Earth response for limiting long-term West Antarctic Ice Sheet retreat in a warming climate, *Earth and Planetary Science Letters*, *432*, 254–264, doi:10.1016/j.epsl.2015.10.008, 2015.

[24] Lambeck, K., H. Rouby, A. Purcell, Y. Sun, and M. Sambridge, Sea level and global ice volumes from the Last Glacial Maximum to the Holocene, *Proceedings of the National Academy of Sciences of the United States of America*, *111*, 15,296–15,303, doi:10.1073/pnas.1411762111, 2014.

[25] Larour, E., H. Seroussi, S. Adhikari, E. Ivins, L. Caron, M. Morlighem, and N. Schlegel, Slowdown in Antarctic mass loss from solid Earth and sea-level feedbacks, *Science*, *364*(6444), eaav7908, doi:10.1126/science.aav7908, 2019.

[26] Lloyd, A. J., et al., Seismic Structure of the Antarctic Upper Mantle Imaged with Adjoint Tomography, *Journal of Geophysical Research: Solid Earth*, *125*(3), doi:10.1029/2019JB017823, 2020.

[27] Mitrovica, J. X., and G. A. Milne, On post-glacial sea level: I. General theory, *Geophysical Journal International*, *154*(2), 253–267, doi:10.1046/j.1365-246X.2003.01942.x, 2003.

[28] Mitrovica, J. X., J. Wahr, I. Matsuyama, and A. Paulson, The rotational

stability of an ice-age earth, *Geophysical Journal International*, *161*(2), 491–506, doi:10.1111/j.1365-246X.2005.02609.x, 2005.

[29] Morelli, A., and S. Danesi, Seismological imaging of the Antarctic continental lithosphere: A review, *Global and Planetary Change*, *42*(1-4), 155–165, doi:10.1016/j.gloplacha.2003.12.005, 2004.

[30] Nield, G. A., V. R. Barletta, A. Bordoni, M. A. King, P. L. Whitehouse, P. J. Clarke, E. Domack, T. A. Scambos, and E. Berthier, Rapid bedrock uplift in the Antarctic Peninsula explained by viscoelastic response to recent ice unloading, *Earth and Planetary Science Letters*, *397*, 32–41, doi:10.1016/j.epsl.2014.04.019, 2014.

[31] Peltier, W. R., The impulse response of a Maxwell Earth, *Reviews of Geophysics*, *12*(4), 649–669, doi:10.1029/RG012i004p00649, 1974.

[32] Peltier, W. R., Global glacial isostasy and the surface of the ice-age earth: The ICE-5G (VM2) model and GRACE, *Annual Review of Earth and Planetary Sciences*, *32*, 111–149, doi:10.1146/annurev.earth.32.082503.144359, 2004.

[33] Petrini, M., et al., Simulated last deglaciation of the Barents Sea Ice Sheet primarily driven by oceanic conditions, *Quaternary Science Reviews*, *238*(15), 106,314, doi:10.1016/j.quascirev.2020.106314, 2020.

[34] Pollard, D., and R. M. Deconto, Description of a hybrid ice sheet-shelf model, and application to Antarctica, *Geoscientific Model Development*, *5*, 1273–1295, doi:10.5194/gmd-5-1273-2012, 2012.

[35] Pollard, D., R. M. DeConto, and R. B. Alley, Potential Antarctic Ice Sheet retreat driven by hydrofracturing and ice cliff failure, *Earth and Planetary Science Letters*, *412*(112), 121, doi:10.1016/j.epsl.2014.12.035, 2015.

[36] Pollard, D., N. Gomez, and R. M. Deconto, Variations of the Antarctic Ice Sheet in a coupled ice sheet-Earth-sea level model: Sensitivity to viscoelastic Earth properties, *Journal of Geophysical Research: Earth Surface*, *122*, 2124–2138, doi:10.1002/2017JF004371, 2017.

[37] Pollard, D., N. Gomez, R. M. DeConto, and H. K. Han, Estimating Modern Elevations of Pliocene Shorelines Using a Coupled Ice Sheet-Earth-Sea Level Model, *Journal of Geophysical Research: Earth Surface*, *123*(9), 2279–2291, doi:10.1029/2018JF004745, 2018.

[38] Pörtner, H.-O., et al., IPCC Special Report on the Ocean and Cryosphere in a Changing Climate, *eds*, 2019.

[39] Powell, E., N. Gomez, C. Hay, K. Latychev, and J. X. Mitrovica, Viscous effects in the solid earth response to modern Antarctic ice mass flux: Implications for geodetic studies of WAIS stability in a warming world, *Journal of Climate*, pp. 443–459, doi:10.1175/JCLI-D-19-0479.1, 2020.

[40] Raymo, M. E., J. X. Mitrovica, M. J. O'Leary, R. M. Deconto, and P. J. Hearty, Departures from eustasy in Pliocene sea-level records, *Nature Geoscience*, *4*(5), 328–332, doi:10.1038/ngeo1118, 2011.

[41] Rovere, A., M. Pappalardo, S. Richiano, M. Aguirre, M. R. Sandstrom, P. J. Hearty, J. Austermann, I. Castellanos, and M. E. Raymo, Higher than present global mean sea level recorded by an Early Pliocene intertidal unit in Patagonia (Argentina), *Communications Earth & Environment*, *1*(68), doi:10.1038/s43247-020-00067-6, 2020.

[42] Schoof, C., Ice sheet grounding line dynamics: Steady states, stability, and hysteresis, *Journal of Geophysical Research: Earth Surface*, *112*(F3), doi:10.1029/2006JF000664, 2007.

[43] Spada, G., and P. Stocchi, SELEN: A Fortran 90 program for solving the "sea-level equation", *Computers and Geosciences*, *33*(4), 538–562, doi:10.1016/j.cageo.2006.08.006, 2007.

[44] Thomas, R. H., and C. R. Bentley, A model for Holocene retreat of the West Antarctic Ice Sheet, *Quaternary Research*, *10*(2), 150–170, doi:10.1016/0033-5894(78)90098-4, 1978.

[45] Weber, M. E., et al., Millennial-scale variability in Antarctic ice-sheet discharge during the last deglaciation, *Nature*, *334*, 1265–1269, doi:10.1038/nature13397, 2014.

[46] Weertman, J., Stability of the junction of an ice sheet and an ice shelf, *Journal of Glaciology*, *13*, 3–11, doi:10.3189/s0022143000023327, 1974.

[47] Woodward, R. S., On the Form and Position of the Sea-level as Dependent on Superficial Masses Symmetrically Disposed with Respect to a Radius of the Earth's Surface, *United States Geol. Survey Bull.*, *48*, 87–170, doi:10.2307/1967175, 1888.

Chapter 5

Discussion and Conclusions

Ice sheets interact with the solid Earth and sea level and evolve over a range of timescales. Studying how these components in the Earth System impacted each other through past glacial cycles and capturing such interactions in models can help us better understand our present and project future sea-level changes.

In this thesis, I have conducted three studies (Ch. 2-4) to broaden our understanding of and our ability to numerically simulate ice-age sea-level changes and the interactions between ice sheets, sea level and the solid Earth on a range of timescales. In particular, I sought out to explore the following questions:

Q1. (Chapter 2) What was the unidirectional influence of ice the (unidirectional) influence of ice cover changes on GIA predictions in North America during the last deglaciation? More specifically, how did sea level change in North America in response to surface (ice and water) loading changes during the last deglaciation phase? How do post-deglaciation GIA signals influence the interpretation of geological sea-level records that are used to constrain mantle viscosity in the Hudson Bay region of North America?

Q2. (Chapter 3) What was the two-way influence between ice sheet dynamics and GIA in the Northern Hemisphere through the last glacial cycle? How did the terrestrial and marine-based ice sheets in the Northern Hemisphere interact with the solid Earth and sea level during the last glacial cycle? What were the separate roles of solid earth deformation and gravitational-field perturbations on the short-term $O(\leq 10^2\text{ yr})$ and long-term $O(> 10^2\text{ yr})$ dynamics of the Northern Hemispheric Ice Sheets?

Q3. (Chapter 4) How do we improve sea-level modelling so that a coupled ice-sheet - sea-level model can capture the short-term interactions between ice sheets, sea level and the solid Earth within simulations with a large number of ice history time steps (e.g., longer glacial-cycle timescale simulations or Antarctic Ice Sheet simulations that require annual to decadal coupling time interval between an ice-sheet model and a sea-level model)?

Ice-cover changes in the past caused sea-level changes over an ice-age timescale because of the viscoelastic Structure of the solid Earth. Postglacial decay times (the intrinsic timescale of the solid Earth relaxation toward isostatic equilibrium) observed in the Hudson Bay region in North America have been used to infer the Earth's mantle viscosity. The use of postglacial decay times in constraining mantle viscosity assumes that 1) these parameters are insensitive to ice loading history, 2) the region of inference was once under the centre of the paleo ice sheet and 3) there is no ongoing surface (ice or ocean) loading change at the time of inference. However, there have been ongoing water loading changes in Hudson Bay after the last deglaciation phase that could impart potential bias in interpreting observed postglacial decay times and thus the inference of mantle viscosity.

In Chapter 2, I investigated this issue by modelling postglacial sea-level changes associated with ice and water loading changes separately since the Last Glacial Maximum (21 ka) and calculating postglacial decay times based on each sea-level curve. Our results suggest that postglacial decay times at sites in the Hudson Bay region in North America can be biased by recent (late Holocene) ice unloading and ongoing water loading in the bay, suggesting caution in interpreting these records. Our results also demonstrate that bias can arise if the time window used in estimating postglacial decay times covers periods close to active ice and water loading during the deglaciation followed by post-deglacial water redistribution in Hudson Bay. These findings have been supported by more recent work by Kuchar et al. (2020), who performed a detailed sensitivity test of postglacial decay times to different ice histories. They confirmed that postglacial decay times are sensitive to ice loading history and showed that the sensitivity depends on a site's location relative to the geometry of an ice sheet covering the region. They also concur with our findings that postglacial decay times may not always be appropriate to constrain Earth structure, but add that Richmond Gulf in Hudson Bay is less biased by Holocene water loading changes and insensitive to ice history, making the site suitable for decay time analyses (e.g., Mitrovica and Forte, 2004; Lau et al., 2016).

Chapter 2 highlights that it is important to capture the full details of surface (ice and water) loading and associated GIA to interpret records of paleo sea-level change and understand the driving mechanisms. In Chapter 3, I carried this idea forward to investigate how GIA impacts our understanding of the evolution of paleo ice sheets. I modelled the coupled evolution of the Northern Hemispheric Ice Sheets and GIA over the last glacial cycle and investigated the influence of Earth deformation and gravitational perturbations on ice dynamics. Our results show that solid Earth deformation enhanced the evolution of the NHIS through build-up and retreat phases through ice-surface elevation feedback mechanism over the glacial cycle. I also found that the sea-level feedback influenced the short-term $O(\leq 10^2\ \mathrm{yr})$ dynamics of the marine-based portion of the Laurentide and Eurasian Ice Sheets during the last deglaciation phase. For example, a local sea-level fall due to local deglaciation caused short-lasting stabilization of the Barents-Kara Ice

Sheet before the ice sheet rapidly collapsed within a few centuries rather than the earlier and gradual retreat seen in the case of absence of the sea-level feedback.

These results hint at the mechanism driving the Eurasian Ice Sheet's dynamics and its contribution to sea level during Melt Water Pulse-1A (MWP-1A), a rapid global sea level rise of ∼15 m in ∼350 years that occurred around ∼14.6 ka (Fairbanks, 1989; Hanebuth et al., 2000; Deschamps et al., 2012; Liu et al. 2015). Brendryen et al. (2020) have recently suggested a contribution of ∼3.3-6.7 m of global mean sea-level rise from the rapid collapse of the Eurasian Ice Sheet Complex during MWP-1A, ∼2.5-5 m larger than previously suggested (e.g., Hughes et al., 2016; Patton et al., 2017). Our results suggest that a rapid collapse of the marine-based Barents-Kara Sea Ice Sheet of the Eurasian Ice Sheet might have followed a temporary stabilization due to sea-level feedback, and future work will investigate this possibility in more detail. Understanding the mechanisms and timing of rapid marine ice-sheet retreat such as this in the past could provide insights into the processes of the past and potential future of the WAIS, which has a possibility of taking a similar path to a catastrophic collapse within only 300-500 years.

In a broader context, our results indicate that the feedback between ice sheet dynamics and GIA are active over a range of timescales, emphasizing the importance of capturing the interactions at high temporal resolution and simultaneously presenting a computational challenge in classic coupled ice-sheet – sea-level modelling. To capture such short-term interactions between ice sheets, sea level and the solid earth in coupled ice-sheet - sea-level simulations, a dynamic ice-sheet model and sea-level model need to exchange their outputs frequently. However, keeping a short coupling time interval in coupled simulations becomes computationally challenging with the increasing length of the simulations. To overcome this computational challenge, I have developed a new "time window" algorithm in the sea-level model. The algorithm allows the assignment of a non-uniform temporal resolution in the model, enabling ice sheet-GIA feedback at high temporal resolution for a recent loading period while having a coarser temporal resolution to "forget" some details of loading that happened further back in time. This allows the feedback between ice sheets and GIA to be captured precisely in coupled simulations while remaining computationally feasible for simulations with many time steps. I also provided in the chapter the time window parameters that can be used to simulate the global ice evolution over the past two glacial cycles and the multi-centennial future Antarctic Ice Sheet evolution, each of which reduced computing time by 54 % and 50 %, respectively, compared to the classic sea-level algorithm.

Potential applications of the algorithm include investigating the role of GIA feedback on episodic changes in past ice sheets and sea levels, such as meltwater pulse events as mentioned above and Heinrich events (e.g., Bassis et al., 2017). The algorithm can also be applied to evaluate ice-Earth-sea level feedbacks during past warm interglacials (Raymo et al., 2011; Pollard et al., 2018) and future Antarctic Ice Sheet dynamics that require annual to decadal-scale coupling time intervals or less, as suggested by some recent studies (Barletta et al., 2018; Larour et al. 2019).

A list of shortcomings of the studies in this thesis includes the following: relatively simple representation of the paleoclimate forcing, absence of error bars in model results, uncertain climate forcing and ice model parameters (e.g., basal sliding coefficients), simplified representation (e.g., sub-ice ocean melting) or absence of explicit physics (e.g., basal hydrology) in some parts of the ice-sheet model, and incorporation of radially varying (1D) rather than 3D Earth structure in the sea-level model. However, these limitations are not specific to this thesis but are ongoing subjects of improvement in the ice sheet and sea-level modelling communities in general. These shortcomings made it challenging for me to match our model results to paleo constraints on the volume and extent of the Northern Hemisphere Ice Sheets during the last glacial cycle on a regional scale, even within the wide parameter space I explored. Therefore, I focused on studying the physics of the interactions within a wide range of ice-sheet model and climate forcing parameters rather than comparing our model outputs to site-specific ice-sheet and sea-level data. Future work could explore these interactions on a regional scale at higher resolution and could improve on the representation processes at the ice-bed, ice-atmosphere and ice-ocean interfaces and compare to regional observational constraints. Meanwhile, the time window algorithm and associated improvement in computational feasibility will enable me to perform ensemble simulations and explore a range of possible ice-sheet – sea-level dynamics under different climate forcing, ice model parameters and Earth models. Ensemble simulations will help to improve our understanding and quantify uncertainty of both past (e.g., Tarasov et al., 2012) and future (e.g., DeConto et al., 2021) ice sheet – sea level – solid Earth interactions.

Through this thesis, I have contributed to expanding the understanding of the interactions between ice sheets and GIA over broader spatial and temporal scales focusing on Earth's past. To date, much paleo research has been conducted in compiling paleoenvironmental datasets and modelling past long-term climate, and much effort has also been going on in projecting future ice sheets and sea level. However, most paleo and future studies have been done fairly independently, and not much work has been done to bridge the two. My vision for the field is to start using paleo research more in constraining and projecting future climate change. Connecting the paleo and future research communities will increase the fields' interdisciplinarity and the robustness of the future projections, contributing to both the scientific community and society. In this regard, I hope that my thesis will contribute to constructing a window through which we can bridge Earth's past and future climate, helping us to prepare for the future of our warming planet.

References

[1] Albrecht, T., R. Winkelmann, and A. Levermann, Glacial-cycle simulations of the Antarctic Ice Sheet with the Parallel Ice Sheet Model (PISM)-Part 2: Parameter ensemble analysis, *Cryosphere*, (14), 633–656, doi:10.5194/tc-14-633-2020, 2020.

[2] Austermann, J., J. X. Mitrovica, K. Latychev, and G. A. Milne, Barbados-based estimate of ice volume at Last Glacial Maximum affected by subducted plate, *Nature Geoscience*, *6*, 553–557, doi:10.1038/ngeo1859, 2013.

[3] Barletta, V. R., et al., Observed rapid bedrock uplift in amundsen sea embayment promotes ice-sheet stability, *Science*, *360*(6395), 1335–1339, doi:10.1126/science.aao1447, 2018.

[4] Bassis, J. N., S. V. Petersen, and L. Mac Cathles, Heinrich events triggered by ocean forcing and modulated by isostatic adjustment, *Nature*, *542*(7641), 332–334, doi:10.1038/nature21069, 2017.

[5] Brendryen, J., H. Haflidason, Y. Yokoyama, K. A. Haaga, and B. Hannisdal, Eurasian Ice Sheet collapse was a major source of Meltwater Pulse 1A 14,600 years ago, *Nature Geoscience*, *13*, 363–368, doi:10.1038/s41561-020-0567-4, 2020.

[6] Clark, P. U., A. S. Dyke, J. D. Shakun, A. E. Carlson, J. Clark, B. Wohlfarth,

J. X. Mitrovica, S. W. Hostetler, and A. M. McCabe, The Last Glacial Maximum, *Science*, *325*(5941), 710–714, doi:10.1126/science.1172873, 2009.

[7] Coulson, S., T. Pico, J. Austermann, E. Powell, R. Moucha, and J. X. Mitrovica, The role of isostatic adjustment and gravitational effects on the dynamics of the Messinian salinity crisis, *Earth and Planetary Science Letters*, *525*, 115,760, doi:10.1016/j.epsl.2019.115760, 2019.

[8] De Boer, B., P. Stocchi, and R. S. Van De Wal, A fully coupled 3-D ice-sheet-sea-level model: Algorithm and applications, *Geoscientific Model Development*, *7*, 2141–2156, doi:10.5194/gmd-7-2141-2014, 2014.

[9] DeConto, R., The Paris Climate Agreement and future sea level rise from Antarctica, *Nature*, 2021.

[10] DeConto, R. M., and D. Pollard, Contribution of Antarctica to past and future sea-level rise, *Nature*, *531*(7596), 591–597, doi:10.1038/nature17145, 2016.

[11] Deschamps, P., N. Durand, E. Bard, B. Hamelin, G. Camoin, A. L. Thomas, G. M. Henderson, J. Okuno, and Y. Yokoyama, Ice-sheet collapse and sea-level rise at the Bølling warming 14,600 years ago, *Nature*, *483*, 559–564, doi:10.1038/nature10902, 2012.

[12] Fairbanks, R. G., A 17,000-year glacio-eustatic sea level record: Influence of glacial melting rates on the Younger Dryas event and deep-ocean circulation, *Nature*, *342*, 637–642, doi:10.1038/342637a0, 1989.

[13] Gilford, D. M., E. L. Ashe, R. M. DeConto, R. E. Kopp, D. Pollard, and A. Rovere, Could the Last Interglacial Constrain Projections of Future

Antarctic Ice Mass Loss and Sea-Level Rise?, *Journal of Geophysical Research: Earth Surface*, *125*(10), e2019JF005,418, doi:10.1029/2019JF005418, 2020.

[14] Gomez, N., J. X. Mitrovica, P. Huybers, and P. U. Clark, Sea level as a stabilizing factor for marine-ice-sheet grounding lines, *Nature Geoscience*, *3*(12), 850–853, doi:10.1038/ngeo1012, 2010.

[15] Gomez, N., D. Pollard, J. X. Mitrovica, P. Huybers, and P. U. Clark, Evolution of a coupled marine ice sheet-sea level model, *Journal of Geophysical Research: Earth Surface*, *117*(1), 1–9, doi:10.1029/2011JF002128, 2012.

[16] Gomez, N., D. Pollard, and J. X. Mitrovica, A 3-D coupled ice sheet - sea level model applied to Antarctica through the last 40 ky, *Earth and Planetary Science Letters*, *384*, 88–99, doi:10.1016/j.epsl.2013.09.042, 2013.

[17] Gomez, N., D. Pollard, and D. Holland, Sea-level feedback lowers projections of future Antarctic Ice-Sheet mass loss, *Nature Communications*, *6*, 8798, doi:10.1038/ncomms9798, 2015.

[18] Gomez, N., K. Latychev, and D. Pollard, A coupled ice sheet-sea level model incorporating 3D earth structure: Variations in Antarctica during the Last Deglacial Retreat, *Journal of Climate*, *31*, 4041–4054, doi: 10.1175/JCLI-D-17-0352.1, 2018.

[19] Gomez, N., M. E. Weber, P. U. Clark, J. X. Mitrovica, and H. K. Han, Antarctic ice dynamics amplified by Northern Hemisphere sea-level forcing, *Nature*, *587*(7835), 600–604, doi:10.1038/s41586-020-2916-2, 2020.

[20] Gregory, J. M., et al., Concepts and Terminology for Sea Level: Mean, Variability and Change, Both Local and Global, *Surveys in Geophysics*, *40*(6), 1251–1289, doi:10.1007/s10712-019-09525-z, 2019.

[21] Han, H. K., N. Gomez, D. Pollard, and R. DeConto, Modeling Northern Hemispheric ice sheet dynamics, sea level change and solid Earth deformation through the last glacial cycle, *Journal of Geophysical Research: Earth Surface*, doi:10.1029/2020jf006040, 2021.

[22] Hanebuth, T., K. Stattegger, and P. M. Grootes, Rapid flooding of the Sunda Shelf: A late-glacial sea-level record, *Science*, *288*(5468), 1033–1035, doi:10.1126/science.288.5468.1033, 2000.

[23] Hay, C. C., H. C. Lau, N. Gomez, J. Austermann, E. Powell, J. X. Mitrovica, K. Latychev, and D. A. Wiens, Sea level fingerprints in a region of complex earth structure: The case of WAIS, *Journal of Climate*, pp. 1881–1892, doi:10.1175/JCLI-D-16-0388.1, 2017.

[24] Hughes, A. L., R. Gyllencreutz, Ø. S. Lohne, J. Mangerud, and J. I. Svendsen, The last Eurasian ice sheets - a chronological database and time-slice reconstruction, DATED-1, *Boreas*, *45*, 1–45, doi:10.1111/bor.12142, 2016.

[25] Kendall, R. A., J. X. Mitrovica, and G. A. Milne, On post-glacial sea level - II. Numerical formulation and comparative results on spherically symmetric models, *Geophysical Journal International*, *161*(3), 679–706, doi:10.1111/j.1365-246X.2005.02553.x, 2005.

[26] Kuchar, J., G. Milne, A. Hill, L. Tarasov, and M. Nordman, An investigation into the sensitivity of postglacial decay times to uncertainty in the adopted ice history, *Geophysical Journal International*, *220*(2), 1172–1186, doi:10.1093/gji/ggz512, 2020.

[27] Lambeck, K., H. Rouby, A. Purcell, Y. Sun, and M. Sambridge, Sea level and global ice volumes from the Last Glacial Maximum to the Holocene,

Proceedings of the National Academy of Sciences of the United States of America, *111*, 15,296–15,303, doi:10.1073/pnas.1411762111, 2014.

[28] Lambeck, K., A. Purcell, and S. Zhao, The North American Late Wisconsin ice sheet and mantle viscosity from glacial rebound analyses, *Quaternary Science Reviews*, (158), 172–210, doi:10.1016/j.quascirev.2016.11.033, 2017.

[29] Larour, E., H. Seroussi, S. Adhikari, E. Ivins, L. Caron, M. Morlighem, and N. Schlegel, Slowdown in Antarctic mass loss from solid Earth and sea-level feedbacks, *Science*, *364*(6444), eaav7908, doi:10.1126/science.aav7908, 2019.

[30] Latychev, K., J. X. Mitrovica, J. Tromp, M. E. Tamisiea, D. Komatitsch, and C. C. Christara, Glacial isostatic adjustment on 3-D earth models: A finite-volume formulation, *Geophysical Journal International*, *161*(2), 421–444, doi:10.1111/j.1365-246X.2005.02536.x, 2005.

[31] Lau, H. C., J. X. Mitrovica, J. Austermann, O. Crawford, D. Al-Attar, and K. Latychev, Inferences of mantle viscosity based on ice age data sets: Radial structure, *Journal of Geophysical Research: Solid Earth*, *121*, 6991–7012, doi:10.1002/2016JB013043, 2016.

[32] Liu, J., G. A. Milne, R. E. Kopp, P. U. Clark, and I. Shennan, Sea-level constraints on the amplitude and source distribution of Meltwater Pulse 1A, *Nature Geoscience*, *9*, 130–134, doi:10.1038/ngeo2616, 2016.

[33] Milne, G. A., and J. X. Mitrovica, Postglacial sea-level change on a rotating Earth: First results from a gravitationally self-consistent sea-level equation, *Geophysical Journal International*, *126*(3), F13–F20, doi:10.1111/j.1365-246X.1996.tb04691.x, 1996.

[34] Milne, G. A., and J. X. Mitrovica, The influence of time-dependent ocean-continent geometry on predictions of Post-Glacial sea level change in Australia and New Zealand, *Geophysical Research Letters*, *25*(6), 793–796, doi: 10.1029/98GL00498, 1998.

[35] Mine, G. A., and J. X. Mitrovica, Postglacial sea-level change on a rotating Earth, *Geophysical Journal International*, *133*(1), 1–19, doi:10.1046/j.1365-246x.1998.1331455.x, 1998.

[36] Mitrovica, J. X., and A. M. Forte, A new inference of mantle viscosity based upon joint inversion of convection and glacial isostatic adjustment data, *Earth and Planetary Science Letters*, *225*(1–2), 177–189, doi: 10.1016/j.epsl.2004.06.005, 2004.

[37] Mitrovica, J. X., and G. A. Milne, On post-glacial sea level: I. General theory, *Geophysical Journal International*, *154*, 253–267, doi:10.1046/j.1365-246X.2003.01942.x, 2003.

[38] Mitrovica, J. X., G. A. Milne, and J. L. Davis, Glacial isostatic adjustment on a rotating earth, *Geophysical Journal International*, *147*, 562–578, doi: 10.1046/j.1365-246x.2001.01550.x, 2001.

[39] Morlighem, M., et al., BedMachine v3: Complete Bed Topography and Ocean Bathymetry Mapping of Greenland From Multibeam Echo Sounding Combined With Mass Conservation, *Geophysical Research Letters*, *44*(21), 11,051–11,061, doi:10.1002/2017GL074954, 2017.

[40] Morlighem, M., et al., Deep glacial troughs and stabilizing ridges unveiled beneath the margins of the Antarctic ice sheet, *Nature Geoscience*, *13*, 132–137, doi:10.1038/s41561-019-0510-8, 2020.

[41] Nield, G. A., P. L. Whitehouse, W. van der Wal, B. Blank, J. P. O'Donnell, and G. W. Stuart, The impact of lateral variations in lithospheric thickness on glacial isostatic adjustment in West Antarctica, *Geophysical Journal International*, *214*(2), 811–824, doi:10.1093/gji/ggy158, 2018.

[42] Patton, H., et al., Deglaciation of the Eurasian ice sheet complex, *Quaternary Science Reviews*, *169*, 148–172, doi:10.1016/j.quascirev.2017.05.019, 2017.

[43] Peltier, W. R., The impulse response of a Maxwell Earth, *Reviews of Geophysics*, *12*(4), 649–669, doi:10.1029/RG012i004p00649, 1974.

[44] Peltier, W. R., Global glacial isostasy and the surface of the ice-age earth: The ICE-5G (VM2) model and GRACE, *Annual Review of Earth and Planetary Sciences*, *32*, 111–149, doi:10.1146/annurev.earth.32.082503.144359, 2004.

[45] Pico, T., J. R. Creveling, and J. X. Mitrovica, Sea-level records from the U.S. mid-Atlantic constrain Laurentide Ice Sheet extent during Marine Isotope Stage 3, *Nature Communications*, *8*, 15,612, doi:10.1038/ncomms15612, 2017.

[46] Pollard, D., and R. M. Deconto, Description of a hybrid ice sheet-shelf model, and application to Antarctica, *Geoscientific Model Development*, *5*, 1273–1295, doi:10.5194/gmd-5-1273-2012, 2012.

[47] Pollard, D., N. Gomez, R. M. DeConto, and H. K. Han, Estimating Modern Elevations of Pliocene Shorelines Using a Coupled Ice Sheet-Earth-Sea Level Model, *Journal of Geophysical Research: Earth Surface*, *123*(9), 2279–2291, doi:10.1029/2018JF004745, 2018.

[48] Pörtner, H.-O., et al., IPCC Special Report on the Ocean and Cryosphere in a Changing Climate, *Tech. rep.*, 2019.

[49] Raymo, M. E., J. X. Mitrovica, M. J. O'Leary, R. M. Deconto, and P. J. Hearty, Departures from eustasy in Pliocene sea-level records, *Nature Geoscience*, *4*(5), 328–332, doi:10.1038/ngeo1118, 2011.

[50] Schoof, C., Ice sheet grounding line dynamics: Steady states, stability, and hysteresis, *Journal of Geophysical Research: Earth Surface*, *112*, F03S28, doi:10.1029/2006JF000664, 2007.

[51] Shackleton, N., Oxygen isotope analyses and pleistocene temperatures reassessed, *Nature*, *215*, 15–17, doi:10.1038/215015a0, 1967.

[52] Tarasov, L., A. S. Dyke, R. M. Neal, and W. R. Peltier, A data-calibrated distribution of deglacial chronologies for the North American ice complex from glaciological modeling, *Earth and Planetary Science Letters*, *315-316*, 30–40, doi:10.1016/j.epsl.2011.09.010, 2012.

[53] Thomas, R. H., and C. R. Bentley, A model for Holocene retreat of the West Antarctic Ice Sheet, *Quaternary Research*, *10*(2), 150–170, doi:10.1016/0033-5894(78)90098-4, 1978.

[54] van der Wal, W., P. L. Whitehouse, and E. J. Schrama, Effect of GIA models with 3D composite mantle viscosity on GRACE mass balance estimates for Antarctica, *Earth and Planetary Science Letters*, *414*, 134–143, doi:10.1016/j.epsl.2015.01.001, 2015.

[55] Weertman, J., Stability of the junction of an ice sheet and an ice shelf, *Journal of Glaciology*, *13*, 3–11, doi:10.3189/s0022143000023327, 1974.

[56] Yokoyama, Y., et al., Rapid glaciation and a two-step sea level plunge into the Last Glacial Maximum, *Nature*, *559*, 603–607, doi:10.1038/s41586-018-0335-4, 2018.

[57] Yousefi, M., G. A. Milne, and K. Latychev, Glacial isostatic adjustment of the pacific coast of North America: The Influence of lateral earth structure, *Geophysical Journal International*, doi:10.1093/gji/ggab053, 2021.